AN ABSTRACT OF THE THESIS OF

Lee M. Edward for the degree of Master of Science in Mechanical Engineering presented on June 6, 2008.

Title: Characterization of Flow Boiling in a Fractal-Like Branching Microchannel Network

Abstract approved:

_____

James A. Liburdy

Based on experimental investigations the present study evaluates flow instability and void fraction in a fractal-like branching microchannel network with rectangular cross-section. The hydraulic diameter of the channels ranged from 308μm at the inlet to 143μm at the outlet. The flow network used is characterized by set branching ratios for channel length and width of $\frac{L_i}{\sqrt{2}}$ and $L_i \cdot \sqrt{2}$, respectively, and features 5 branching levels. Test were performed using DI degassed water heated to an 88°C inlet temperature with a mass flow rate of 10g/min. Heat fluxes of 1.76 W/cm^2 and 2.64 W/cm^2 were applied to the test device for the given flow rate. Finally, a control valve directly upstream of the test device was throttled until the pressure drop across the valve was roughly 100 times larger than the pressure drop across the test device. For the cases with and without throttling at the inlet, results for inlet pressure oscillation and vapor activity at the inlet and exit of the test device are compared. Frequency of inlet pressure oscillations and the upstream flow of vapor are correlated. In addition time averaged void fraction is presented for each branching level for the 10g/min, 1.76 W/cm^2 case with and without throttling and is compared to predictions from a 1-D model.

Characterization of Flow Boiling in a Fractal–Like Branching Microchannel Network

by

Lee M. Edward

A THESIS

Submitted to

Oregon State University

in partial fulfillment of

the requirement for the

degree of

Master of Science

Presented June 6, 2008

Commencement June 2009

Master of Science thesis of Lee M. Edward presented on June 6, 2008.

APPROVED:

_____

Major Professor, representing Mechanical Engineering

_____

Head of the School of Mechanical, Industrial & Manufacturing Engineering

_____

Dean of the Graduate School

I understand that my thesis will become part of the permanent collection of the Oregon State University Libraries. My signature below authorizes release of my thesis to any reader upon request.

_____

Lee M. Edward, Author

ACKNOWLEDGEMENTS

I would to thank my advisor, Dr. James Liburdy, for his many contributions to this thesis and his personal guidance in this area of research. I would also like to thank Dr. Deborah Pence and Dr. Vinod Narayanan for all of their vital input regarding this thesis and allowing me to participate in their research at Oregon State University. I am grateful to the Office of Naval Research (contract number Noo14-06-1-0017) for providing funding to facilitate this research. Also, much thanks to Mr. Douglas Heymann for his development of the image processing algorithm used for analysis of images in this thesis as well as his operation of the 1-D model code to generate the model results shown in this thesis and lastly his many answers to my many Matlab questions and quandaries. Thank you also to Mr. Daniel Krebs and Mr. Younghoon Kwak for their many additions to the experimental facility and calibration of instruments, especially to Mr. Younghoon Kwak for his addition to the voltage divider and flow data monitoring and recording program in Labview. I would like to thank my mother, Diana Edward, for teaching me the value and importance of following through and finishing strong in the tasks appointed to me. Lastly but most importantly I would like to thank Jesus Christ for the height and depth and width of His great and consuming love which has been lavished upon me. It is my prayer that somehow His love will be in the lines of this thesis and come upon any who may read it.

TABLE OF CONTENTS

TABLE OF CONENTS (Continued)

TABLE OF CONENTS (Continued)

TABLE OF CONENTS (Continued)

TABLE OF CONENTS (Continued)

LIST OF FIGURES

LIST OF FIGURES (Continued)

LIST OF FIGURES (Continued)

LIST OF FIGURES (Continued)

LIST OF TABLES

LIST OF TABLES (Continued)

Table Page

LIST OF TABLES (Continued)

Nomenclature

A_c	cross-sectional area of channels (m)
A_t	planform area of test device (m)
Bo	boiling number $\left(\frac{q''}{Gh_{fg}}\right)$
CHF	critical heat flux
CTF	continuous two-phase flow
D	diameter of channel (m)
DP_{max}	maximum instant pressure drop (Pa)
DP_{min}	minimum instant pressure drop (Pa)
DP_N	non-dimensional pressure drop oscillation magnitude $\left(\frac{\rho_{l,sat}\left[DP_{\max} - DP_{\min}\right]}{G^2}\right)$
F	frequency (Hz)
F'_I	liquid inertia force per unit length (N/m) $F_I' = \rho_l V^2 D = \frac{G^2 D}{\rho_l}$
F'_M	evaporation momentum force per unit length (N/m) $F_M' = \frac{q'' D}{h_{fg}} \frac{q''}{h_{fg}} \frac{1}{\rho_g} = \left(\frac{q''}{h_{fg}}\right)^2 \frac{D}{\rho_g}$
F'_S	surface tension force per unit length (N/m) $F_S' = \gamma \cos(\theta)$
G	mass flux (kg/(m^{2}s))
h	enthalpy of two-phase mixture (J/kg)
h_f	enthalpy of fluid (J/kg)
h_{fg}	enthalpy of vaporization (J/kg)
$h_{f,sat}$	saturation enthalpy of fluid (J/kg)
h_g	enthalpy of vapor (J/kg)
h_i	enthalpy of inlet fluid (J/kg)

K_1 ratio of F'_M and F'_I $K_1 = \left(\frac{q''}{Gh_{fg}} \right)^2 \frac{\rho_l}{\rho_g}$

K_2 ratio of F'_M and F'_S $K_1 = \left(\frac{q''}{h_{fg}} \right)^2 \frac{D}{\rho_g \sigma}$

L_h heated length of test device (m)

LALPO large amplitude large period oscillation

LTAF liquid two-phase alternating flow

LTVAF liquid two-phase vapor alternating flow

OFI onset of flow instability

ONB onset of nucleate boiling

OSV onset of significant void

Pe pressure energy per frequency (kPa^2/Hz)

p_h heated perimeter of test device (m)

Pi inlet pressure (kPa)

q" heat flux (W/m^2)

SASPO small amplitude small period oscillation

sat saturation condition

V fluid velocity (m/s)

x quality

Greek symbols

α void fraction

γ surface tension (N/m)

ρ_g density of vapor (kg/m^3)

ρ_l density of liquid (kg/m^3)

$\rho_{l,sat}$	density of saturated liquid (kg/m^3)
τ_C	vapor-liquid cycle time (s)
τ_{vr}	vapor residence time (s)
τ_{lr}	liquid residence time (s)
σ	standard deviation
θ	angle of contact of vapor interface with channel wall (degrees)

1 Introduction

1.1 Motivation for Microchannel Flow Networks

Microchannel networks are well suited to environments which demand high rates of cooling in compact spaces Mudawar [1], Kandlikar [2]. The scale of their hydraulic diameter affords them much higher rates of heat transfer compared to their macro-level counterparts Tuckerman & Pease [3]. When two-phase flow is introduced in the channels, the heat transfer coefficients of the channels typically increase by an order of magnitude above those realized by single phase forced convection. When two phase flow occurs, the pressure drop across channels of hydraulic diameter on the order of 10^{-6} m is substantially larger than that for conventional size channels though the flow rate required for these micro-devices is much lower than that for those of conventional size. Also, it is thought that a practical lower limit of d_h=200μm is necessary to avoid clogging of the channel due to limitations of conventional machining techniques Mudawar [1]. Once the heat flux input to the microchannel device becomes high (>100W/cm^2) it is thought channels of a minimum diameter of 510μm should be used due to the large pressure drop and potential for choking Mudawar [1].

In the present study flow boiling of water is investigated in a novel microchannel flow network whose geometry is inspired by naturally occurring systems in the world. The characteristics and distribution of vapor in the flow network is documented and analyzed for growth rates as well as correlated to the global pressure characteristics of the flow network. The behavior of unstable flows, here defined as the flow reversing direction and flowing upstream toward the inlet of the device, is investigated. Also, the

experimental results are compared with theoretical results generated from a 1-D model Daniels et al. [4].

1.2 Flow Observations & Phenomena

In general, in studies of flow boiling in microchannels investigators have observed distinct flow regimes which differed in some areas from those documented in macrochannels. Two large differences is the reduction or elimination of the effects of gravity on the flow in microchannels along with a greater dependence on the surface tension forces and the limitation of bubble growth by the channel walls Kandlikar [2]. While the heated flow in a microchannel test device is still single phase the temporal measurements of pressure and temperature are observed to fluctuate slightly; typically within the range of uncertainty of the measurement. As noted in Wu & Cheng [5], as the heat flux applied to the test device is increased and other parameters are held constant the fluid at the test section outlet will reach the saturation temperature and small bubbles will form. This is generally regarded as incipient boiling. Continuing to increase the heat flux will increase the growth rate of the bubbles and thereby reduce the time required for the bubble to nucleate and reach its departure size whereas increasing the mass flow of the liquid will inhibit or retard bubble growth. A higher flow rate means the energy introduced to the liquid is spread out over a larger volume of liquid and thus the growth rate of a single bubble will be reduced. Also, increasing the flow rate means increasing the shearing forces acting on the bubble and thus a reduction in the departure diameter is achieved Kandlikar [2]. Kennedy et al. [6] made similar observations of incipient boiling but used the term onset of nucleate boiling (ONB) to describe this occurrence. Xu et al. [7] observed ONB in their test device as well. However, rather than increasing heat flux

for a constant mass flux they decreased the mass flux at a constant heat flux. As they decreased the mass flux the flow transitioned from single phase liquid to the ONB. This transition point is defined as the point at which the measured demand curve deviates from the computed one which Xu et al. [7] notes as accounting for the variation in liquid viscosity with fluid temperature. As the heat flux continues to be increased for a given flow rate the amount of vapor present in the channels will also increase. This increase in vapor leads to the formation of different flow regimes. However, flow conditions which lead to different flow regimes can often be difficult to identify do to the visual abruptness and unpredictability of transitions between flow regimes in microchannel networks Qu & Mudawar [8].

Typically in air-water two phase flows many investigators documented a series of seven different flow regimes Kawaji & Chung [9], Serizawa et al. [10]. In these cases the air-water mixture is meant to simulate the behavior of liquid-vapor flows produced in heated devices with an increase in air flow corresponding to an increase in vapor generation resulting from an increase in energy input to the device. The flow regimes in the air-water devices progressed one into another as the relative flow rate of air to water was increased. The first regime is single phase liquid flow and occurs when no air is allowed in the test device. As the air flow rate is increased small bubbles of varying sizes but less than the diameter of the channels are observed. This is called bubbly flow. Increasing the air flow rate from this level generates bubbles which are of similar diameter to that of the channels. Thus they become constricted by the channel walls and are forced to extend up and down the length of the channel. In this case there are slugs of vapor in between slugs of liquid in the channel, thus it is named slug flow. Increasing the

air flow rate further causes the slugs to merge together into elongated slugs which are typically longer in length than the slugs of liquid that separate air slug from air slug. This is the elongated slug regime. Continuing to increase the air flow rate causes the elongated slugs to form a bridge between one another. This is done by pushing the liquid between the air slugs up against the channels wall thereby forming an air core in the middle of the channel between the air slugs. The liquid becomes a ring around the air core connecting the two air slugs and the regime is therefore called liquid ring flow. As the air flow rate is increased from this point the liquid flowing in the channel loses its symmetry and rather than flowing as rings it flows as intermittent lumps along the channel wall. Thus it is called liquid lump flow. Finally, as the air flow rate is increased further still the liquid is smoothed into a thin layer flowing along the channel wall and surrounds an air core in the middle of the channel. This is called annular flow. As the air flow rate is increased in this case the slip velocity of the air over the liquid increases and also the thickness of the liquid film may vary. There have been some exceptions to this progression, though they generally occur in transition regions between regimes. The existence of "frothy annular flow" was observed by Serizawa et al. [10], Saisorn & Wongwises [11]. In this case small bubbles are observed in the liquid layer along the channel wall between the air core of the channel and the wall of the channel. Generally these bubbles appear to protrude out into the air core in the middle of the channel but are not permitted to merge with it and can appear as an isolated bubble or a cluster of smaller bubbles bonded together. Serizawa et al. [10] also documented the occurrence of small liquid drops which clung to the channel surface within the boundaries of a gas slug when the channel was observed to be operating in the slug regime.

According to Kandlikar [2], stratified flow is absent for the most part in boiling flows in microchannels networks as it has only been observed at very low flow rates as those documented in Kasza et al. [12]. This is thought to be an effect of the dominance of surface tension forces in microchannel networks. Kandlikar [2] also noted the slug regime occurs over extensive periods of flow conditions making it the dominant flow regime to be expected in flow boiling short of annular flow. Typically once incipient boiling has begun in the test section a further increase in heat input causes an abrupt transition to slug flow leaving only a small window of flow conditions over which bubbly flow is sustained.

Chen & Garimella [13] studied boiling flow of water in a microchannel network consisting of 24 microchannels of cross-section 389x389μm and length 12.7mm machined in a silicon substrate. At low heat fluxes still large enough to produce nucleate boiling, they observed bubbles that grew on the channels walls to a certain size, detached and moved down stream. As the bubbles traveled together it was rarely observed that they coalesced and were mostly kept along the channel walls. Increasing the heat flux led to much stronger bubble interactions and merging thus transitioning the flow from the bubbly to the slug regime. Continuing to increase the heat flux led to unstable flows characterized by flow reversal and alternating flow regimes present in the test device. In fact it was stated by Chen & Garimella [13] that the alternating flow patterns were the direct result of the occurrence of flow reversal. They observed that once the flow reversed at the inlet a momentary reduction in flow rate occurred in the channels. Since the heat flux was held constant the vapor generation rate was increased in the channels during this transition period. This led to a transition from churn flow, which is

characterized by pockets of vapor distributed across the channel cross-section, to annular flow, characterized by a vapor core in the middle of the channel surrounded by a liquid film on the channels wall. It was found that the frequency of flow reversal was the same as that of the transition from churn to annular flow in the channels. Furthermore, the conditions which led to flow reversal brought about pressure drop oscillations across the device of about 1 kPa whereas flow conditions that did not produce flow reversal yielded a value of about 0.5 kPa. When the flow was transitioning between churn and annular there was a definite front separating the regions of churn and annular flow which would move downstream as the next flow regime was initiated.

Kasza et al. [12] studied flow boiling in a 500mm long rectangular channel with a cross-section of 2.5X6.0mm. Here a similar pattern of transition from nucleate bubbles, to wall confined bubbles to slugs to annular flow with increasing heat flux or decreasing mass flux was observed. They found that as large vapor slugs swept through the channel they coalesced with smaller nucleating bubbles and increased the large slug's vaporization rate as a result. Kasza et al. [12] found that if the wall temperature was high enough the slugs would grow to the point at which they would occupy the length of the channel and annular flow would be realized. They observed an interesting phenomenon in the annular flow region. In the annular flow region nucleation sites would still be active in the thin liquid film between the vapor core and the channel wall. Similar observations were made for air-water two phase flows by both Serizawa et al. [10] and Saisorn & Wongwises [11]. Both of these investigations revealed “frothy” liquid-ring and liquid lump flow. In these cases small bubbles were observed in the liquid film near the channel wall while the center of the channel was occupied by a gas core. Kasza et al.

[12] observed these sites would produce bubbles which would grow and push the liquid film out into the core of the annular region without allowing merger between the nucleate bubble and the annular core. Eventually the bubble "discharged" its vapor into the core of the annular region. This process occurred over a few thousandths of a second. Usually this would cause the nucleating bubble to deform and squish into a shape more closely resembling an oval whereas when no vapor core was present over the top of the nucleating bubble the bubble would grow spherically until it detached. In the case where the nucleating bubble was growing under a vapor core the bubble demonstrated much more "reluctance" to merge with the vapor core than it did to merge with another bubble. Typically the bubble nucleating under a vapor core would grow for a much longer period of time than a bubble growing with no vapor core present. For the case when it was present the frequency of bubble nucleation was 63 bubbles/second and with no vapor core present the frequency was 42 bubbles/second. So with the vapor core bubbles nucleated more frequently and grew for a longer period of time.

Li et al. [14] noticed similar trends in bubble formation and growth as has been found in conventional size channels as well as single microchannels; the streamwise location of the onset of nucleate boiling (ONB) moves upstream toward the inlet for an increase in heat flux. Also, consistent with these types of channels, it was found that at high enough mass fluxes the addition of greater heat input to the device caused higher rates of bubble growth. Li et al. [14] studied convective flow boiling of water in two parallel microchannels with trapezoidal cross-sections. The channels were 41μm deep, 41μm wide at the base, 100μm wide at the top and 28mm long. The channels were micro-machined into a 5mm wide strip of Si. The deionized water they used for the

experiment was degassed by boiling in a beaker but then allowed to cool to room temperature and from the beaker poured into the syringes they used to pump the water to the test device. This procedure effectively re-aerated the water as they themselves note in their article.

However, they notice something very strange that occurred during the two low flow rate cases of 105 and 269 kg/(m^2s) . In these two cases an increase in heat flux input to the device actually lowered the bubble growth rate! They believed this occurrence was due to the increase in heat flux triggering an increase in the local pressure and saturation temperature of the fluid surrounding the vapor. They stated the increase of these properties may suppress the bubble growth mechanisms. It should also be taken into consideration that the flow was unstable for both low flow rate conditions which is described in the instability section as having a significant effect on bubble growth. The reduction in bubble growth rates may only be indirectly linked to low flow rates in that the low flow rate produces an environment in which flow instability occurs and it is the instability itself which causes local pressure oscillations which then impedes the bubbles ability to grow.

For the 269 kg/(m^2s) case it was found for both 143 and 303 kW/m^2 the bubble radius increased linearly with time which Li et al. [14] reported as an indication the growth was inertia dominated. However, the case with 190 kW/cm^2 for the same flow rate demonstrated bubble radius growing with the square root of time and was interpreted as indicating a diffusion dominated growth. For stable flow configurations an exponential slug growth rate was found; this is different than what was found for the growth rate of bubbles. The growth rate of the slug was measured by an increase in

overall length. The slug fills the cross-section of the channel so the length seems an appropriate gage of growth. As Li et al.[17] noted this exponential growth indicates the slug is growing in an environment dominated by the evaporation effect over the local pressure effect. Definitely the pressure around the slug has an effect on the shape or curvature of the vapor interface. Li et al. [14] found the interface of a vapor slug which was subjected to a higher pressure displayed a much flatter interface or an interface with a larger radius of curvature than the interface of the slug subjected to the lower region of pressure. The slug appeared to take on the shape of a bullet with the "nose" of the slug pointing in the direction of the flow.

1.3 Flow Instability in Microchannel Networks

It has been shown two-phase flow in microchannel networks is sensitive to hydrodynamic instabilities which limit or reduce the devices ability to effectively remove heat and/or increase the cost associated with operating the device Qu & Mudawar [15]. Also, these instabilities can lower the heat flux at which CHF is reached for a given microchannel network, by inducing it before dryout conditions are actually reached Hetsroni et al. [16]. Typically these instabilities were found to occur at low flow rates or high input heat fluxes Wu & Cheng [5]. Instabilities can be classified as static or dynamic. The two types of instabilities of greatest concern fall in the dynamic category and are labeled pressure drop oscillation and parallel channel instability. A system undergoing pressure drop oscillation sees the liquid-vapor interface move upstream simultaneously in all channels of the array from the channel exit toward the inlet. In some cases the vapor reaches the inlet plenum of the channels in the network. The vapor will continue its progress upstream until the pressure at the inlet becomes large enough to

flush the vapor through the channels and replaces the vapor with fresh liquid Jiang et al. [17]. Then nucleation occurs and the vapor bubbles grow and begin propagating upstream and the cycle starts over again. It is believed that pressure drop oscillation can be triggered by the phenomena known as flow excursion or Ledinegg instability Qu & Mudawar [15]. This is an example of a dynamic instability triggered by a static instability. In this circumstance if the slope of the demand curve of the heated test section is less than the demand curve of the pump in the flow loop then the system is operating in an unstable mode; see fig.A1 in appendix A. In this case for a given pressure differential across the pump the velocity of the flow in the test section can be abruptly reduced by a substantial amount. If this happens and the heat input to the test device remains constant the boiling in the test section will become much more vigorous and the ability of the flow to retard the vapor growth upstream will be diminished. It was also noted that Ledinegg instability could induce parallel channel instability as well by Kosar et al. [18]. This makes sense due to the fact the phenomenon of parallel channel instability is similar to pressure drop oscillation instability but is characterized by a pressure drop oscillation occurring in each channel. However, the channels will be out of phase with one another whereas in pressure drop oscillation the movement of vapor fronts in the channels have been observed to behave in phase. In pressure drop oscillation the vapor fronts in each channel move in unison up or down stream. In parallel channel instability the vapor fronts in each channel oscillate up or down stream independently; somewhat reminiscent of cylinders pumping in an engine. Parallel channel instability is like pressure drop oscillation localized to a single channel. However, it is more complicated than that. Due to the thinness of the channel walls in

microchannel networks, neighboring channels are able to interact with each other through conduction Chang & Pan [19], Li et al. [14], Lee & Pan [20]. This is expressed through instability in one channel destabilizing or triggering instability in a neighboring channel(s). This effect becomes more pronounced when the flow rate is low due to the fluid having a longer residence time in the channels and thus greater amounts of time to interact with fluid in surrounding channels. Parallel channel instability is noted as a milder instability than pressure drop oscillation by Qu & Mudawar [15]. In their experiment the magnitude of the oscillation of inlet pressure was shown to decreases by roughly a factor of 2.5 and the frequency of the oscillation was shown to increase by nearly an order of magnitude when the flow transitioned from pressure drop oscillation to parallel channel instability.

Li et al. [14] documented bubble growth in two parallel microchannels in which they presented a bubble growing in only one of the channels and suggested the reason for the presence of single phase flow only in the neighboring channel to this feedback effect due to the thinness of the channel walls. All the energy at this location was being used to evaporate the liquid film in the one channel and thus being directed away from the neighboring channel. To compound this effect, once the slug occupied the given channel the pressure drop across that channel increased bringing about a decrease in flow rate thereby increasing the flow rate in the other channel. So the channel which sees the bubble first will consume more energy. Also, this could explain why the growth of vapor slugs under stable conditions was found to be exponential by Li et al. [14]; in that once the channel nucleates a bubble it consumes more energy as the bubble grows larger thus increasing the growth rate of the bubble over time. However, if for some reason the

bubble growth was stopped or possibly reversed it would seem then the effective heat flux to the other channel would become greater and cause nucleation and/or bubble expansion in the neighboring channel.

Jiang et al. [17] also observed the upstream propagation of vapor to the inlet plenum of their test device. They used a parallel microchannel array consisting of 34 or 35 microchannels with a heater located directly under the inlet of the test device. They noted three distinct flow regimes that varied with the ratio of heat flux input to the critical heat flux for the device at a given flow rate and inlet fluid temperature. The first was single phase liquid flow at the device inlet and outlet for a heat flux ratio defined as input heat flux to critical heat flux < 0.4. Next was what they described as nucleation flow boiling between a heat flux ratio of 0.4 and 0.6. Above this they reported annular flow for the heat flux ratio > 0.6. For the second region of heat flux ratio, nucleation boiling, they discovered and documented large bubbles which would be generated at and fill the inlet as well as the outlet of the test device. They reported the bubbles at the inlet would continue to grow and fill the inlet until the upstream pressure became great enough the flush them through the channel network. The bubbles at the inlet were typically of diameters several times larger than the characteristic width of the channels so when the bubbles were forced through they reportedly traveled at rates of speed to great too be observed until they emerged again at the outlet. The inlet and outlet of the channels acted as condensers and diffusers accelerating and slowing the flow, respectively. They did not report the inlet pressure or outlet pressure of the test device during this bubble growth and clearing at the inlet but they must have seen fluctuations similar to what is seen in the pressure drop oscillation instability mode. The flow rates of their test case varied from 2-

55 g/min and the test fluid entered the test device at room temperature. It is questionable if the bubbles they saw generated at the inlet were actually vapor or just the water degassing due to the increase in temperature. They reported to have used deionized water but did not state if it had been degassed and given the low inlet temperature of the water there is the potential for much gas to come out of the water once it reached the heated test section. The bubbles they describe were actually generated at the inlet rather than flowing upstream into the inlet. However, it was found once the bubble in the inlet of the channel network becomes larger than the characteristic channel dimension there is required a significant increase in inlet pressure to force the bubble through the channel network. This could explain the reason why, in the absence of upstream flow of vapor, they observed oscillations in pressure.

When the flow becomes unstable it has been observed that dry-out conditions in the microchannel network occur at lower heat flux for a given flow rate than in a network experiencing stable flow patterns. Under stable boiling conditions, the flow regimes occurring in the microchannel will progress through the stages described earlier. Once the annular flow regime is reached the liquid film will eventually be completely evaporated away until the channel is occupied completely by vapor. This is known as critical heat flux (CHF) Mudawar [1]. However, once the flow becomes unstable and vapor propagates upstream many of the intermediate flow regimes that occur prior to CHF are bypassed and CHF is reached at lower heat flux conditions for a given flow rate as a result, Mudawar [1]. When CHF occurs the device can fail causing it to be “burned up” or destroyed and also can damage or destroy the device being cooled. So it is seen to

be beneficial and necessary to investigate ways of eliminating or reducing the initiation and severity of flow instabilities in microchannel networks.

1.4 Suppression of Flow Instabilities

Recently many investigators have sought modifications to the test devices which would alleviate the flow boiling instabilities or at least lessen their effect. Qu & Mudawar [15] investigated two-phase flow phenomena in 21 microchannels 231μm wide 712μm deep machined in a copper test section 4.48 cm in length. They found that introduction of an upstream control valve could suppress pressure drop oscillation in their test device when throttled. The control valve was directly upstream of the test section and was throttled until the outlet pressure of the flow loop gear pump increased from 1.5 bar to 2.0 bar. The pressure drop across the test device was unaffected in this process. The pressure drop across the system, including filter, flow meter, constant temperature bath, control valve, and test device, increased from 33 to 83 kPa as a result of throttling, meaning a 50 kPa pressure drop across the throttle. From the data they presented the pressure drop across the test device with the upstream control valve throttled was about 160 kPa. So once the upstream control valve was throttled such that a pressure gradient roughly 30% of the pressure drop across the test device was established upstream the pressure drop oscillation instability was suppressed in the test device even for an increase of heat flux by roughly three times. However, the test device still displayed signs of hydrodynamic instability while operating with the throttle valve in place though they were less pronounced than the pressure drop oscillation instability. The magnitude of the pressure oscillation was decreased by about a factor of three and the frequency of oscillations increase between seven and ten times. Also, the amplitude of the oscillations

of the outlet pressure of the test device were reduced by an order of magnitude and the mean value of the outlet pressure was lowered substantially below that of the inlet. In the case without throttling the inlet and outlet pressure oscillated in phase. The type of instability observed with the throttle valve in place was classified as the milder type of instability known as parallel channel instability. In effect the upstream control valve isolates the test device from the upstream compressible volume which can be an air bubble upstream in the flow loop or the result of flexible tubing upstream of the test device. However, in the case of microchannels it can stem even from "a large volume of degassed liquid" upstream of the microchannels at the inlet of the device Kosar et al. [18]. As noted in Qu & Mudawar [15] the throttle valve effectively increases the system stiffness making it less susceptible to the effects of compressibility.

Kosar et al. [18] investigated two-phase flow phenomena in 5 microchannels 200μm wide and 264μm deep etched into a Si test device 1.00cm in length. They stated that a single upstream control valve was sufficient to isolate the test device from the upstream compressible volume and thus suppress the pressure drop oscillation mode of instability. However, in order to suppress the parallel channel instability they reasoned each channel would need to be throttled individually in order to isolate it from the fluid in the inlet plenum. To do this they made four separate test devices three of which were made with orifices at the inlet of each channel. The orifices were 20μm wide and ranged and each device had a differing orifice length. The lengths were 50, 100 and 400μm and one test device was fabricated without any orifice at all as a base to test the devices with orifices against. For the device without any orifices conditions associated with pressure drop oscillation and parallel channel instability were observed. These include the

oscillations in measured pressure and temperature. However, due to the reduced number of microchannels and a test section length of four times less than the test device used by Qu & Mudawar [15] the magnitude and frequency of the pressure drop oscillation is different. The frequency looks to be roughly the same and definitely the same order of magnitude but the magnitude of the oscillation is reduced by two orders of magnitude. They noted as the length of inlet orifice increased the heat flux which, for a given flow rate and inlet temperature, caused unstable boiling to occur also increased. In fact the heat flux at which unstable boiling occurred in the devices with the two greatest lengths of orifices was almost identical. The authors believed this was an indication that for these orifice lengths hydrodynamic instabilities had been "eradicated" and the heat flux corresponding to unstable boiling actually indicated that a critical heat flux condition had been reached in the device.

Muwanga et al. [21] investigated two-phase flow of water in a parallel channel network consisting of 45 microchannels 269μm wide and 283μm deep etched in a Si test piece 16mm in length. The addition they made was etching three channels 269μm wide across the microchannel network at equal intervals. Their idea was to connect all the microchannels together with these "cross-links" at several points along the stream wise direction to deter vapor from flowing upstream into the common inlet of the device. In addition they performed tests on a device of the same dimensions and material without the cross-links in order to compare the performance of the two devices. It was found the onset of flow instability occurred at the same heat flux for the same flow rate and inlet temperature for both the device with cross-link geometry and that without. However, the addition of the cross-links decreased the magnitude of the inlet pressure oscillations by

about 22% and decreased the frequency of the oscillations by about 57%. While holding the flow rate and inlet temperature constant it was found that for each input heat flux the frequency and the magnitude of the oscillations were reduced. For both devices the oscillations of measured temperature and pressure of the devices were in phase. The magnitude of the oscillations seems to be a measure of the severity of the instability as was found by Qu & Mudawar [15]. So a reduction in magnitude of oscillation of the pressure drop indicates a reduction in the strength of the oscillations and a reduction in the frequency of the oscillations indicates a decrease in the number of vapor fronts flowing upstream to the inlet of the device over time. In the case of the modifications made to the test device by Muwanga et al. [21] there is a reduction in the severity of the instabilities but they are not eliminated.

Chang & Pan [19] investigated boiling instability and its effect on bubble formation and growth in fifteen parallel microchannels 99.4μm wide, 76.3μm deep and 20 mm long machined in a Si test section. They noted that flow boiling instabilities typically are found in microchannel networks operating at low mass fluxes or high heat fluxes. Also, for a given mass flux increasing the heat flux increases the magnitude of the oscillations of pressure and temperature of the fluid and likewise for a given heat flux decreasing the mass flux increases the magnitude of the oscillations. This is consistent with observations of the other investigators in this area. They also reported the feedback effects in microchannels are much more complicated than those of larger scale channels due to the thinness of the wall dividing the channels. This effectively makes transferring thermal energy between channels very easy or reduces the time required for the fluid in

one channel at a given state to be effected by the fluid in the neighboring channels as compared with larger scale channels.

Their test conditions ranged from flow rates of 22-44 kg/(m^2* s) with heat fluxes of 0.791 W/cm^2 - 8.77 W/cm^2 and an ambient inlet fluid temperature. They also recorded bubble formation and behavior using a CCD camera set to acquire images at 250 frames/second. They found that for stable two-phase flow conditions after a bubble becomes a vapor slug it will grow at a roughly exponential rate, which is thought to be mainly limited by the pressure field around the bubble and the channel wall temperature. For a flow rate of 22 kg/(m^2*s) at 0.791 W/cm^2 they found a growth rate of the form $e^{\beta t}$, where β=5.87, found using a curve fit to their experimental data. This agrees with the type of slug growth seen in stable flow configurations by Li et al. [14], who reported vapor slug growth is a balance between the evaporation of the liquid film between the vapor and the channel wall and the pressure field in the liquid surrounding the vapor. Holding the above flow rate constant and increasing the heat flux to 1.58 W/cm^2, roughly double that of the initial value, the boiling in the test device became unstable characterized with the large fluctuations in pressure and temperature seen in other documented work. With the given factors influencing slug growth it's not surprising the rate of slug growth becomes unstable characterized by shrinking and then expanding repeatedly when the flow conditions become unstable and produces severe oscillations in pressure drop. This phenomenon was also observed by Li et al. [14] which also noted both the front and rear cap of the vapor slug oscillated expanded “rapidly”. Chang & Pan [19] provided a plot of slug length vs. time for 44 kg/(m^2*s) and 8.77 W/cm^2, which is in the unstable flow regime. The length appears to oscillate with respect to time which

corroborates with the visual data recorded. However, the frequency of the bubble growth oscillation appears to be three orders of magnitude greater than the oscillation frequency of the pressure drop generally observed for pressure drop oscillation instability. This could be the "rapidness" of expansion noted by Li et al. [14]. The bubble growth oscillation is on the order of 100 Hz whereas the pressure drop oscillation frequency is on the order of 0.1Hz. The range of time over which they provided data was very small, about 0.025 seconds, so drawing any conclusions from this would be rash. However, it could be that the local pressure fluctuations surrounding the vapor slug are three orders of magnitude higher than that measured across the entire device from inlet to outlet. Also, Li et al. [14] noted a bubble volume increase may also trigger an increase in the local pressure surrounding the bubble which would in turn limit the growth of the bubble. But vapor slug growth is governed by more than the local pressure field. Other investigators have noted that CHF condition is affected by the oscillations of flow conditions during instability; meaning the channel wall temperature could be oscillating as well.

Hetsroni et al. [16] studied convective flow boiling of water in three microchannel networks of 13, 21, 26 channels with hydraulic diameters of 220, 130, and 100μm, respectively. The channels were etched in Si and were 15 mm in length with cross-sections of isosceles triangles. They documented the phenomena of explosive boiling oscillations (EBO's) and the main parameters which affect the EBO's. EBO's are formed when a bubble after nucleation grows and reaches the slug regime. Once this happens the sudden increase in channel wall temperature causes the liquid film between the channel wall and vapor core to evaporate rapidly and thus causes the caps on both ends of the slug to expand up and downstream simultaneously. It is observed that this process is periodic.

Their studies showed the time interval between successive EBO's, τ, was dependent on heat flux and mass flux and therefore chose the boiling number, $Bo=q/(m*h_{LG})$, and the dimensionless time period τ^*, $\tau^*=\tau/(U*d_h)$, to characterize the time of the oscillations. It should also be noted their definition for τ^* cannot be correct if it is to be non-dimensional. Currently their definition yields units of s^2/m^2. A relationship of the form

$$\tau^* \sim C_2 Bo^{m_2} \tag{1.1}$$

was determined empirically where the constants C_2 and m_2 are determined by experimental results and were determined to be 0.00003 and -2 respectively. They concluded from their results that an increase in boiling number causes the non-dimensional time period between EBOs to decrease. However, this seems strange due to the fact they found by increasing the heat flux while holding the mass flux and other flow conditions constant the frequency of the pressure drop oscillations decreased and the amplitude increased slightly. If the oscillation frequency decreases one would expect the number of cycles of EBOs over time to be reduced and therefore the time between EBOs to be reduced as well. With this in mind it seems odd their data also shows a decrease in τ^* for an increase in Bo, or an effective increase in heat flux. However, Muwanga et al. [21] found a similar decrease in frequency and increase in amplitude as Hetsroni et al. [16] for oscillations of pressure drop with an increase in heat input. Li et al. [14] noted that at low flow rates undergoing flow instability additional input of heat flux for a given flow rate produced lower bubble growth rates. It should be noted this observation was made in regard to growth of a bubble from a nucleation site along a channel wall in the period from nucleation until the bubble detached or connected with the opposing channel wall.

Nevertheless, if lower frequency oscillations indicate less vapor being produced perhaps there is agreement between these cases.

Wu & Cheng [5] sought to document boiling instability in eight parallel microchannels of trapezoidal cross-section with a top width, bottom width, and depth of 427, 208 and 146μm respectively. The channels had a hydraulic diameter of 186μm and were 30 mm in length. Deionized degassed water was pumped into the test device at room temperature via nitrogen gas pressurizing the holding tank in a similar fashion as Chang & Pan [19]. They documented their flow instabilities not as the point at which flow reversed and vapor entered the inlet plenum but rather as a cyclical transition between flow regimes. At q=13.5 W/cm^2, $\dot{m}$ =14.6 g/(cm^2 *s) and q=16.6 W/cm^2, 12.7 g/(cm^{2}s) they observed single phase liquid two-phase alternating flow (LTAF). Further increasing the heat flux and decreasing the mass flux to 18.8 W/cm^2 and 11.9 g/(cm^2*s), respectively, they observed continuous two phase flow (CTF). Yet another increase in heat flux and decrease in mass flux to 22.6 W/cm^2 and 11.2 g/(cm^2*s), respectively, yielded liquid two-phase vapor alternating flow (LTVAF). Here the term vapor flow indicates annular flow. Whether or not vapor actually entered the inlet or if flow reversal occurred in this experiment was not discussed in the paper. However, they did report similar fluctuations in inlet pressure and temperature of the device as was seen in test devices experiencing flow reversal. For all of the "unstable" flow configuration cases the oscillations of temperature and pressure are in phase with one another but out of phase with the mass flux oscillations. In fact the mass flux oscillations in all unstable flow configurations don't appear to have any dominant frequency or periodic behavior but look more like a random scatter plot of fluctuations. If there is any periodic nature to the mass

flux data its dominant frequency is likely to be two orders of magnitude greater than those seen in the data for pressure and temperature. For the first LTAF case and the CTF case the oscillation magnitude and frequency are on the order of 1 kPa and 0.01 Hz, respectively. This magnitude is similar to that seen by other investigators Muwanga et al. [21], Chang & Pan [19] but the frequency is much lower, two orders of magnitude, than other investigators observed for flow reversal and pressure drop oscillation. For the second LTAF case the magnitude of the oscillations was similar but the frequency decreased an order of magnitude to 0.001 Hz. From the data shown it takes nearly 200 seconds to complete one cycle. For the LTVAF case the frequency of the oscillations returned to a similar value as that of the first LTAF case and the CTF case but the amplitude of the oscillations increased by an order of magnitude to 10 kPa. They believed the alternating flow regimes were caused by the generation of vapor suddenly causing the pressure drop across the test section to decrease which in turn yielded a decrease in flow rate. This decrease in flow rate in turn caused a decrease in pressure drop and thus the pressure and flow conditions oscillated. When the mass flux increased the constant heat flux wasn't sufficient to boil the incoming flow and so single phase liquid flow could be observed whereas when the flow rate was decreasing the heat flux was more than enough to boil the incoming flow and so one of the two phase flow patterns could be observed.

1.5 Flow Instability and Growth Rate and Behavior of Vapor

Li et al. [14] found that when flow reversal occurred in either the one or two channel parallel microchannel networks they investigated the growth rate of nucleating bubbles actually decreased with increasing heat flux. In the two channel network the

lowest flow rates used in the experiment the flow was always unstable. However, with the largest flow rate used the flow was always stable. When no flow reversal occurred the bubble growth rate was seen to increase with increasing heat flux as would be expected.

The authors do mention that flow reversal (instability) causes a decrease in bubble growth rate. However, the explanation of the likely cause of decreasing bubble growth rate with increasing heat flux is that following an increase in heat flux the local pressure was seen to significantly increase and thus the saturation temperature would also increase significantly. If the local saturation temperature around a bubble was increased it could substantially limit the growth rate of the bubble. At a given input energy rate if the local saturation temperature was increased a growing bubble would grow at a much smaller rate as more of the input energy would be used to warm the liquid surrounding the bubble.

It is likely the reason the local pressure was seen to significantly increase with an increase in heat flux is due to the upstream flow of vapor triggered by an unstable set of flow conditions. When the flow reversed and vapor propagated upstream the local pressure was seen to increase significantly thereby reducing the rate of bubble growth. The effect of the change in local pressure surrounding a vapor slug or bubble should have a two-fold effect. On the one hand a decrease in pressure at a vapor front would decrease the flow resistance to the motion of the vapor front. On the other hand the saturation temperature would also decrease and thus more vapor would be generated from a given heat input. So in the case of a decrease in local pressure a vapor front would move faster due to an increase in the rate of evaporation and a decrease in flow resistance; of course

the opposite would happen for an increase in local pressure. As the pressure oscillates it would then be expected for the length of the vapor slugs and bubbles to oscillate as well.

Chang & Pan [19] also observed odd behavior of vapor with unstable flows. For stable flow conditions they found vapor slugs grow exponentially with respect to time though they note not very smoothly due possibly due to slight fluctuations in the pressure field surrounding the slug. However, when the flow became unstable the authors observed the usual oscillations in pressure drop across their test device. However, they also observed the length of the vapor slugs oscillated under these conditions; in this case oscillating means growing and shrinking alternatively. However, the oscillations of slug length found by Chang & Pan [19] did not drop below a ratio of one, meaning that the length of the slug under consideration never shrank to less than its initial value. This is not the case in the present experiment where vapor slugs have been seen to collapse down to an order of magnitude less than the initial length.

From a plot of slug length versus time produced by Chang & Pan [19] it appears the slug length is oscillating at as much as three orders of magnitude higher than the pressure drop across the test device. Of course this is hard to tell from a visual estimation but it is clear that when the flow becomes unstable and pressure oscillations are induced across the test device the local pressure surrounding vapor slugs or bubbles oscillates and thus causes the local saturation temperature to oscillate as well and it can be determined from this plot then local oscillations of bubble length are higher frequency than the global oscillations of pressure drop.

1.6 Prediction of Stable/Unstable Flow Boiling Threshold

Several investigators have attempted to provide criteria which when satisfied will lead to flow instability. Chang & Pan [19] did find a condition that when satisfied would instigate boiling instability. They found that if the difference between the maximum pressure drop across the test device and the minimum pressure drop was greater than 6 kPa the flow would become unstable. This means that at a pressure drop difference of more than 6 kPa vapor would flow upstream and vapor slug growth would oscillate as previously discussed and two-phase mixtures would flow upstream into the inlet. But it is important to note that fluctuations in flow conditions exist at all points whether stable or not but the magnitude and frequency of the oscillations determine when the flow becomes unstable. It should be noted that due to the experimental set-up used by Chang & Pan [19] the mass flow rate was not independent of the oscillations as is pointed out by Hetsroni et al. [16].

Xu et al. [7] found that the onset of flow instability (OFI) occurred at the minimum point on the demand curve for the test section. Studied in this paper were 26 microchannels of width and depth of 300μm and 800μm, respectively, and 50mm in length. They found a progression in flow phenomena as they decreased mass flux while holding other experimental conditions constant. Single phase flow occurred until the mass flux was lowered enough until fine bubbles appeared on the channels. This was denoted as ONB similar to the previous papers mentioned. A further decrease in mass flux let the bubbles grow larger and detach. Upon detachment their diameter was the same as the channel width. This point was labeled the onset of significant void (OSV). The OSV occurs also at a lower pressure drop on the demand curve. However, the

authors noted the difficulty in distinguishing between ONB and OSV over identifying them for macrochannels. Qu & Mudawar [8] have used the phrase "boiling incipience" to replace ONB and OSV because of this difficulty. Finally, a minimum point on the demand curve is reached with a slight reduction in mass flux below that which yielded OSV. This is the point labeled OFI and any further reduction in mass flux from this point will result in an increased pressure drop across the system due to the presence of large amounts of vapor in the test device as well as unstable flow. By means of empirical correlations Xu et al. [7] found expressions for the mass flux and heat flux leading to the onset of flow instability. For a given heat flux the flow become comes unstable when the mass flux is less than or equal to

$$G_{OFI} \leq 1.17 G_{sat} \tag{1.2}$$

where

$$G_{sat} = \frac{q'' A_t}{A_c \left(h_{f,sat} - h_i \right)} \tag{1.3}$$

which was found via a simple energy balance. For a given mass flux Xu et al [7] found the flow becomes unstable for a heat flux greater than or equal to

$$q''_{OFI} \geq 3 + 0.834 q''_{sat} \tag{1.4}$$

where

$$q''_{sat} = \frac{G A_c \left(h_{f,sat} - h_i \right)}{A_t} \tag{1.5}$$

which is also found via a simple energy balance. In each expression "sat" refers to saturation conditions at the exit of the device. The saturation conditions were calculated based upon a simple energy balance.

Xu et al. [7] also observed flow reversal in their test device. For a low inlet temperature of 30°C with a mass flux varying from 0-446 kg/(m^2s) and an applied heat flux of 56.3 W/cm^2 they found large amplitude long period oscillations (LALPO) superimposed upon short amplitude short period oscillations (SASPO). The LALPO had a magnitude of about 18 kPa and the SASPO were down around 5-8 kPa. A Power Spectral Density (PSD) analysis was done on the signals and it was discovered the dominant frequency of the LALPO and the SASPO were $7.87*10^{-3}$ Hz and 0.197 Hz, respectively. When the inlet temperature was increased to 50°C and the heat flux decreased to 43.3 W/cm^2 the mass flux fluctuated from 0-543 kg/(m^2*s), the LALPO type oscillations disappeared and only the SASPO type oscillation of pressure and temperature remained. For this case the SASPO showed a magnitude of inlet pressure oscillation of 6-8 kPa and a frequency of about 0.1 Hz and appeared to be in phase with the recorded values of inlet and outlet temperature. They noted that when the peak in the time signals for pressure and temperature occurred for each cycle there was a corresponding presence of vapor in the inlet of the test device. Interestingly it appears the vapor only required about 20% of the cycle time to work its way from the outlet as fine bubbles all the way upstream to the inlet and the other 80% of the cycle time was needed to flush the vapor out of the channels and begin the cycle over again.

Xu et al. [7] reported that these SASPO type oscillations had a cycle length of about 10 seconds and went through 4 characteristic processes during each cycle. The first step was ONB near the channel exit. These bubbles would grow and fill the channels (OSV) and this was near the stage of OFI. Second, the vapor liquid interface would propagate upstream toward the inlet and this corresponded to the time at which the

pressure drop across the test section was increasing and the mass flux was decreasing. At this time the region of the channel occupied by vapor would see a decrease in heat transfer coefficient and thus an increase in channel wall temperature. Third, the interface would eventually reach the inlet and upon contacting the "cool" liquid at the inlet the vapor would undergo a strong condensation process and cause the vapor slug to shrink. Fourth, the vapor interface would recede downstream until it was completely flushed away and fresh liquid would fill the channels. During this time the pressure drop across the test device would drop the mass flux would increase and the channel wall temperature would decrease

Kennedy et al. [6] also found that OFI occurred when the device was operated at the minimum point on the device's demand curve. In this paper results for single 1.17 mm and 1.45 mm diameter copper tubes 22 cm in length with heated lengths of 16 cm were investigated. They defined a similar set of empirical relations to define OFI as does Xu et al. [7]. For a given heat flux Kennedy et al [6] found the flow became unstable for mass fluxes at or below

$$G_{OFI} \le 1.11 G_{sat} \tag{1.6}$$

where

$$G_{sat} = \frac{q'' p_h L_h}{A_c \left(h_{f,sat} - h_i \right)} \tag{1.7}$$

Again "sat" refers to saturation conditions of the fluid at the exit of the device and the saturation mass flux was determined via a simple energy balance. For a given mass flux Kennedy et al. [6] found the flow becomes unstable when the heat flux is at or above

$$q''_{OFI} \ge 0.9 q''_{sat} \tag{1.8}$$

where

$$q''_{sat} = \frac{GA_c\left(h_{f,sat} - h_i\right)}{p_h L_h} \tag{1.9}$$

The saturation heat flux is found through an energy balance. There seems to be good agreement for the value of G_{OFI} between Kennedy et al. [6] and Xu et al. [7] but the value q''_{OFI} is somewhat different. In each expression there is a coefficient less than one which multiplies the saturation heat flux. However, Xu et al. [7] found that there is a constant added to the modified saturation heat flux whereas Kennedy et al. [6] used no constant added at all. However, the magnitude of the heat fluxes renders the constant found in the expression derived by Xu et al. [7] to be negligible. In fact the expression derived for the unstable heat flux by Kennedy et al. [6] yields slightly larger values than does the one derived by Xu et al. [7]. It does seem strange to have the heat flux corresponding to OFI as less than that of the heat flux corresponding to the saturation of the exit fluid. In fact if this is the case then any flow boiling at all would fall into the unstable regime at least according to the given definitions. This seems due to uncertainties in the measurements in both Xu et al. [7] and Kennedy et al. [6] and the fact it was reported by Qu & Mudawar [8] to clearly identify or delineate between ONB and OSV was difficult to impossible. OFI occurs slightly after OSV as is found by Xu et al. [7] making it difficult to identify the conditions at which OFI occurs when it is defined in terms of the ONB heat flux or mass flux. Logically it must occur after ONB which corresponds with saturation conditions at the exit of the device.

Another possible way of predicting the onset of instability is documented in Kandlikar [22]. Here Kandlikar sought to describe the forces acting on the vapor-liquid

interface. He described the behavior of an interface as governed by three principal forces; the evaporation momentum (F'_M), the inertial force of the fluid (F'_I), and the surface tension acting on the interface (F'_S); the definitions of these parameters can be found in the nomenclature and appendix A. Also Kandlikar [22] created two new non-dimensional parameters K1 and K2 which related the forces which impede the upstream propagation of the vapor front (F'_S and F'_I) to the force which is trying to expand the slug both up and downstream (F'_M). K1 represents the ratio of F'_M to F'_I and K2 represents the ratio of F'_M to F'_S. hypothetically, it would seem if K1 and K2 are both very large for the conditions of the fluid in a given channel then the flow could reverse and the vapor slugs would propagate upstream; thus signaling a transition to flow instability.

1.7 Methods of Flow Visualization

Many methods to capture and document bubble phenomena and activity in microchannels have been used. The most common is through the use of a high speed high resolution (HSHR) camera operated from a computer. Typically these cameras achieve frame rates of 10,000 fps. In this set-up the camera looks down on the top of the test device through either a microscope objective or a camera lens, typically a “macro lens”. Usually the lens is selected on the amount of desired magnification of the channels in the test device, and the available lighting. A major limitation of this method is that it only provides a 2-D representation of the bubble activity in view, i.e., a bubble which is in contact with the top surface of the channel may be obscuring a liquid film below it. If a void fraction analysis were performed on this particular type of image it could result in a void fraction of 1 when in actuality the void fraction may be 0.7 or 0.6 and so on. Also, lighting is an issue due to the sometimes explosive nature of the boiling phenomena. For

most cameras shutter speeds of <10μs is required to clearly capture a bubble or a vapor front which is traveling or expanding at high rates of speed. If this condition is not met than the resulting image of the interface can become blurry or distorted making it difficult or impossible to analyze the image for void fraction or bubble velocity. One method to solve this problem is to use a laser to illuminate the flow. By doing this the pulse length of the laser determines the effective shutter speed of the camera and very short times intervals of exposure can be had. However, the laser requires the addition of a dye into the test fluid that will fluoresce when irradiated by the wavelength of the laser in use. The dye could alter the properties of the fluid in use, though typically when used in low enough concentrations it is not a problem Cullion [26]. Nonetheless it does increase the cost of the experiment. The laser is also useful in that it can increase the intensity of the light striking the surface of the test device over that of other lighting methods such as a halogen light. The high shutter speed reduces the amount of light allowed into the camera and thus can make the images very dark. Also, the laser provides a more constant intensity light level than that of other sources. When a halogen lamp is connected to AC power in a room the intensity can fluctuate with source of the power signal. This can be a problem when performing image analyses on the data acquired because the brightness of the images can vary from image to image in a given series comprising a single movie. If the analysis algorithm is dependent upon a threshold of some kind varying image intensity for a constant set of flow conditions can be extremely troubling.

Direct visual observation limits the type of devices which can be tested in that it requires the device be made with a port or other feature allowing optical access to the flow. Typically most parallel microchannel networks are constructed with a base

composed of a high thermal conductivity material and has either a polymer or glass top which is transparent and thermally insulative to meet this demand. This effectively eliminates a heat transfer path from the channel. In this situation heat is added to the flow through the channel sides and bottom and may sustain some minor losses through the channel top. This could change the bubble dynamics and phenomena that would occur if the channel was composed of four highly thermally conductive walls.

Finally, this method of imaging restricts temporal measurements of bubble phenomena to a local area on the test device. Due to the need for a high optical resolution at the vapor interface or location of the bubble in the channel a very small field of view is required. This prevents observation of the phenomena happening up or downstream of the field of view of the channel(s) under consideration as well as channels not in view at all. Being able to make a full field measurement across the extent of the device would be advantageous but would require several camera set-ups and would be exceptionally difficult to accommodate due to space limitations over the test device. Also, when this degree of resolution is needed typically the depth of focus of the lens is much less than the depth of the channel. This can make accurate detection of bubbles or vapor interfaces difficult because only when a bubble comes into the range of the depth of focus of the lens will the interface be clear enough to make measurements from.

Ide et al. [27] investigated nitrogen-water two phase flow in a 100μm transparent tube. In order to measure and document bubble phenomena they employed a method utilizing fiber-optic cables through which a beam of light was sent through the transparent tube under investigation. Two pairs of optical fibers of 250μm were spaced 0.25 mm apart at a distance of 36mm downstream of the t junction where the nitrogen gas

was injected into the water flow. Each pair of optical fibers were axially aligned with each other and separated across the diameter of the test tube such that a light signal traveling through one fiber of one pair would be incident on the test tube and once it had traveled through the diameter of the test tube would be received by the opposing optical fiber of the pair. The fibers were connected to an LED light source of wavelength 644nm. Each pair of fibers was connected to simple circuits which yielded a voltage signal that changed with amount of infrared light received. When a gas plug passed through one of the optical detectors the amount of light transmitted was low but when a liquid plug passed through the detectors the signal was high. Using this method they were able to achieve measurements at rates of 10 kHz, which, according to the above documented camera frame rates used in experiments with HSHR cameras should be sufficient to capture the bubble phenomena during flow boiling. The authors correlated each voltage signal with a corresponding image from a HSHR camera to qualitatively verify that the measurements with the optical detectors were correct.

The type of optical measurement used by Ide et al. [27] would be difficult to institute in an actual flow boiling apparatus due to the requirement the channels be optically transparent from at least two opposing sides. In order to simulate a heat source generally a heater need be made to contact with a thermally conductive material out of which the channels are formed; these materials are generally opaque. Also, in a network consisting of more than one channel several pairs of optical detector devices would be required complicating the experiment greatly. Also, these devices are subject to the limitation of local measurements of bubble phenomena rather than field measurements across the entire device. However, these devices are much less expensive than the more

conventional HSHR camera set-up and can provide very high rates of temporal measurements.

Walchli et al. [28] sought a method to forgo optical measurements of bubbles phenomena all together. They were interested in creating a system in which 3-D measurements of bubbles in devices that could have stacked channels with no optical access. They employed the method of X-Ray Tomographic Microscopy (XTM) visualization technique. Thus they made a single SI-glass microchannel of width 250μm and depth 100μm with which to test the technique. They discovered that each XTM image required 3 seconds of exposure time to get "sufficient" information of the interfacial gas-liquid boundary. Each experiment consisted of 1000 images and when the calibration images are included into the data set a single experiment required 1.5 hours of visualization time. Due to the excessive period of exposure time required the authors stated the only two phase flow regime this technique could be applicable for is annular flow since it is the only two phase flow configuration that is "temporally stationary".

Revellin & Thome [29] used a similar means of bubble detection and measurements Ide et al. [27]. Revellin & Thome [29] made flow observations in glass tubes of 0.509mm and 0.790mm in diameter and 20 mm in length. The test fluid was pumped through three sections of piping before entering the test section. In order they were: pre-heater, electrical insulator and micro-evaporator. These sections of the experimental set-up would generate bubbles to be observed in the glass test device. To measure bubble activity in the glass test section two lasers were employed. Both lasers were aimed at the glass tube and spaced at a distance of 70.63mm apart. The beam of each laser was focused through use of a lens on the glass test section. On the opposing

side of the glass tube two photodiodes captured the laser signals after passing through the tube. The photodiodes were set at a scan rate of 10 kHz and the resulting voltage signal was processed for bubble length, speed and frequency. Again this method of flow observation is subject to the same limitations as that employed by Ide et al. [27].

1.8 Fractal-Like Channel Geometry

Two major problems with microchannels used in cooling applications are a large pressure drop across the channel network and nonuniform temperature distributions along the channel wall resulting from the small diameter of the channel Alharbi et al. [30]. It is a concern that nonuniform temperature distributions in the heat sink could result in uneven thermal expansion of the component being cooled and thus damage it. Pence & Enfield [31] related that tapering a channel in the direction of the flow could reduce the maximum surface temperature but this would be accompanied by an increase in velocity of the flow through the channel resulting in an increased pressure drop, thus an increase in pumping power. To avoid this increase in pressure drop, or even provide a decrease in pressure drop, while improving temperature uniformity, fractal-like channel geometries have been investigated. In such a system each channel in the network divides into two or more "daughter" channels usually according to set length and diameter ratios.

Chen & Cheng [33] investigated a fractal-like microchannel network inspired by mammalian circulatory and respiratory systems. Their analysis showed the ratio of heat transfer rate to pumping power required to operate the device was much larger than for the traditional parallel channel array. In other words, the fractal-like design had a better benefit-to-cost ratio. For a given heat flux the pressure drop across the fractal-like design is substantially lower than for the parallel channel design so long as the branching level is

less than six. In the study of Chen & Cheng [33] a bifurcation number of two was chosen, meaning each channel bifurcated into two channels at the end of each branching level, and a branching angle of 90 degrees was selected, meaning each channel ended perpendicularly into the next branching level. They decided on four branching levels with both the length ratio and width ratio of each branching level were fixed at values of $\gamma = 2^{-1/2}$ and $d_{k+1}/d_k=2^{-1/3}$ respectively. The channels had a trapezoidal cross-section and the cross-section at the first branching level had a hydraulic diameter of 48.1μm.

Tests were completed on the device by pumping room temperature water through the network and making measurements of inlet pressure. The outlet of the device was open to atmosphere. They found that for laminar flow the pumping power required for the fractal-like geometry was between two and three times less than for a parallel channel array. From their results, as mass flow increased the ratio of pumping power for the fractal-like array to the parallel channel array became smaller, indicating improved performance at higher laminar flows.

In Pence [34] a fractal-like branching channel network consisting of 12 initial channels, 4 branching levels, a length ratio of $\gamma = 2^{-1/2}$ and a hydraulic diameter ratio of $\beta = 2^{-1/3}$ was studied numerically. The total length of the channels was 17.5 mm and the ending channel width was 100 μm and the channel depth was set at a fixed value of 250 μm for all channels. To compare the performance of this geometry, a system of parallel microchannels was also numerically analyzed. The hydraulic diameter of the parallel channel array was set equal to that of the ending branch level of the fractal-like network at 143 μm. The parallel network was then constructed of 77 channels 17.5 mm in length to create identical convective heat transfer area between both heat sinks.

Numerical tests were run on the two geometries under three different circumstances: identical flow rate, identical pressure drop and identical pumping power. A heat flux of 100W/cm^2 is applied to both channel geometries for all of the tests. For the identical flow rate condition the parallel channel configuration required 2.4 times the pumping power of and had a maximum wall temperature 10ºC greater than the fractal-like configuration. For identical pressure drop the flow rate in the parallel channel configuration was reduced to nearly half that of the fractal-like and the max wall temperature of the parallel channel system jumped to 106ºC (though boiling not taken into account) compared to the wall temperature of 60.4ºC reported for the fractal-like system. Finally, for identical pumping power the parallel channel configuration saw a maximum wall temperature of almost 30ºC higher than the fractal-like configuration. From these cases we see the fractal-like configuration demonstrates a higher benefit-to-cost ratio, the ratio of heat flux to pumping power, than the parallel channel configuration. As noted by Pence & Enfield [31], these trends hold for ratios of the convective heat transfer area of the fractal-like configuration to that of the parallel channel configuration greater than 0.5.

It appears the greater uniformity of wall temperature distribution and the lower pressure drop across the flow network is the direct result of flow phenomena near and at the bifurcation regions. Alharbi et al. [30] conducted a CFD analysis of a non-optimized fractal-like geometry proposed in Pence [32]. For the same flow conditions the fractal-like configuration had a 30% lower pressure drop than did the parallel channel configuration. Also in this analysis, it was found that as the fluid entered into the bifurcation region it decelerated due to an increase in cross-sectional area of 26% and at

each bifurcation a new laminar boundary layer was formed; boundary layer reinitiation was also confirmed in Alharbi et al. [35]. It is thought that this deceleration along with a secondary recirculation at the bifurcation region maybe responsible for the pressure recovery of the flow and further it appears the magnitude of recirculation is heavily dependent on the angle of the bifurcation Alharbi et al. [30]. In Alharbi et al. [35], further CFD analysis was run on the same geometry employed in Alharbi et al. [30]. Plots of the average wall temperature profiles showed the temperature rose according to an exponential growth pattern which increased along the length of the channel until a bifurcation was reached at which point the temperature profile dropped of sharply; at each bifurcation the temperature returned to nearly the initial value of the wall temperature at the inlet of the network. This behavior appears to coincide with the redevelopment of the boundary layers at the bifurcations. Also included in the results was an analysis of two different fluid paths possible for a fluid particle to travel through during its residence time in the flow network. Plots for the inner, outer and bottom wall temperatures along these paths were presented and from them it is shown that along all the paths the temperature profile spikes, with the exception of the k=1 bifurcation possibly because of the symmetric nature of this bifurcation. For all the other bifurcations it was found flow separation occurred just after the bifurcation and set-up a zone of recirculating fluid to which is attributed the sharp spike in wall temperature. However, there is also a secondary flow field occurring at the bifurcations which is strongly dependent on the angle of bifurcation Alharbi et al. [35]. In path one the branch angles were much larger than those of path two. For each bifurcation it was found that a "swirl" occurred which transported cool fluid from the center of the flow to the channel

wall. Thus a swirl of stronger magnitude resulted in a lower wall temperature. In path two the shallow branching angles gave rise to a swirl around 30% of the streamwise velocity, whereas the sharper branching angles found in path one resulted in a swirl around 50% of the streamwise velocity. This seems to be in agreement with the larger wall temperature spikes observed in path two versus path one. Perhaps a fractal-like flow network with sharper bifurcation angle that are also symmetric would result in stronger swirl thus lowering or eliminating the temperature spikes as is foreshadowed by the results for the k=1 bifurcation in the above results. Thus the geometry of the fractal-like branching network is very important regarding the performance of the device.

Another significant area of interest regarding the fractal-like flow networks is how they distribute vapor during flow boiling as well as how they handle the upstream flow of vapor if the flow were to become unstable. In Muwanga et al. [21] the microchannel test device was altered by cutting three cross-directional channels into the parallel network. The idea behind this was to give the upstream bound vapor in a channel an alternate path to prevent it from reaching the inlet plenum. This is somewhat similar to the way a fractal-like flow network could handle the upstream flow of vapor because at each branching level with the exception of the zeroth level once the vapor reaches the inlet of a channel it first encounters a bifurcation before continuing upstream. The bifurcation presents the vapor with an alternate flow path. Thus it can bend around the bifurcation and flow down stream in the adjacent channel.

Earlier it was discussed the manner in which the generation and presence of vapor in a channel produces an increase in the pressure drop of the microchannel test device. In the present study it is desired to investigate the effect of a fractal-like branching

microchannel network on the magnitude and distribution of the void fraction under given boiling flow conditions on the pressure drop across the test device. In addition to this, it is desired also to investigate the effect a fractal-like geometry has on two-phase instabilities with and without separating the test device from the upstream control volume and also investigate the behavior and phenomena of vapor in the flow network especially in the regions at and near the bifurcations.

2 Experimental Set-up & Procedure

2.1 Test device

The test device, shown in fig.2.1, is a disk of diameter 38.1 mm and is composed principally of two parts; a silicon bottom and a Pyrex® top. The bottom of the test device was made from silicon due to its high thermal conductivity 150 W/mK. This was needed to ensure a uniform heat flux across the entirety of the bottom of the test device. The top was made of Pyrex due to its low thermal conductivity 1.5 W/mK and its optical transparency. This was needed to ensure the lowest rate of heat transfer possible while maintaining an optically transparent top surface. Both the top and bottom parts of the test device are of the same diameter and each are 0.5 mm in thickness.

Channels were dry reactive ion etched (DRIE) 0.25mm deep into the silicon layer. The channel pattern employed was based on the results of an optimization study by Pence & Enfield [31]. The channels are rectangular in cross-section and the channel dimensions are governed by fixed length and width ratios dictated by results from Pence & Enfield [31]. It should be noted the channel lengths are presented based on radial distances from the inlet and are not the actual lengths of the channels. At the zeroth branching level there are 16 initial channels, corresponding to a total of 16 trees as shown in fig.2.2,

which, through a series of bifurcations, transition to 256 channels at the fourth and ultimate branching level. The dimensions of the channels are listed in table 2.1.

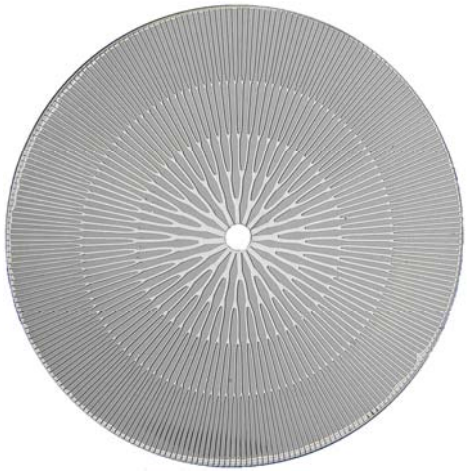

Figure 2.1: Typical test piece used in present experiment. Fluid enters at the center of the device and flows radially outward through the channel network.

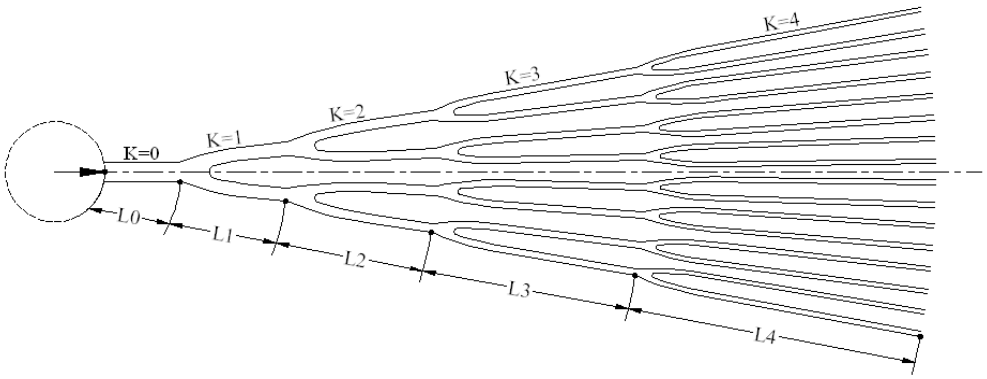

Figure 2.2: Diagram of a "tree" system of channels in the test device.

Table 2.1: Dimensions of channels in test device.

k level	No. of branch	Depth (μm)	Width (μm)	D_h (μm)	Length (mm)
0	16	250	400	308	1.6
1	32	250	283	265	2.27
2	64	250	200	222	3.21
3	128	250	141	180	4.54
4	256	250	100	143	6.42

After the channels had been etched into the silicon disk the Pyrex® top was anodically bonded to the top surface of the silicon disk forming the fourth wall of the channels. On the bottom side of the silicon disk opposite of the channel side a 1μm thick layer of silicon dioxide SiO_2 was grown and on top of this three Nichrome rings of 0.5μm thickness were chemically deposited. Lastly a final layer of SiO_2 1μm in thickness was deposited over the Nichrome rings. The entire bottom of the test piece, except for 6 small pads used to make electrical contact on the Nichrome rings, was insulated with SiO_2, as shown in fig.2.3. The Nichrome rings were used to generate heat by passing an electrical current through them. The heaters were not extended to the periphery of the test device due to concerns of melting the o-ring gasket material. However, it was believed that due to the high thermal conductivity of silicon the heating of the test fluid would remain uniform over the extent of the test piece. The test fluid exits the device into an open annular plenum, thus exit conditions are taken to be the recorded atmospheric temperature and pressure.

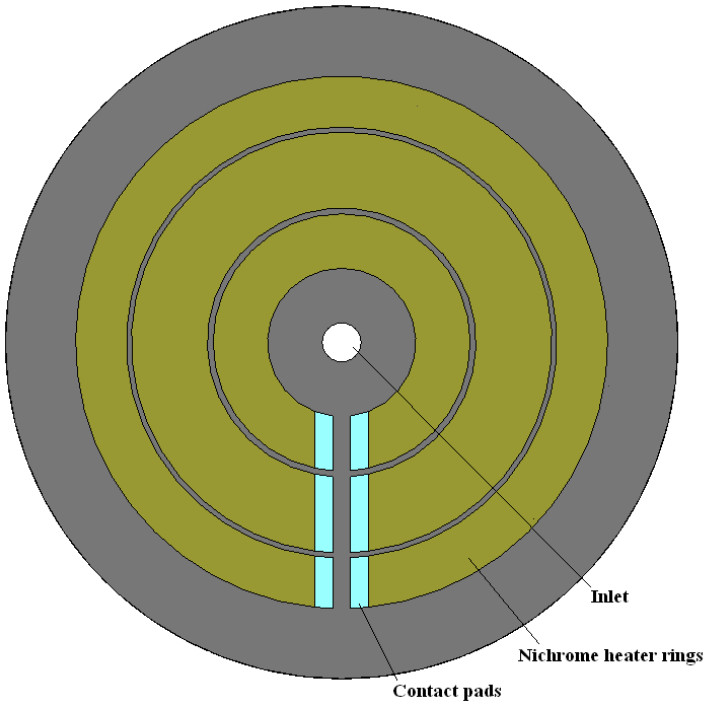

Figure 2.3: Nichrome heater rings on the bottom of the fractal

2.2 Flow Loop and Instrumentation: The Manifold

The manifold, shown in fig.2.5, was designed to connect the test piece with the flow loop. Also, it provided a means to measure inlet pressure and temperature of the test fluid as well as supply electrical current to the heaters on the bottom of the test piece. A circular lid with a hole cut out of the center was placed onto the top of the manifold allowing optical access to the test device during operation. The test device was held in place by a vacuum pulled through the vacuum chuck, shown in fig.2.4, located in the center of the manifold. On the top of the vacuum chuck four 1.6mm diameter equally spaced holes were drilled through which the vacuum was applied to the fractal. Two o-rings located at the inlet and outer radius acted as the interface between the test device and the vacuum chuck and also sealed the underside of the fractal outside of the inlet to prevent leaking.

When the vacuum was applied to the test device it was pulled down onto six gold pogo pins which connected to the contact pads and served as a means to connect the Nichrome heaters to the power sources which supplied electric current. Each pair of pogo pins connected one of the Nichrome heaters to an independent power supply. The pogo pins were mounted on top of individual springs allowing them to exert a force on and maintain contact with the contact pads. The pins protruded through the top of the vacuum chuck via six 0.94mm holes drilled through the top surface of the vacuum chuck.

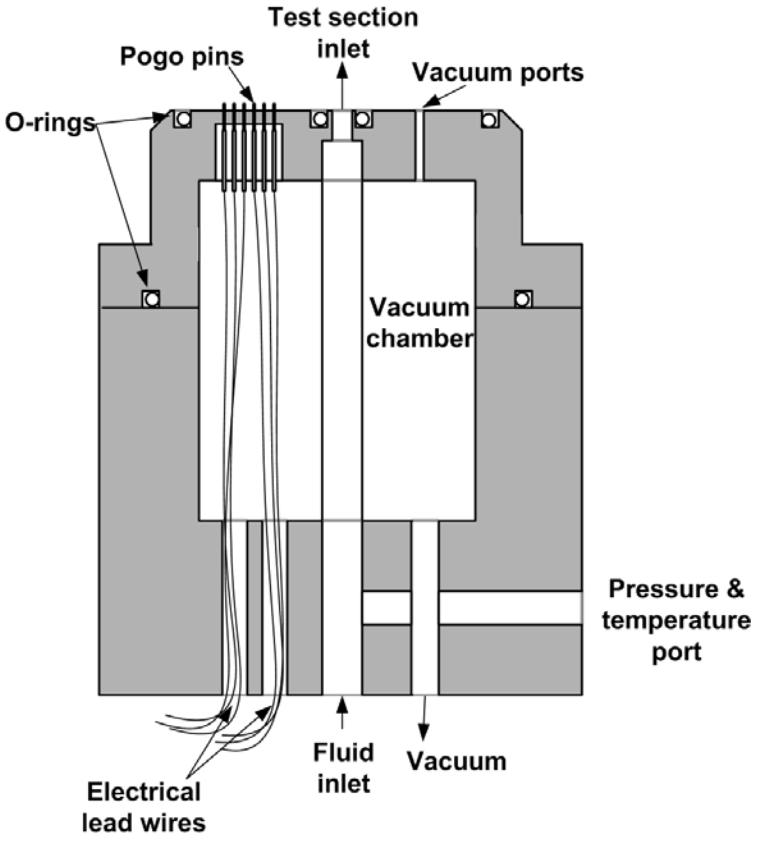

Figure 2.4: Cross-section of vacuum chuck.

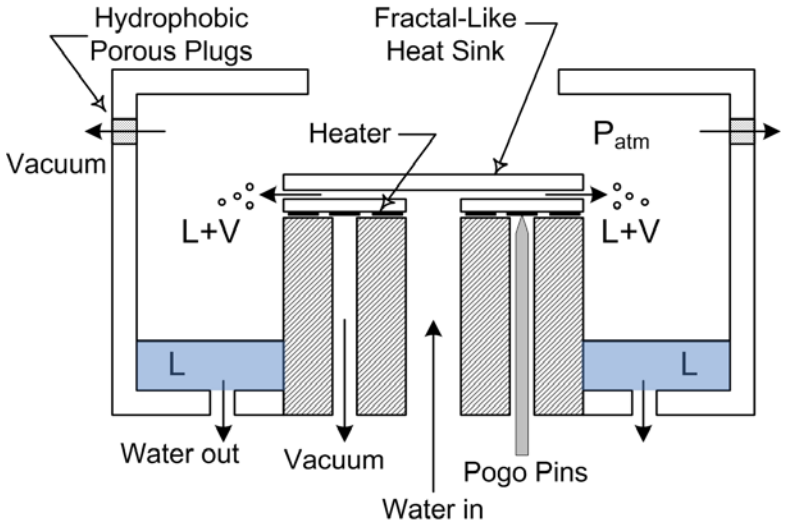

Figure2.5: Cross-section of the manifold and test device[1].

2.3 Flow Loop and Instrumentation: The Flow Loop

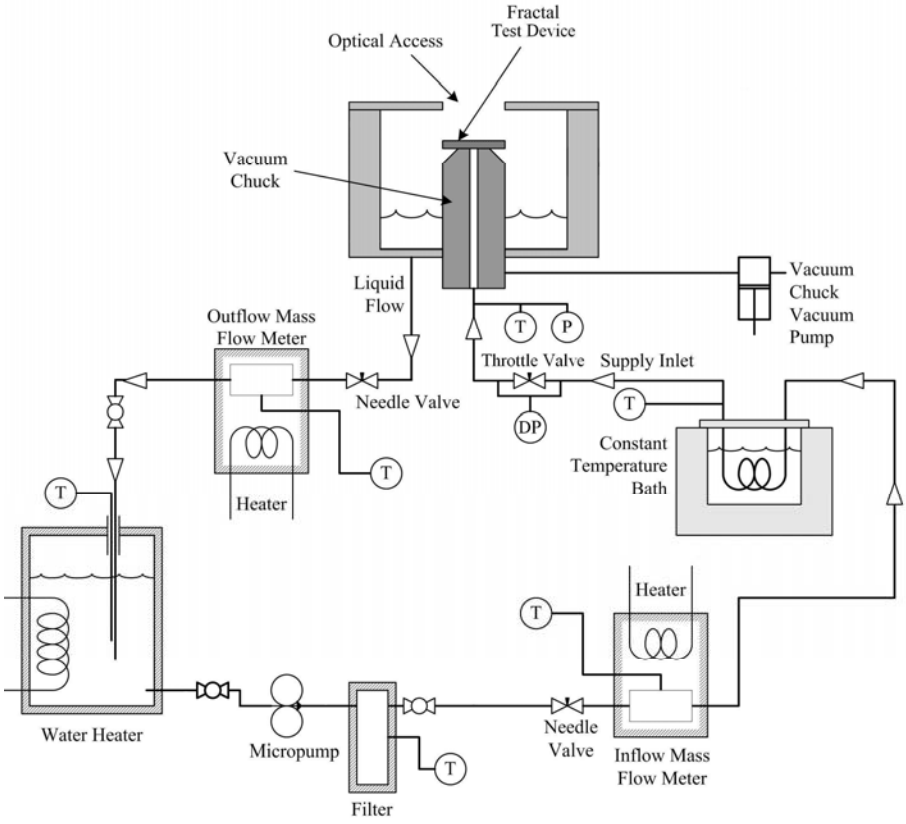

Figure 2.6: Diagram of flow loop used in experiment.

[1] Figure created by Brain Daniels, Graduate Student, Oregon State University.

Figure 2.6 details the components of the flow loop used in the present study. The working fluid was held in a 2000W 6 gallon Vanguard water heater. The temperature of the fluid was maintained using an Omega iSeries controller having an accuracy of 0.02°C connected to a T-type thermocouple. From the water heater the fluid was fed to a Micropump gear pump, which drove the fluid through the flow loop at a constant rate. The pump was powered by a 115V DC power supply. The fluid passed through a Shelco 10 μm filter to filter out any impurities that could damage the test device or cause the fluid to boil prematurely. Then the fluid passed through a needle valve used to regulate the flow rate in addition to the adjusting the speed of the pump head. Following the needle valve a Micromotion Coriolis mass flow meter with a flow range of 0 to 1370 g/min and an accuracy equal to 0.10% of the rate is used to measure the inlet fluid flow rate.

The fluid is then driven through a Neslab 800W constant temperature oil bath to heat the fluid to the desired inlet temperature. The fluid travels through insulated Nylon tubing to the throttle valve before entering the manifold. The throttle valve was produced by Ideal Valve Co. model 52-2-11 with 56 threads/inch for precision metering.

The fluid then enters into the vacuum chuck and into the test device. Exiting the test piece the fluid pools in the manifold until it is drained out. Once the fluid exits the manifold its flow rate is regulated by another Ideal Valve Co. needle valve model number 52-3-11. Then the outlet flow rate is measured using a second Micromotion Coriolis mass flow meter and then the fluid exits into the water heater thus completing its traverse around the flow loop. All of the tubing in the flow loop is clear 6.35mm (¼")

polyethylene tubing with the exception of the 20.32 cm (8”) section of 6.35mm (¼”) stainless steel tubing connecting the throttle valve to the vacuum chuck in the manifold.

2.4 Determination of Test Cases

The single largest criteria for deciding the flow rate and heat flux the test device was operated at is manufacturing defects of the test device itself. Initially 16 identical test devices were constructed. However, due to the complex nature of the test pieces themselves the manufacturer only agreed to guarantee a best effort regarding the outcome of the final product. The test pieces looked to be usable; the visible defects being scratches or pock marks on the surface of the Pyrex, misalignment of the test piece inlet and the beginning of the channels, a few channels blocked on one test piece, and misalignment of the Pyrex and Si layer. However, all the test pieces suffered from a critical malady; an insulating layer had been deposited or grown over the contact pads where the pogo pins delivered the flow of electric current. Without correcting this problem the test pieces would be useless for the studies needed to be done.

Initially it was desired to select a test case based on what flow regimes we could expect at different heat fluxes and flow rates. However, since studies employing the channel geometry of the test pieces was undocumented in the literature and no flow map was known an experimental determination of flow regimes was required. Unfortunately in this process the Nichrome heaters on multiple test pieces were rendered useless due to the occurrence of electric shorts between contact pads. In this case current would flow between contact pads of separate rings rather than around the intended ring. Thus only a small area located by the contact pads would receive heating thereby destroying the capacity of the test pieces to have a uniform heat flux.

It was determined through numerous preliminary tests that the largest energy input that could likely be tolerated by the test devices was 40 watts. In other words this was the energy level at which no shorting had been found to occur. Two initial test conditions were determined by setting the heat input under the maximum allowable level and using the numerical model[2] to determine the flow rate that would produce an exit quality under 0.1 to avoid "dry-out" conditions in the channels of the test-device. Using this scheme the test conditions of (1) 20 watts heat input, 20 g/min inlet flow rate, 88 deg. C inlet temperature and (2) 30 watts heat input, 30 g/min inlet flow rate, 88 deg. C inlet temperature were determined. However, once the initial data was acquired it was found that little to no vapor activity occurred in the test piece. When it did occur it happened as isolated bursts both in time and location on the fractal. Whenever one of the bursts of vapor activity occurred it occupied only 3-4 neighboring trees of the 16 which comprise the test piece. Thus it was determined because of the spatial and temporal intermittency of vapor activity that different and more interesting conditions were needed for the investigation of the test device.

As it had been decided the heat input should not be increased beyond the amount already being supplied to the test piece so it was determined to lower the mass flow rate. For the 20 watt heat input case the flow rate was lowered to 10 g/min holding the inlet temperature constant at 88°C. For this condition the numerical model predicted boiling initiation close to the middle of the K4 level, which is the last branching level shown in fig.2.2. Initially global movies were recorded of the test piece operating at the 10g/min,

[2] Daniels et al. [4]

20 watt conditions. These movies demonstrated sustained vapor activity over the extent of the test piece.

Also, it was desired to investigate the effects of adding a control valve to throttle directly upstream of the inlet of the test device. It has been shown in parallel microchannel networks the addition of such a throttling valve can suppress certain hydrodynamic instabilities by Qu and Mudawar [18]. In order to show the benefits of the test device geometry employed in this study it was desired to compare the effect of the throttle valve on average void fraction in the test device as well as inlet pressure, temperature and flow rate of the test device.

Also, it was desired to investigate the effects of increased amounts of vapor in the test device on inlet temperature, pressure and flow rate. However, due to the excessive time required to acquire and reduce void fraction data it was determined to omit those parameters from the test plan of this study. It was found that the largest pressure drop across the throttle valve upstream of the inlet which the experimental facility could produce was 150 kPa. Thus the pressure differential across the throttle valve was incrementally increased up to the maximum value while measurements of inlet pressure, temperature and flow rate as well as observations of flow phenomena were made. It was shown that the maximum differential pressure across the throttle valve demonstrated the most pronounced effects on the measured values listed above. Therefore, it was determined to use this value of pressure drop across the throttle valve for this study.

Table 2.2: Test matrix to be employed in this study. Diameter of test piece is 38.1 mm.

	10 g/min, 1.76 W/cm^2, 88°C		10 g/min, 2.64 W/cm^2, 88°C	
desired measurements	150 kPa throttle	no throttle	150 kPa throttle	no throttle
average void fraction	X	X		
inlet pressure	X	X	X	X
inlet temperature	X	X	X	X
inlet flow rate	X	X	X	X

Table 2.3: Uncertainty in Measured flow conditions. The calculations can be found in appendix D.

	Flow rate (g/min)	Input heat flux (W/cm^2)[3]	Inlet temperature (°C)	Inlet pressure (kPa)	Pressure drop across fractal (kPa)
Throttled	+/-0.24	+/-0.21	+/-0.28	+/-0.36	+/-2.69
Non-Throttled	+/-0.73	+/-0.21	+/-0.41	+/-0.36	N/A

2.5 Determination of Heat Input

Initially the fact that the Nichrome heaters did not extend over the entire extent of the test device raised concerns of the possibility of non-uniform heating. However, because of the high thermal conductivity of silicon this was believed not to be a problem.

It was necessary to determine the amount of energy to supply to each of the Nichrome heater rings to ensure uniform heat flux along the base of the test piece. Three different area schemes were considered to define the effective area over which each heater was responsible to deliver a uniform heat flux. The first defined the effective area

[3] These values are for the 1.76 W/cm^2. the uncertainty values for the 2.64 W/cm^2 will be double those shown in table 2.3.

for the inner heater ring (A_i) as extending from the radial location of the inner o-ring to the midpoint between the inner and middle heater rings, the effective area of the middle ring (A_m) as extending between the midpoint of the inner and middle heater rings to the mid point of the middle and outer heater rings and the effective area of the outer heater ring (A_o) as extending from the midpoint between the middle and outer heater rings to the radial location of the outer o-ring. In the second scheme A_i is defined as extending from the inner radius of the inner heater ring to the mid point between the inner and middle heater rings, A_m is defined as extending from the midpoint between the inner and middle heater rings to the midpoint between the middle and outer heater rings and A_o is defined as extending from the midpoint between the middle and outer heater rings to the outer radius of the outer heater ring. In the third scheme A_i is defined as extending from the radius of the inlet hole to the midpoint between the inner and middle heater rings, A_m is defined as extending from the midpoint between the inner and middle heater rings to the midpoint between the middle and outer heater rings and A_o is defined as extending from the midpoint between the inner and middle rings to the outer radius of the test piece.

It was thought that due to the high thermal conductivity of Si scheme (c) in fig.2.7 would produce the best results because it was believed to be the most certain of delivering a uniform heat flux to the bottom of the test device. Schemes (a) and (b) both had substantially smaller areas for the inner and outer rings than scheme three and it was thought they would result in large concentrations of energy delivered in one place. The way the heat flux applied to the test device is presented is defined in terms of the heat energy supplied to the test device divided by the entire area of the bottom of the test device, i.e., (c).

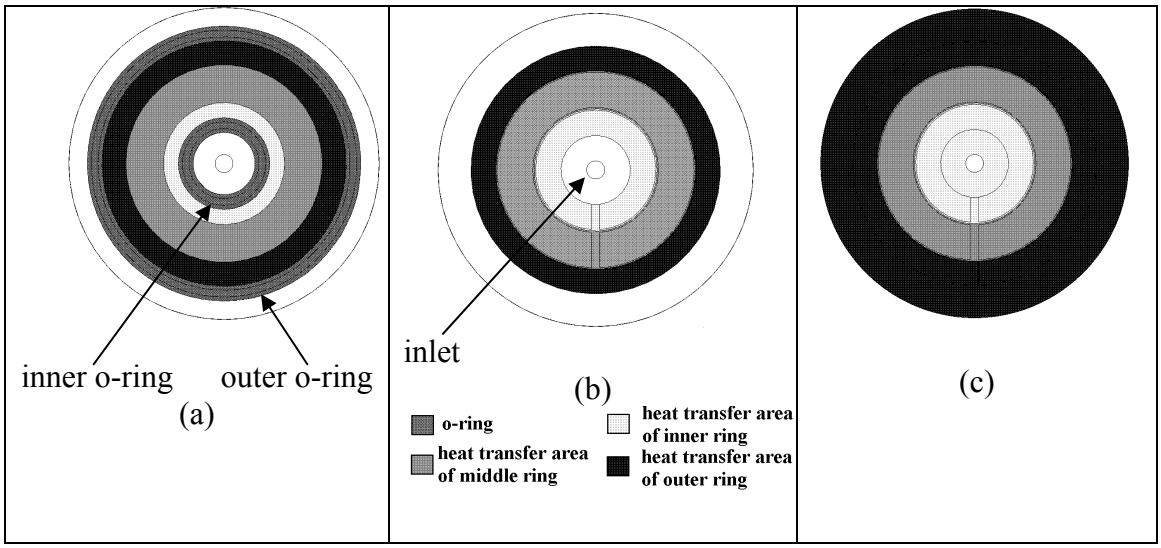

Figure 2.7: scheme of effective heat transfer areas for each of the heater rings. (a) Shows the scheme governed by the location of the heater rings, (b) shows the scheme governed by the geometry of the heaters only and (c) shows the scheme governed by the entire bottom area of the test device.

To determine the energy to send to each heater ring during the experiment, the desired heat flux was first calculated by dividing the desired amount of energy input, 20 or 30 watts, by the total area of the test device bottom. The value calculated for the desired heat flux was then multiplied by the three different areas calculated based on the location of the three heater rings and this generated three separate values of power to be sent to the inner, middle and outer heater rings.

2.6 Experimental Procedure: Mounting the Test Piece

Each experiment was done according to the following procedure. Three multi-meters were connected to the wire leads attached to the pogo pins and set to measure resistance. Next the contact pads of the Nichrome heater rings located on the bottom of the test piece were visually aligned with the pogo pins. When the alignment looks correct the fractal was pressed down onto the vacuum chuck. When contact was made between the heater ring contact pads and the pogo pins the resistance of each heater ring was

displayed on the multi-meters. If the resistance values matched those which were measured directly from the test piece and the inlet of the fractal looks to be aligned concentrically with the outlet of the vacuum chuck then the vacuum pump was engaged and the test piece sucked down onto the o-rings on top of the vacuum chuck.

Once the test piece was securely seated on the vacuum chuck a circular bubble type level was placed on top of the test piece to ensure the fractal was level, at least to the human eye. If the bubble in the level was off center the stage which the manifold was attached to was adjusted until the bubble comes to center. This was an important step in minimizing the shift in the channel depth at which the microscope is focused as the lens was moved across the test piece.

It is important to align the test piece concentrically with the outlet of the vacuum chuck because misalignment reduces the effective pressure gradient across the flow loop from pump outlet to fractal inlet thereby reducing the maximum possible flow rate. Also, a misalignment was thought to potentially hinder repeatability of the flow conditions.

2.7 Experimental Procedure: Preparing the flow loop

Deionized distilled water with McCormick black food dye added at a ratio of 6ml/gallon H_2O was gravity fed into the water heater. After 4 gallons of the working fluid had been added to the water heater, the fluid was vigorously boiled for one half hour in order to ensure it was properly degassed as was done by Cullion [26]. After the half hour boiling period was complete the working fluid in the water heater was held at a constant temperature of 85° C.

Next the fluid was pumped through the flow loop bypassing the manifold. During this time the oil bath was brought to 96°C. Also, the flow meters, being the largest heat

sinks in the flow loop, were warmed using heating blankets. When the fluid temperature measured by the inlet flow meter reached 70°C the warm up of the flow loop was complete. Next the fluid was diverted to the manifold and passed through the test device.

The inlet flow rate was then set to 10 g/min. For the case without throttling at the inlet, this is achieved by setting the power supply of the pump to roughly 95% of the voltage capacity of the pump. And then throttling down the needle valve directly upstream of the inlet mass flow meter until the 10 g/min flow rate was achieved. By operating the pump in the upper 90% of its range it was found that more consistent flow rates occurred.

For the case with throttling at the inlet, the low flow pump head on the pump was replaced with the high flow pump head. This was needed to achieve the desired pressure drop across the inlet throttle valve. In this case the pump was operated at its maximum capacity and the needle valve directly upstream of the inlet mass flow meter was totally disengaged. The inlet throttle valve was then engaged until the 10 g/min flow rate was achieved. When the 10 g/min inlet flow rate was obtained then the desired pressure drop across the throttle valve was obtained simultaneously.

Additional energy was added to the working fluid via a rope heater wrapped around the stainless steel tube located at the inlet of the vacuum chuck. The rope heater temperature was increased using the variac, which was set at a voltage output of roughly 52 volts. This in conjunction with the energy input by the oil bath achieved an inlet temperature of 88°C at the test device.

Once the desired inlet temperature was achieved, energy was then added to the flow in the test device by means of the Nichrome heaters located on the bottom of the test

device. Energy was supplied to the Nichrome heaters with three independent DC power supplies. The voltage supplied to the heaters was incrementally increased at a rate of 2 Watts/min to ensure a slow enough rate of heating to prevent the Pyrex from cracking due to the large difference of coefficients of thermal expansion of Pyrex and Si. This continued until the 20 watt or 30 watt total heat input criteria was satisfied.

The needle valve controlling the manifold outlet flow rate is set to maintain a constant fluid level in the manifold. The actual level in the manifold was not determined to be critical but needed to be somewhere below the level of the test piece in order to keep the exit of the test piece at atmospheric conditions. Once this level was set the partial lid, covering all but the top of the test piece, is placed over top of the manifold and the manifold and stage are slid into place under the microscope. Next a small 12 VDC fan stripped from a used computer is mounted on the partial manifold lid oriented such that the generated air stream passes underneath the microscope objective. The fan is set to its maximum power. The purpose of this is to clear the vapor away from the objective lens in order to avoid vapor condensation on the lens.

The z-traverse of the stage is adjusted until the top of the Pyrex layer comes into focus. This is determined by identifying a scratch or surface imperfection in the Pyrex layer and bringing it into focus as is seen on the view window of the phantom software on the laptop. Once this reference point is established the z-traverse is raised 625 microns to bring the focal plane into the middle of the channel depth. However, the focal depth of the 5X objective is determined to be 58.8 microns[4] so an additional 25 microns is added to the 625 microns bringing the total z-traverse adjust to 650 microns.

[4] Measured by Mr. Younghoon Kwak, Graduate Student, Oregon State University

After all these steps were complete the system was allowed to run for at least 30 minutes in order to reach steady state conditions before any data was collected.

2.8 Flow Visualization

A Phantom V5.0 high speed high resolution (HSHR) camera is used to capture movies of flow phenomena in the test piece. The camera was set to capture movies at 1000 frames per second with an exposure time of 10μs. A 1000 fps frame rate was selected to acquire data and was shown to accurately capture void fraction variations by Cullion [26]. 10μs is the shortest exposure time the camera is capable of and necessary to capture the fast moving vapor activity with minimal blurring of the vapor-liquid interface. The camera is mounted on top of a Leica Leitz Ergoplan microscope using a 5X objective which overlooks the test piece. The microscope coupled with the 5X objective yielded a resolution of 0.198 pixels per micron. The camera is connected to a laptop which is loaded with the phantom software to operate the camera.

The manifold is mounted on a Thor Labs, Inc. LJ750 three dimensional translation stage. To visually access different areas of the test piece the entire manifold is moved under the stationary microscope. The stage is also used to focus the camera on the desired area of interest.

A diagram of the flow visualization set-up sued in the present study is shown in fig.2.8. A halogen light source was used to illuminate the test piece. A StockerYale Mille Luce M1000 halogen light source was connected to the microscope via a fiber-optic cable. The light travels through the microscope housing and is diverted by a series of mirrors and exits vertically through the objective. Thus the light strikes the test piece normally. The beam of light is focused by the objective. Unfortunately this created a

shadow region in the channel next to the channel walls as is shown in fig.2.9. This is a cause of problems regarding image analysis discussed in the data reduction section.

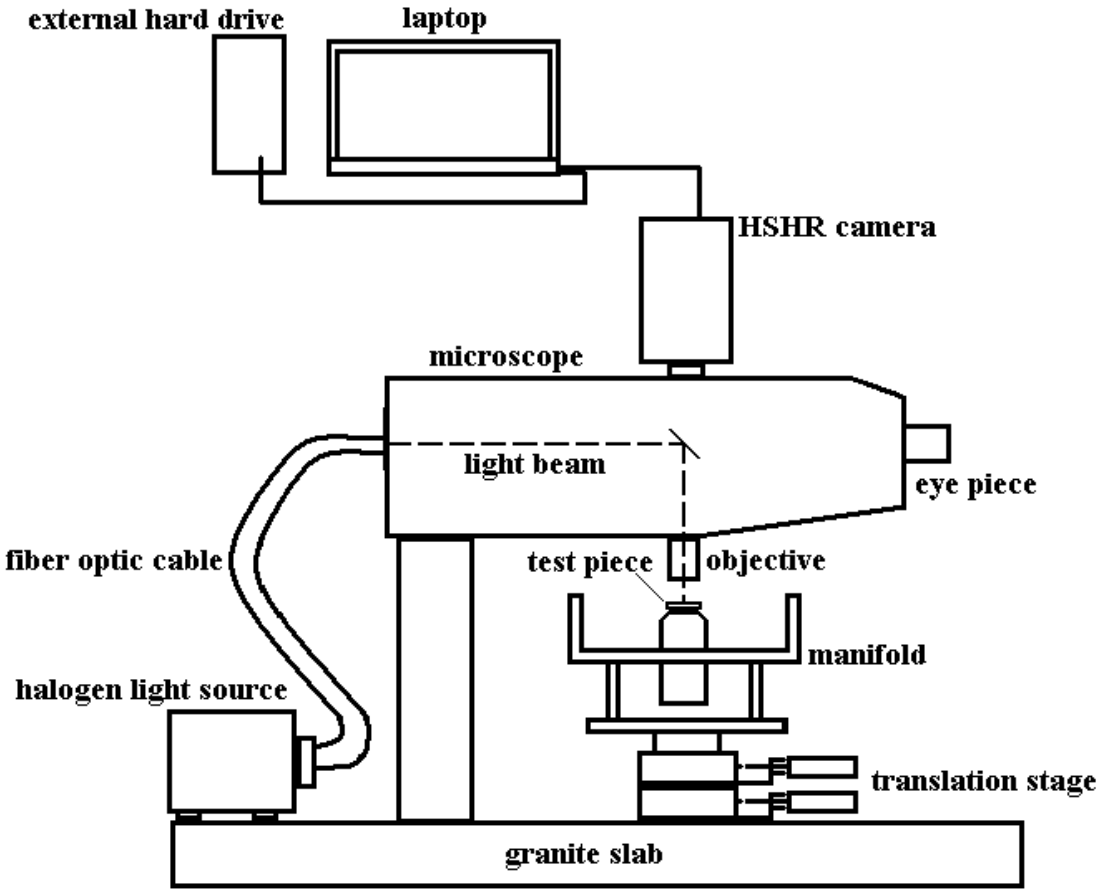

Figure 2.8: Diagram of the flow visualization set-up.

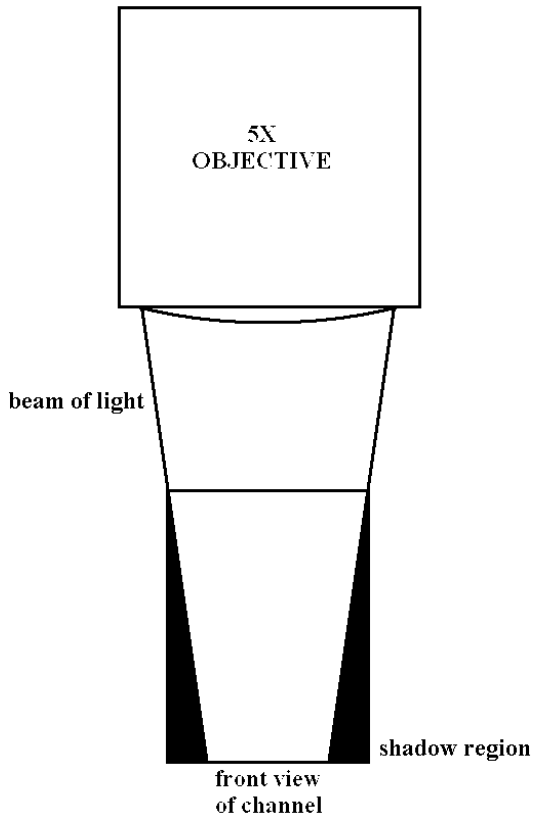

Figure 2.9: Shadow cast by channel walls as a result of the optical properties of the microscope objective

2.9 Data Acquisition

Pressure, temperature and flow rate conditions, as well as voltage supplied to the heater rings, were recorded using virtual instruments created with Labview software. Data was sampled at 200Hz and the values were stored in the computer's internal memory until 1000 total samples had been collected at which time the 1000 samples were averaged and written to a specified file. This effectively provides an average value of the conditions every 5 seconds. The only exception to this is the inlet pressure. It was sampled and recorded according to the aforementioned method; however it was also sampled at 500Hz without being averaged in order to investigate the potential higher frequency inlet pressure fluctuations.

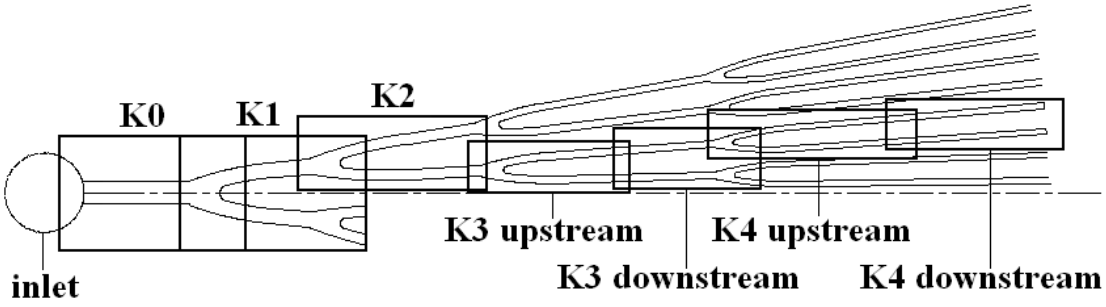

Figure 2.10: Diagram of the different "fields of views" over which movies were recorded.

To document the local vapor phenomena as well as record images to be used in determining local void fraction sets of 250 movies were recorded over a series of 7 locations for each test case as shown in fig.2.10. The recorded movies are stored on the internal flash memory of the camera until its 1 GB capacity is reached. After this they are uploaded to a specified location on the Lacie "d2 extreme" external hard drive. The Movies are saved as multi-paged tagged image file format (TIFF) files each of which has an accompanying camera header data (CHD) file which contains all the information of the camera settings including frame rate, time stamps, etc.

Previous work on a different geometry of a fractal-like branching channel test piece had shown that more than 15 movies were required in order to establish an average void fraction at a given location on the test piece. Initially it was unknown how many movies would be needed for this so a number of 250 movies was decided upon to ensure enough movies were collected to find an average void fraction value at one time at a given location on the test piece. The continuous record feature on the camera manufacturer supplied software was employed to accomplish this. Rather than record each of the movies individually they were named according to the manufacturer

prescribed convention recorded continuously. Once a movie had been recorded it was uploaded directly to the external hard drive. Once the download was complete the next movie was recorded and the process was repeated until the desired number of movies had been acquired. The time interval between movies varied depending upon the resolution setting of the camera. If the resolution size was set 512 pixels X 512 pixels the time to record and download 1019 frames was much less than if the resolution was set to 1024 pixels X 1024 pixels.

2.10 Data Analysis

The recorded movies were analyzed for void fraction, α, using an image processing program created in Matlab with the image processing toolbox[5]. Details of the program can be found in appendix B. The first step was to select an all liquid image from a movie to define the channel boundaries used to analyze all other movies taken at that location. The image chosen was binarized such that all the pixels in the region defined as the channel were white and the remainder of the pixels in the image was black. The channel was defined as beginning immediately after the bifurcation of the upstream branching level and immediately before the bifurcation of the downstream branching level as shown in fig.2.11. More specifically the beginning of the channel region was defined by the radius from the inlet of the test device which passed through the apex of the bifurcation immediately upstream.

[5] Created by Douglas Heymann, Graduate Student, Oregon State University

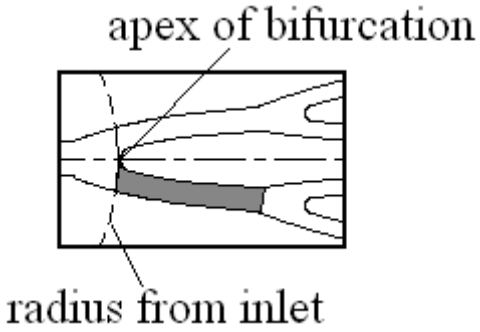

Figure 2.11: definition of channel area in Matlab image processing algorithm. Channel area is filled with gray.

The program read in every image individually from each movie and performed a series of morphological operations to manipulate each image and eventually binarize each image making regions containing vapor filled with white pixels and regions containing liquid filled with black pixels. The void fraction was then defined as the number of white pixels in the image being analyzed, WP_{img}, divided by the number of white pixels in the base image used to define the channel boundaries, WP_{base}, as shown in eq.2.1.

$$\alpha = \frac{\sum WP_{img}}{\sum WP_{base}} \qquad 2.1$$

Thus the void fraction calculated is based on the apparent area of the voids in the channels and is not a true volume void fraction. The parameters that determined the morphological operations were set by selecting a set of movies over the range of movies collected for a given location and test case on the test device and then using that set of movies to optimize the program. This optimization process involved visually comparing raw images of the movies with the processed images once the algorithm was finished. If the algorithm had created a region of white pixels where by visual inspection a bubble

appeared on the raw image the parameter settings of the algorithm were kept if not they were adjusted until the raw image and the process imaged matched up. The program was also tested to ensure all liquid raw images produced black processed images and all vapor raw images produced white processed images.

3 Results & Discussion

3.1 Global Inlet Pressure Characteristics of Test Device

3.1.1 Periodic Filling of the Inlet Plenum with Vapor

In all of the test cases in the present experiment the inlet pressure was seen to oscillate at regular periodic intervals. The characteristic oscillation of pressure measured at the inlet of the test device used in the present study is in agreement with what has been found in the literature for microchannel flow networks undergoing flow reversal. It is desirable to understand how the pressure characteristics change with increased amounts of vapor, hence an increase in heat flux for a given mass flux. Also, the present study investigated the effects of throttling the flow at the inlet of the device, similar to Qu & Mudawar [15], on inlet pressure and flow phenomena throughout the test device.

In the vapor-liquid cycle depicted in fig.3.1, the time interval between the frames in which vapor first enters the inlet plenum to the time when the last of the vapor leaves the inlet plenum is denoted as “vapor residence time”, τ_{vr}. Similarly the time between frames in which the last of the vapor leaves the inlet plenum to the time in which the next vapor slugs enter the inlet plenum is denoted as “liquid residence time”, τ_{lr}. Each vapor residence time is followed by a corresponding liquid residence time. The total time of one cycle, τ_c, is the sum of the vapor residence time, τ_{vr}, and one liquid residence time, τ_{lr}.

$$\tau_c = \tau_{vr} + \tau_{lr} \qquad 3.1$$

In the cycle depicted in fig.3.1 the vapor residence time begins when vapor enters the inlet plenum after frame 148 and ends when vapor completely exits the inlet plenum shortly before frame 256.

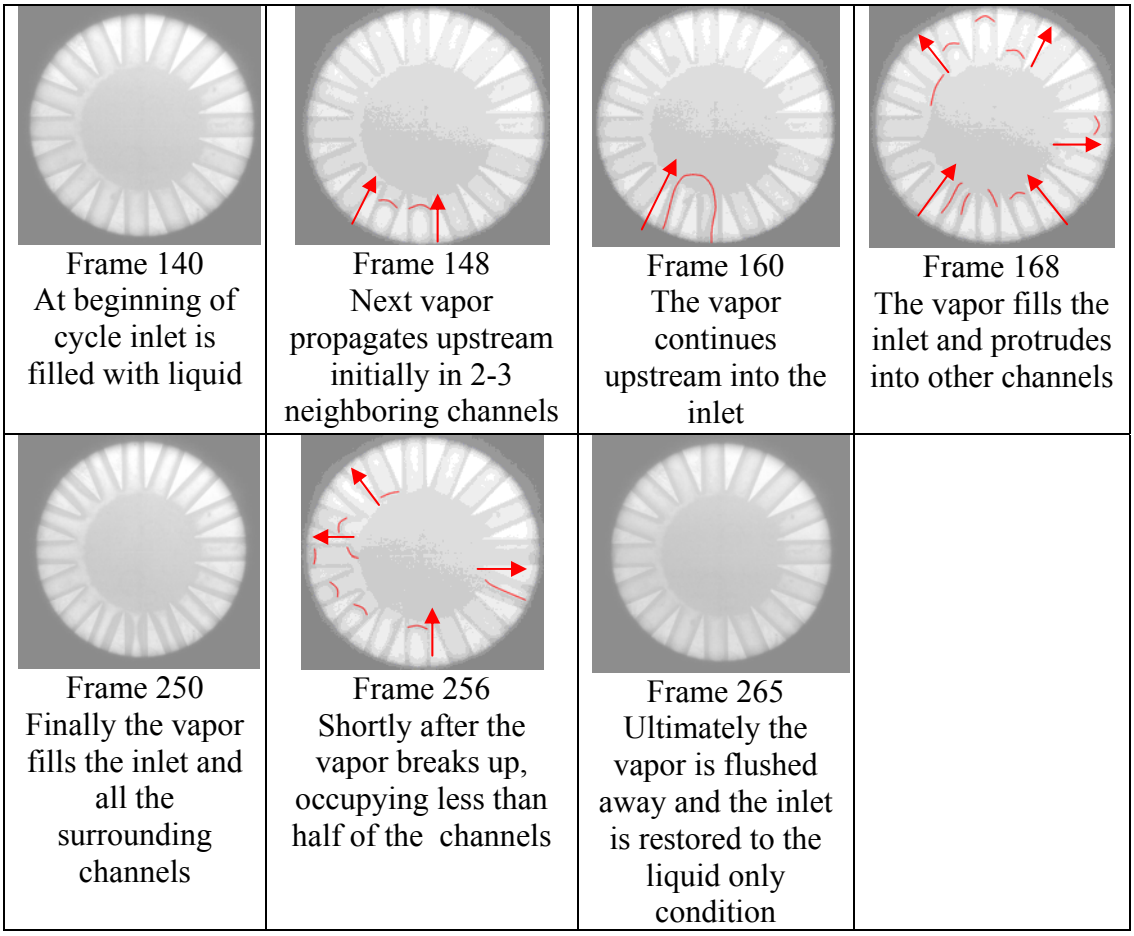

Figure 3.1: Typical behavior of a vapor-liquid cycle at the inlet plenum*. The flow conditions here are 10g/min flow rate, 1.76W/cm^2 input heat flux and 88°C inlet fluid temperature, no throttle. Images shown here were acquired at a rate of 70fps.

Frame 148 of fig.3.1 deserves consideration here. It is interesting that the upstream flow of vapor initially occurs in two-three neighboring channels. Lee & Pan [20] found one unstable channel may destabilize the channels surrounding it due to

complex interactions between the channels. Li et al.[17] described a similar phenomena stating that the interaction between channels on this scale is more complicated than conventional size channels due to the thinness of the wall separating channel from channel. When one channel become unstable (experiences the upstream flow of vapor) the local wall temperature could increase and due to the thinness of the channel walls cause a corresponding increase in wall temperature in neighboring channels thus inducing the upstream flow of vapor in neighboring channels. It should also be noted that the initial upstream propagation of vapor usually occurred in the same cluster of neighboring channels.

The behavior of the vapor in the test device is somewhat in between parallel channel instability and pressure drop oscillation instability, as observed in Qu & Mudawar [15]. In parallel channel instability the vapor fronts in the channels were found to oscillate up and down stream out of phase with one another and did not necessarily reach into the inlet plenum. In pressure drop oscillation the vapor fronts in each channel propagate upstream in unison toward the inlet plenum and after reaching the inlet are flushed downstream and the channels are refilled with single phase liquid. In the present experiment vapor from each channel flows upstream toward the inlet but it is not in unison. It may be that instability in a single channel propagates azimuthally from channel to channel eventually encompassing the entire fractal. This could explain why vapor first enters the inlet plenum from a few channels and as it begins to enter other channels from the inlet plenum it is met by the upstream flow of vapor in those channels often in the k0 branching level. The channel in which the instability initially occurs is the

---

[*] vapor-liquid interfaces demarcated to aid in visualization, and so throughout the document

first to have vapor reach the inlet plenum and as the instability spreads from channel to channel vapor flows upstream from those channels in a somewhat sequential fashion.

3.1.2 Effect of Increase in Heat Flux on Inlet Pressure

For both the throttled and non-throttled cases increasing heat flux while holding the flow rate constant increases the characteristic frequency of the inlet pressure oscillations while at the same time reducing the magnitude of the oscillations. It appears that the frequency of the oscillations doubles for a 50% increase in applied heat flux. This seems reasonable because one would expect more vapor to be generated with an increase in energy input to the fluid while holding the mass flux and inlet temperature constant. Based on the limited data it appears as the number of oscillations for a given time period decreases the energy content of those oscillations, e.g. the magnitude, increases. The trend is to have more energy per cycle for decreasing frequency. This is shown in the power spectral density plots of the pressure signals in fig.3.2 & fig.3.3. However, the apparent increase in magnitude of oscillations is within the specified uncertainty of the pressure measurement. Therefore, whether or not the magnitude is actually increasing is unknown. Also, it is observed that for both throttled and non-throttled cases the average inlet pressure increases with increase in heat flux.

In the present experiment the frequency of the oscillations of inlet pressure appear to be closer to that which corresponded to parallel channel instability as was observed by Qu & Mudawar [15]. Qu & Mudawar also found that increasing the heat flux while holding flow rate and inlet temperature constant increased the frequency of the oscillations of the pressure drop across the parallel channel device. However, this increase in heat flux was also accompanied by the addition of a throttle valve directly

upstream of the test section. So the results are complicated and a direct correlation between increase in heat flux and frequency and magnitude of oscillation is not possible from the results presented. It can be said that the trend for the addition of a throttle valve accompanied with an increase in heat flux is the oscillations of pressure increase and the magnitude of the oscillations decrease over two times. It should be noted that with the throttle valve employed the authors stated a different type of hydrodynamic instability was found. With the throttle valve parallel channel instability was observed whereas pressure drop oscillation was observed in the non-throttled case. These differences in types of instability observed further complicate the relation between heat flux and pressure oscillation.

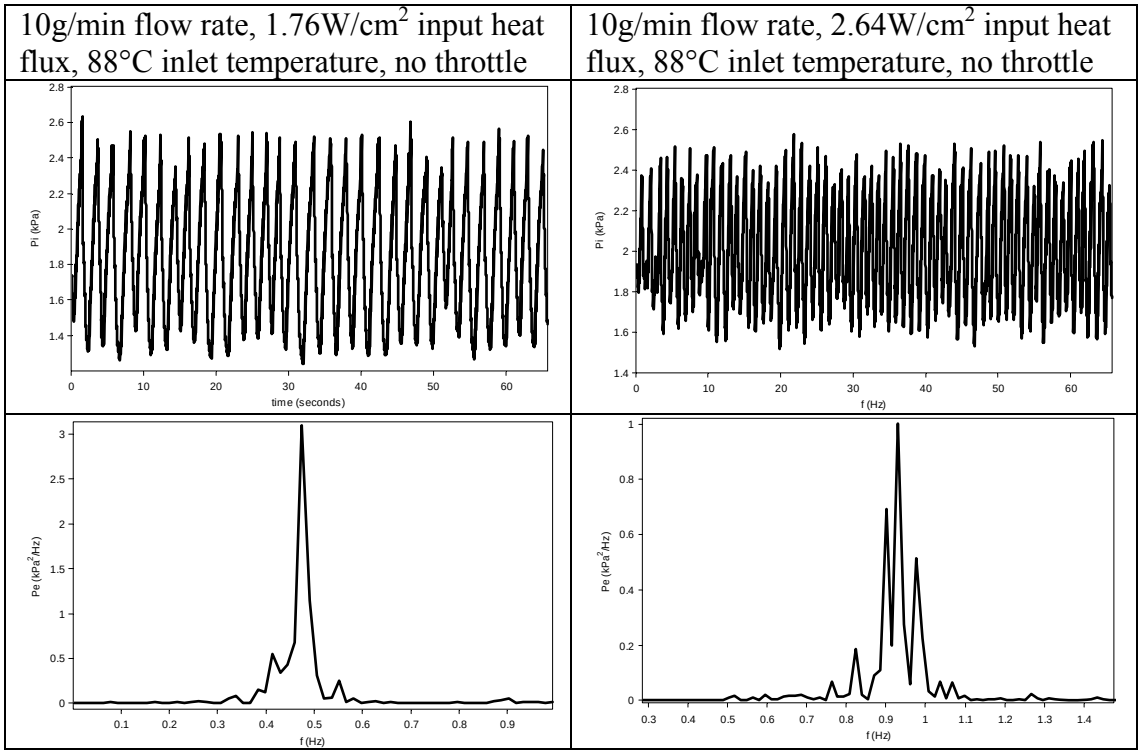

Figure 3.2: Inlet pressure signal and PSD plots from the test cases without throttling at the inlet.

The results in the current experiment appear to be contradictory with the literature not only in the way frequency of oscillations behaves with increase in heat flux but also the manner in which the amplitude of those oscillations varies with heat flux. Both Hetsroni et al. [16] and Muwanga et al. [21] found the trend of decrease in frequency and increase of amplitude of oscillations is found to occur with increase in heat flux. In the present experiment it was found that the magnitude of the oscillations decreased slightly with increasing heat flux. This phenomenon could be due to the difference in channel geometry of the test device used in the present study and the parallel types used in the studies in question.

However, Hetsroni et al. [16] also found that time between vapor slugs flowing upstream decreased with increasing boiling number which has been defined as $Bo=q''/G*h_{fg}$. This trend is in agreement with results observed in the present experiment. However, if the cyclical upstream flow of vapor is responsible for the oscillations of pressure or the result of a more complex system in which pressure oscillations and flow reversal are correlated, which from the literature seems to be the case, then it is difficult to understand how Hetsroni et al. [16] has both decreasing time between upstream flow of vapor and decreasing frequency of oscillations, for these should be mutually exclusive of each other. A decrease in the time between vapor slugs flowing upstream means more vapor moves upstream per time which should be accompanied by a corresponding increase in frequency of oscillation of inlet pressure. Further, an increase in vapor present in the channels should increase the pressure drop per time in those channels.

3.1.3 Effect of Throttle Valve on Inlet Pressure

Qu & Mudawar [15] employed a throttle valve to eliminate the large oscillations of pressure drop from the device. In their case it seems the upstream throttle valve is very effective to remedy the pressure drop oscillation problem as the heat flux was increased by three times the value used without the throttle valve while holding the mass flux and inlet temperature constant and still yielded only parallel channel instability in the test device.

With the introduction of a throttle valve creating a 150 kPa pressure drop directly upstream of the inlet of the test device there is an observed decrease in the frequency in the oscillations of the pressure signal along with a corresponding increase in the magnitude of the oscillations. Again from the limited data it appears that as the frequency of the oscillations decreases the energy content of the oscillations becomes greater. However, this increase in magnitude is also within the uncertainty limits of the measurement of inlet pressure. Use of the throttle valve effectively separates the test device from the upstream compressible volume as was mentioned in Muwanga et al. [21] and increases the system stiffness Qu & Mudawar [15]. Figure 14 shows a decrease in frequency of oscillations of inlet pressure by roughly a factor of two as compared with the signals measured with no throttle valve as shown in fig.3.2. Also, comparing the signals with and without the throttle valve a slight increase in the amplitude of the oscillations of pressure signal is observed. Use of a throttle valve ought to make it more difficult for the vapor to flow upstream and when it does more energy ought to be required to do so. Hence it seems reasonable to expect the vapor flow upstream over time, i.e., frequency of oscillations, to be reduced and for the energy of the upstream flow,

i.e., magnitude of oscillations, to be increased. Also, there is a decrease in the average inlet pressure with the addition of the throttle valve. Similar phenomena, such as shift in frequency and magnitude of pressure oscillations, were found to occur with increase in heat flux.

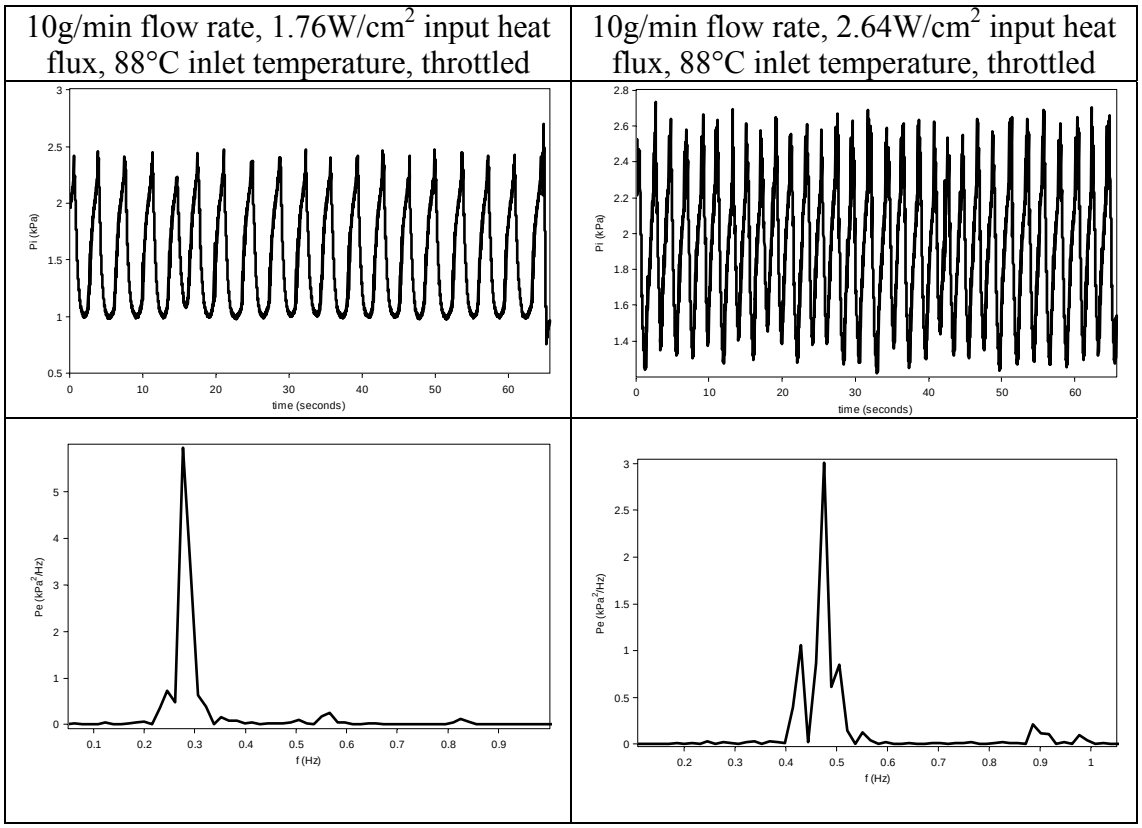

Figure 3.3: Inlet pressure signal and PSD plots from the test cases with throttling at the inlet.

3.1.4 Correlation of Vapor Activity at Inlet and Pressure Signal

It appears there is a strong correlation between activity of vapor near the inlet plenum and the inlet pressure signal. It was observed for all test cases that vapor would cyclically fill and be flushed out of the inlet plenum. To investigate the pressure phenomena in the present experiment, several long time scale movies (~14 seconds in

length @70fps) were taken at the inlet and outlet of the test device in order to understand how the behavior of vapor and inlet pressure were related. While the movies were taken the inlet pressure was measured concurrently with a sampling rate of 500Hz. However, the two measurements were not synchronized but merely acquired during the same experimental run. The selection of images in fig.3.1 depicts an average cycle of vapor filling and being flushed out of the inlet plenum. For all of the test conditions the behavior of the vapor remained the same but the cycle times of vapor activity changed substantially.

To understand the relationship between the recorded flow phenomena at the inlet and outlet plenums and the measured pressure signal, the vapor and liquid residence times were determined by watching each 70fps movie taken for a given set of flow conditions at the inlet and outlet plenums and recording the times which vapor entered and exited the plenum. The values presented for vapor and liquid residence times are average values of data taken from several movies. The average value was considered to be achieved when a running average of the values recorded leveled off by reaching a constant value.

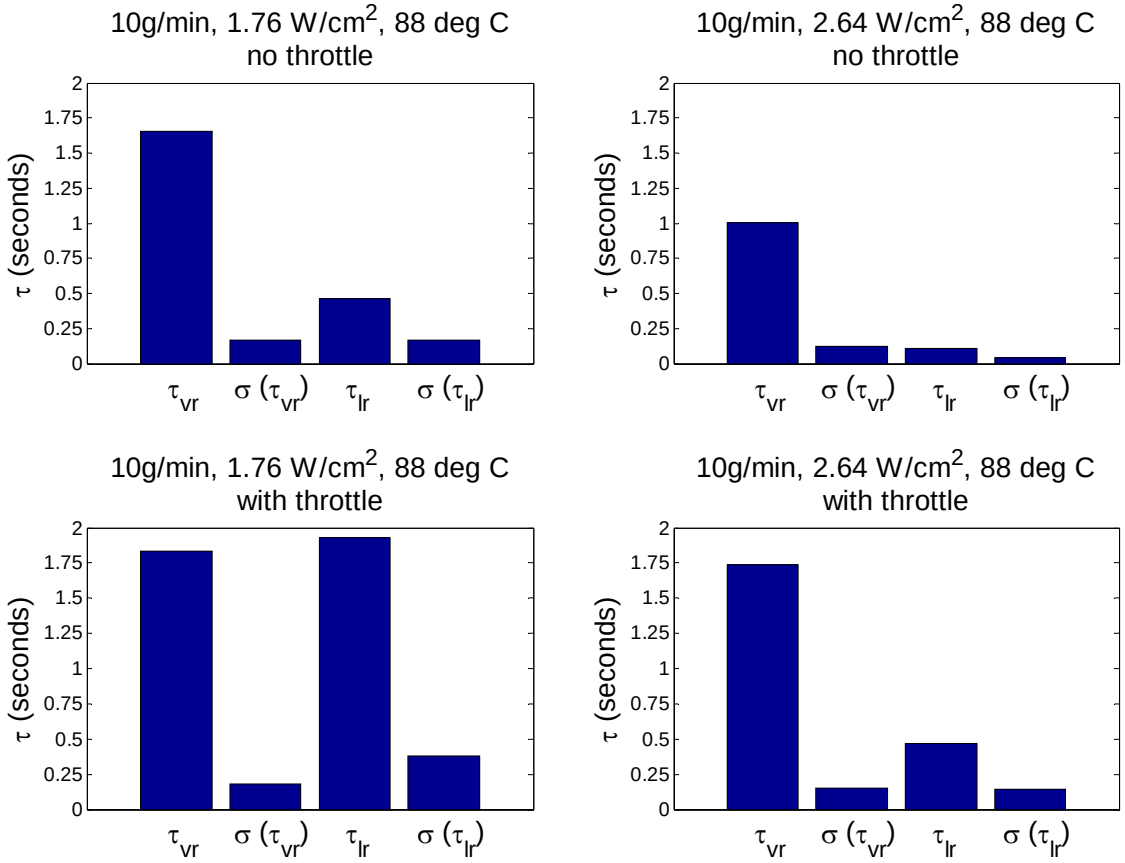

Figure 3.4: Average τ_{vr} & τ_{lr} at the inlet for each of the test cases. Calculated from the long time scale movies taken at the inlet

With the exception of the results of the 10g/min flow rate, 2.64W/cm^2 and 88°C inlet fluid temperature without throttling at the inlet, the vapor residence time doesn't change much. It appears the main contributor to the length of the period of one vapor-liquid cycle is the liquid residence time. In both the throttled and non-throttled cases the same trend of reduction in the length of liquid residence time is observed for increasing heat flux while holding mass flux and inlet temperature constant. In both cases a reduction by roughly a factor of four is observed. Also, when comparing the throttled and non-throttled cases, it appears the liquid residence time increases by roughly a factor of four when the throttle valve is employed.

So, with an increase in heat flux there is a decrease in the time interval between vapor residence times indicating more vapor is present for a given period of time than was found at the lower heat flux. Thus it is expected that cycles in the pressure signal would move closer together. Also, with the addition of the throttle valve there is an increase in the time between vapor residence times which should correspond to the cycles in the pressure signal moving farther apart.

Comparing the frequency of the oscillations of the pressure signals with the vapor activity at the inlet a strong correlation is observed as is shown in table 3.1. The time period of the vapor cycle added to the time period of the interval between cycles in each case almost exactly matches the frequency of the pressure oscillations measured.

Table 3.1: Comparison of dominant frequency measured from inlet pressure signal with those measured from observed vapor-liquid cycles at inlet.

Flow rate (g/min)	Input heat flux (W/cm^2)	Inlet fluid temperature (deg C)	Throttling at inlet	Period of vapor-liquid cycle at inlet (sec.)	Frequency of vapor-liquid cycle at inlet (Hz)	Frequency of dominant peak from PSD plots of inlet pressure signal (Hz)[ε]
10	1.76	88	No	2.12 +/- 0.32	0.47 +/- 0.07	0.47 +/- 0.01
10	2.64	88	No	1.11 +/- 0.16	0.90 +/- 0.13	0.93 +/- 0.01
10	1.76	88	Yes	3.76 +/- 0.56	0.27 +/- 0.04	0.28 +/- 0.01
10	2.64	88	Yes	2.21 +/- 0.29	0.45 +/- 0.06	0.47 +/- 0.01

[ε] note: the uncertainty reported is the resolution error which is 1/(length of measured pressure signal)

With the strong correlation observed between long time scale movies at the inlet and the measured pressure signal it is clear the observations made of the trends that characterize the behavior of the inlet pressure signal with increasing heat flux in the present experiment are indeed correct. However, the results presented for the current experiment are contrary to what has been documented in the literature.

In both Hetsroni et al. [16] and Muwanga et al. [21], a trend of decrease in frequency with increase in heat flux is observed. It could be that due to the difference in test conditions the present experiment sees different trends in behavior of pressure drop with increase in heat flux. Table 3.2 shows the heat fluxes, mass fluxes and inlet temperatures employed in the studies being compared in this section. The ranges for which data is presented are very different and it was noted by Muwanga et al. [21] the frequency of the oscillations is not only dependent upon heat flux but also upon mass flux and inlet temperature. The current experiment was conducted at very low heat fluxes and mass flux. So with such a broad range of flow conditions and limited data sets it may be hasty to conclude there is a direct disagreement between the trends shown for behavior of frequency with varying heat flux. Also, the difference in geometry between the current experiment and those compared here will definitely have a substantial influence.
The studies found in the literature are of parallel channel networks and the present experiment is investigating fractal-like bifurcating channel flow network which increases in cross-sectional flow area as the branching level increases. However, Muwanga et al. [21] found that the same trend of decreasing frequency with increasing heat flux occurred for both the standard parallel channel configuration and the cross-linked channel geometry unique to that experiment. The cross-linked geometry in this experiment in

some ways captured a feature of the fractal-like geometry in the present experiment. Once an upstream-flowing vapor slug reaches one of the cross-link channels it can flow laterally into any one of the other parallel channels in the network rather than continuing upstream. This was thought to minimize pressure oscillations by reducing the amount of vapor flowing upstream and reaching the inlet plenum. The fractal-like geometry in the present experiment also does this though in a much different way. At each bifurcation an upstream flowing vapor slug has the potential to loop around the bifurcation and then travel down the alternate daughter channel. Even with this consideration the geometries are seemingly too different to draw a conclusion.

Table 3.2: Heat flux, mass flux, and inlet temperature of experiments compared in this section.

	note	q" (kW/m^2)	G ($kg/(m^2s)$)	q"/G (m^2/s^2)	Ti (°C)
Present Study	10g/min, 1.76W/cm^2	17.60	53.10	333.33	88
	10g/min, 2.64W/cm^2	26.40	53.10	499.06	88
Hetsroni et al. [16]		200.00	93.30	2143.62	ambient
		220.00	93.30	2357.98	ambient
Muwanga et al. [21]		79.00	140.00	564.29	70
Qu&Mudawar [15]	Pressure drop instability	879.00	400.10	2196.95	30
	Parallel channel instability	2400.00	400.10	5998.50	30

3.2 Prediction of Stable & Unstable Flow Conditions

Chang & Pan [19] determined experimentally that if the magnitude of oscillations of pressure drop across the test device was greater than or equal to 6 kPa the flow was

unstable and the characteristics of the vapor phenomena changed drastically. In their plot of this phenomenon they plotted the magnitude of the pressure oscillations against the input heat flux for five different flow rates. On the plot a horizontal dotted line was plotted at 6 kPa to denote the transition boundary from stable to unstable flow.

In order to extrapolate their findings to encompass the findings of the present experiment along with the findings of other published investigators the axes of their plot were non-dimensionalized. The heat flux was non-dimensionalized with the boiling number and was calculated using the heat of vaporization of saturated liquid water at atmospheric pressure. The magnitude of the oscillations of pressure drop, defined as the difference between the maximum instant pressure drop, DP_{max}, and the minimum instant pressure drop, DP_{min}, was non-dimensionalized by multiplying it with the density of saturated liquid water at atmospheric pressure and dividing by the mass flux squared and was named DP_N.

$$DP_N = \frac{\rho_{l,sat}\left(DP_{\max} - DP_{\min}\right)}{G^2} \qquad 3.2$$

Which value of density to use as the multiplier is not known but whatever the value is it seems it would scale all the terms accordingly and not change their relative position to each other when plotted. The density of saturated water at atmospheric pressure seemed reasonable to start with since the fluid at the inlet of the fractal is not much above atmospheric. All of the data along the horizontal 6 kPa threshold line from Chang & Pan [19] was non-dimensionalized according to the above paradigm and plotted as the stability threshold on a log-log plot below in fig.3.5.

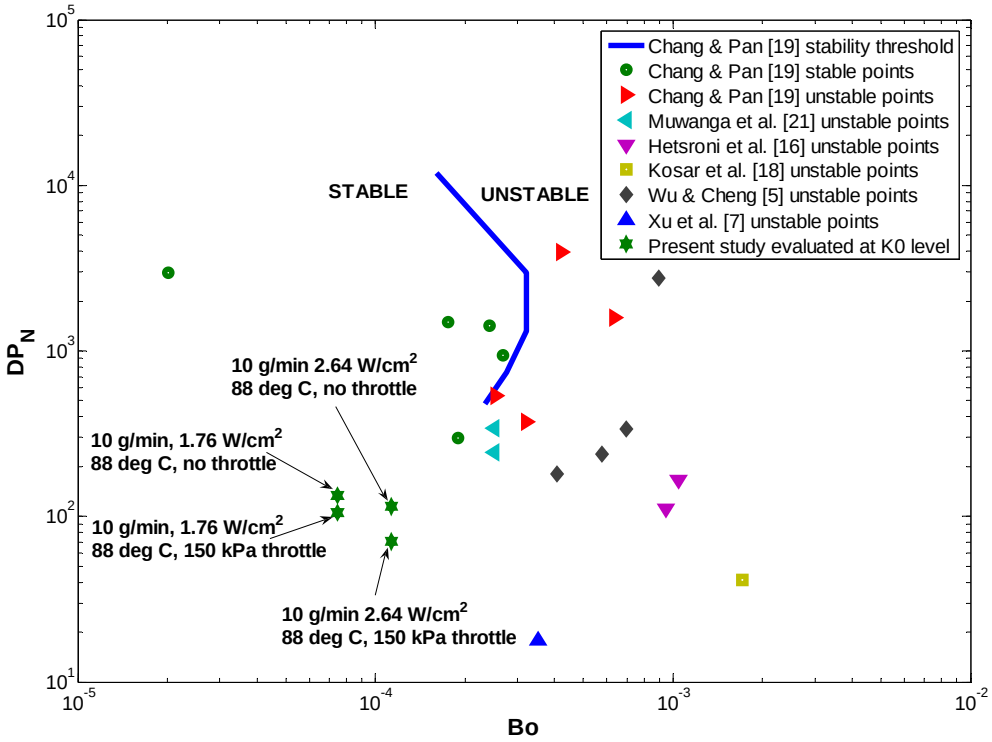

Figure 3.5: Non-dimensionalized stability plot adapted from Chang & Pan [19]. The data points in the present study were plotted using the cross-sectional area of the channels from the K0 level.

In fig.3.5 points to the left of the stability threshold are stable while points to the right are unstable. If the data from the present experiment is omitted it seems that all of the unstable data plotted falls on the unstable side of the threshold and all of the stable data falls on the stable side of the threshold. It appears the data of the present experiment could either be stable or unstable due to the limited data available from Chang & Pan [19]. However, the cross-sectional flow area of the test device has a large impact on where the data points are located on the plot due to the fact that in the present study the cross-sectional flow area increases along the streamwise direction as branching level increases. In fig.3.5 the data points of the present experiment is evaluated using the cross-sectional

area of the K0 branching level. The effect of increasing cross-sectional flow area is investigated below in fig.3.6.

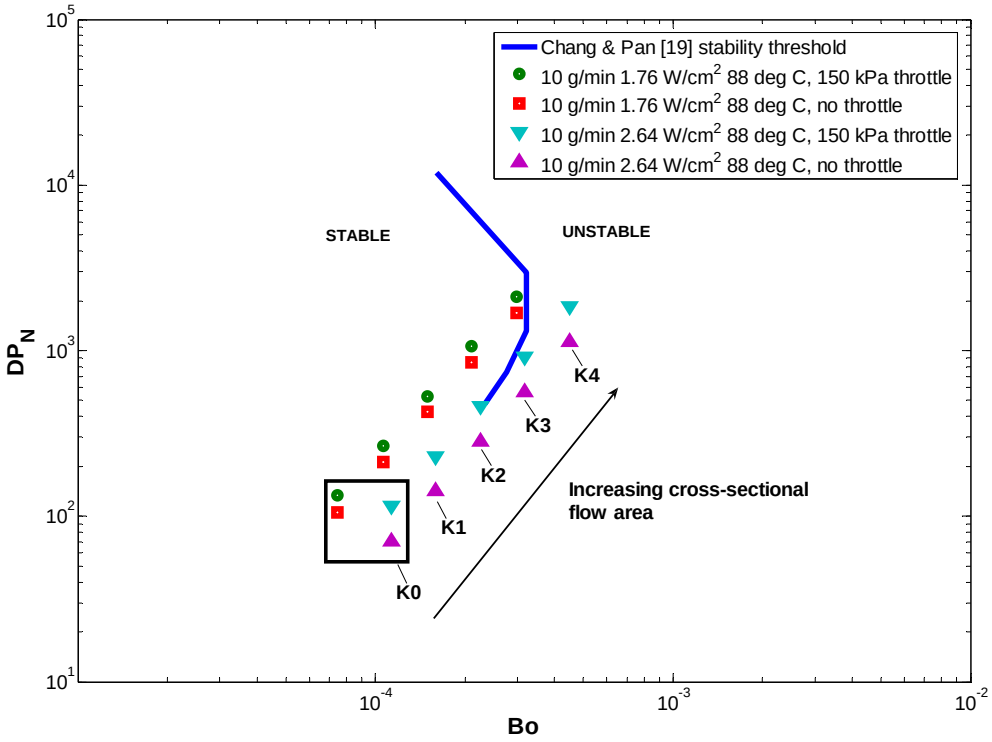

Figure 3.6: Non-dimensionalized stability threshold adapted from Chang & Pan [19] showing the effect of increasing cross-sectional flow area in the present experiment.

From fig.3.6 it appears the data points may fall on both sides of the stability threshold depending on which cross-sectional flow area is used. However, the flow for all of the cases was found to be unstable. It is possible variations of flow conditions could also change where the data falls in regard to the stability threshold.

In fig.3.7 the effect of variation of flow conditions is investigated utilizing the cross-sectional area of the K4 branching level channels. In one case the flow rate is reduced 10% to 9g/min and the input heat flux is increased 10% to 1.94W/cm^2 and in the other the mass flow is increased 10% to 11g/min and the input heat flux is decreased by 10% 1.58W/cm^2. These perturbations are meant to approximate worst case scenarios

producing either much more vapor in the former case and much less vapor in the latter case than the target case of 10g/min, 1.76W/cm^2.

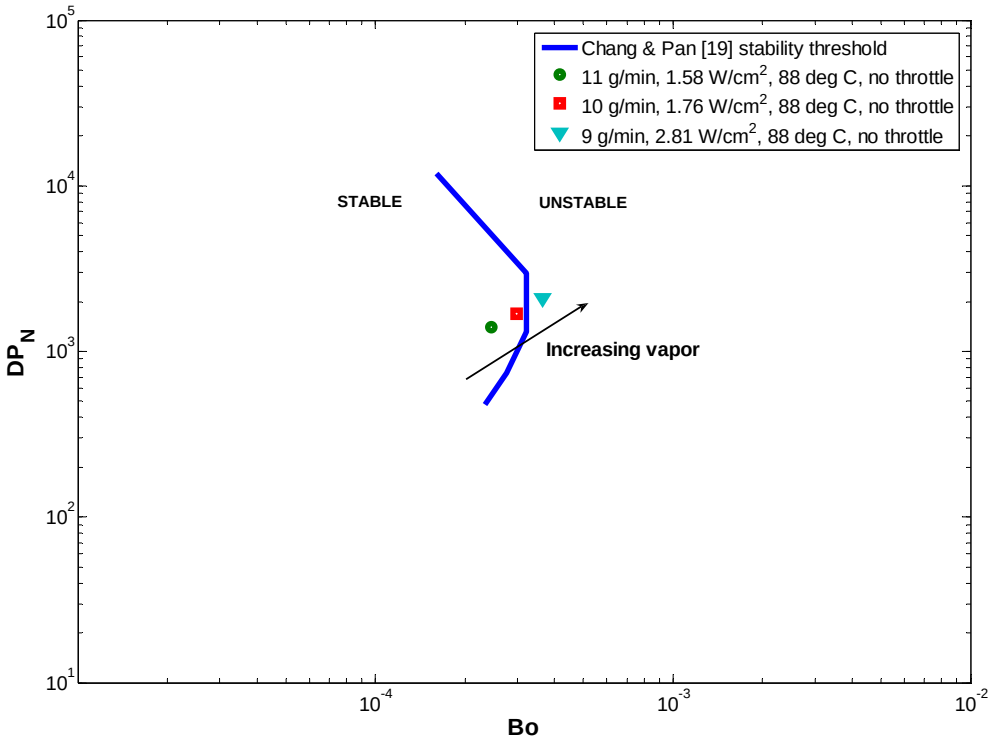

Figure 3.7: Effect of variation of flow conditions on the location of a data point relative to the stability threshold.

So it appears using the stability criteria of Chang & Pan [19] that the flow conditions of the present experiment can be either stable or unstable depending on what cross-sectional area is used (location in the test device) and small perturbations of the flow conditions due to the relative proximity of the data points to the actual stability line. However, it must also be considered that the geometry of the test device in the present experiment is radically different from the parallel channel configurations used in the other investigations compared here.

3.3 Flow Phenomena & Observations

3.3.1 K0 Branching Level

3.3.1.1 K0 without Throttling

At the K0 branching level for the test case without throttling at the inlet it was typical to observe intermittent annular flow. In this case at the K0 level annular flow would be present for a period of time until it was flushed away by single phase liquid from the inlet.

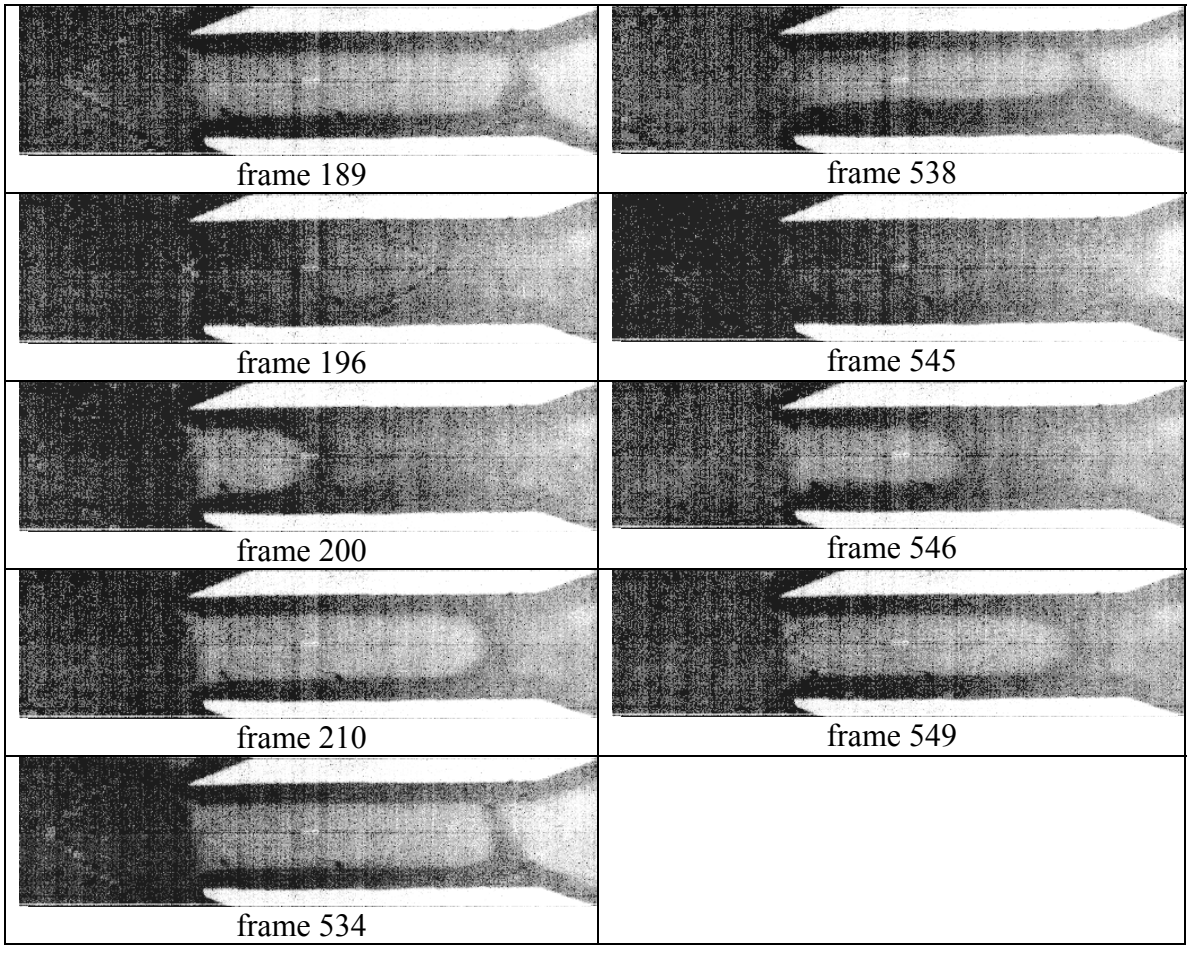

Figure 3.8: A sequence of frames from a single movie demonstrating the typical intermittent annular flow phenomena at the K0 branching level without throttling at the inlet. The flow conditions are 10g/min flow rate, 1.76 W/cm^2 input heat flux and 88°C inlet fluid temperature. The frames shown here were acquired at a rate of 1000fps.

There appears to be no regular periodic intervals of time over which annular flow is present. The time period over which annular flow or single phase liquid flow were present were observed to vary in a random manner.

In frame 189 of fig.3.8, the K0 level is filled with vapor. Note there appears to be some kind article on the top surface of the channel. This should not be confused with a vapor-liquid interface. In frame 196 the flow has transitioned back to single-phase liquid. Then in frames 200-534 fresh vapor enters and eventually fills the entire channel. It appears the liquid film on the right-most channel wall increases in thickness in frame 538 and is one of the initial frames in a process that takes the flow in the channel back to single phase liquid in frame 545. Then in frame 546 and 549 the process of fresh vapor entering from the inlet starts again.

It was common to see vapor enter the K0 level from the inlet plenum and flow downstream as is shown in frames 200, 210 and 534 in fig.3.8. However, vapor did flow upstream into the K0 level. Usually when this occurred the upstream flowing vapor would coalesce with vapor from the inlet plenum in the K0 level. Upstream flowing vapor was never seen to reach all the way into the inlet plenum through travelling upstream in this test case but was met halfway in the K0 level by vapor already present in the inlet.

It was found that of the movies used for analysis 17% had vapor in less then 25% of the total number of frames in the movie. Beyond this 31% had vapor in less than 50% of the frames and 4% had no vapor at all. This accounts for 71% of all the movies used in the analysis at the K0 level for the case without throttling at the inlet. In the cases

reported where movies had low amounts of vapor, if the movie had a large continuous number of frames with single phase liquid either at the beginning or end of the movie then the number of frames of the movie which contained vapor were counted and the movie was placed in one of the three categories; either less than 50% vapor, less than 25% vapor, or no vapor.

3.3.1.2 K0 with Throttling

Once the throttling valve was employed at the inlet the amount of vapor present over time in the K0 channel increased. Of the movies used in the analysis it was found that 6% had vapor in less than 25% of the frames. Other than that 6% all of the other movies did not have a significant portion of continuous frames which contained single phase liquid following the paradigm expounded in the section describing the flow phenomena at K0 with no throttling at the inlet.

Aside from the shear increase in amount of vapor present in the movies over the non-throttled case, the main differences in flow phenomena with the flow throttled at the inlet were the occurrence of wavy annular flow and what is here called "rapid detach-reattach" of vapor interfaces. Frames 221, 232, 243 and 247 of fig.3.9 highlight the occurrence of the typical appearance of the wavy annular flow observed in the movies used for analysis here. It seems the flow of fresh liquid from the inlet plenum forces its way down the K0 level when the vapor region in the K0 level is connected with the vapor in the inlet plenum. Frames 212, 216, 217, 221 and 232 of fig.3.9 demonstrate the occurrence of what is here called "rapid detach-reattach" of vapor interfaces. The appearance of the rapid detach-reattach of vapor interfaces shown here is typical of this phenomenon and usually has an interval of about 15 milliseconds between the time when

the vapor interfaces initially separate and the time at which they merge together. This process happens repeatedly in a given movie as is shown in frames 247 and 256.
In the movies used for analysis here 52% were found to display the occurrence of rapid detach-reattach of vapor interfaces and 40% were found to display only the intermittent wavy annular flow.

Typically the reattachment would occur at the beginning of the K0 level immediately following the inlet plenum and would occur between vapor already present in the inlet plenum and vapor flowing upstream through the K0 level. Frames 63, 69, and 124 of fig.3.9 are used to demonstrate the presence of vapor in the inlet plenum before the upstream flow of vapor enters the K0 level. Initially in frame 63 the K0 channel is filled with single phase liquid into which a small portion of vapor protrudes in frame 69 and then retreats in frame 124. Typically the vapor in the inlet plenum would protrude a small distance into the K0 level and then retreat back into the inlet. This process would repeat until the upstream flow of vapor entered the K0 level.

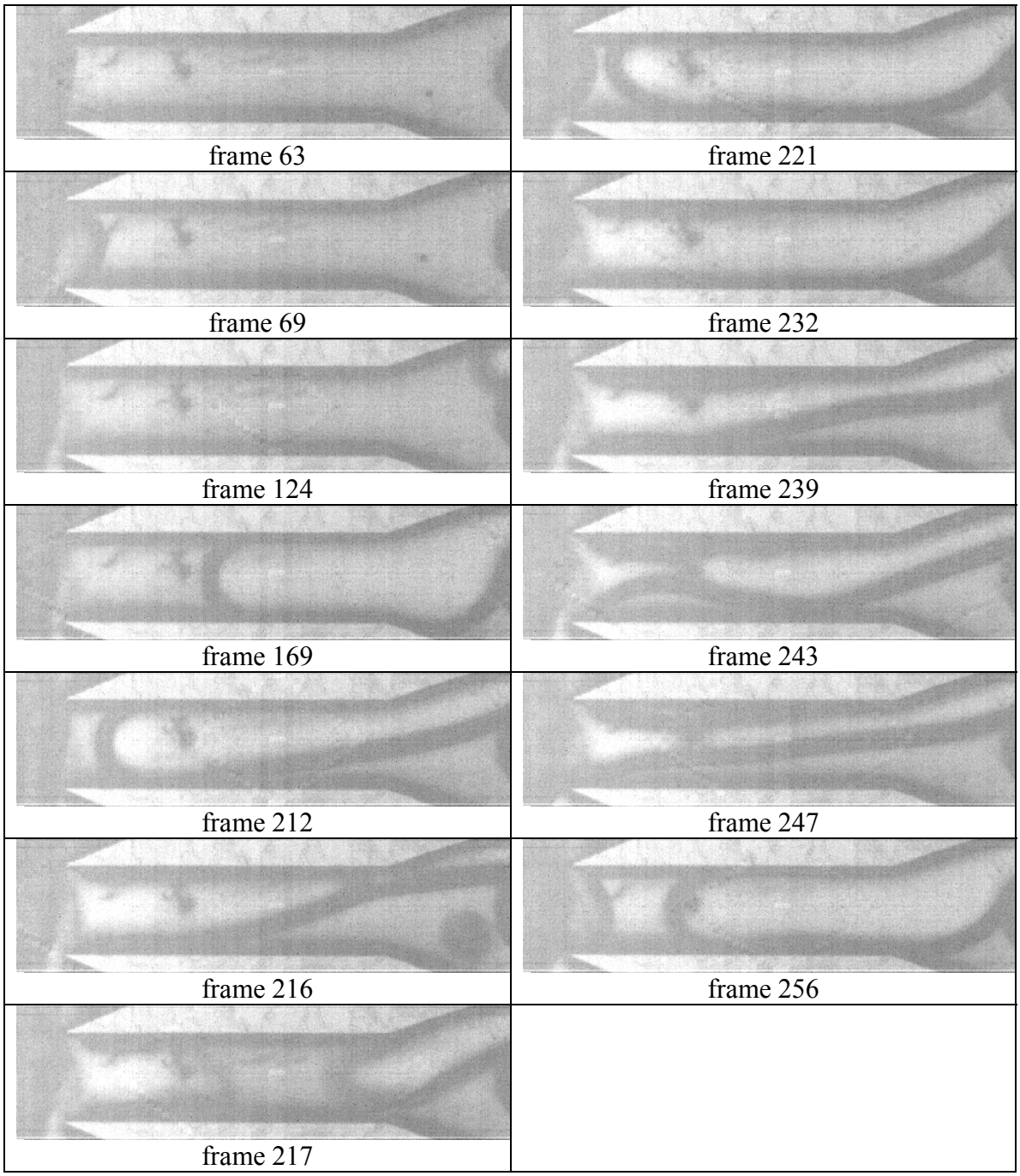

Figure 3.9: A sequence of images demonstrating the typical intermittent wavy annular flow phenomena at the K0 branching level with throttling at the inlet. The flow conditions are 10g/min flow rate, 1.76 W/cm^2 input heat flux and 88°C inlet fluid temperature.

3.3.2 K1 Branching Level

Figure 3.10 documents what happens directly downstream of the K0 level. In this level it was found both the throttled and non-throttled cases displayed nearly identical flow behavior; meaning the differences observed were insignificant and providing separate figures to illustrate the flow phenomena is unnecessary. The sequence of images shown in fig.3.10 begins with single phase vapor and ends with single phase liquid in the channels. Again it appears the transition between single phase liquid and single phase vapor flow is chaotic, meaning it doesn't appear to conform to a regular periodic cycle. In frame 480 of fig.3.10 the channels are filled with single phase vapor. Then by frame 558 the liquid film has increased in thickness along the left-most channel wall and small drops of liquid have appeared on the top surface of the channel over the bifurcation region. The liquid film grows and transitions to an entire liquid layer in frames 610-617 before the vapor present is flushed out replaced with fresh vapor from the K0 level in frames 620-699. Then the vapor is eventually flushed away and replaced with single phase liquid in frames 753-763.

The wavy annular flow shown in frames 610, 612 and 617 of fig.3.10 is typical of the vapor activity that occurs when the vapor in the K0 level is connected with the vapor in the inlet plenum and fresh liquid from the inlet flows down the K0 level. This wavy annular flow was found to occur in 80% of the movies used for analysis at this location while 11% of the movies displayed annular flow only, 7% displayed vapor in less than 25% of the frames and 2% displayed single phase liquid only.

In the case without throttling at the inlet the numbers were slightly different. Here 86% of the movies displayed the intermittent wavy annular flow show in fig.3.10 while 3% displayed annular flow only, 11% displayed vapor in less than 25% of the frames and 2% displayed single phase liquid only.

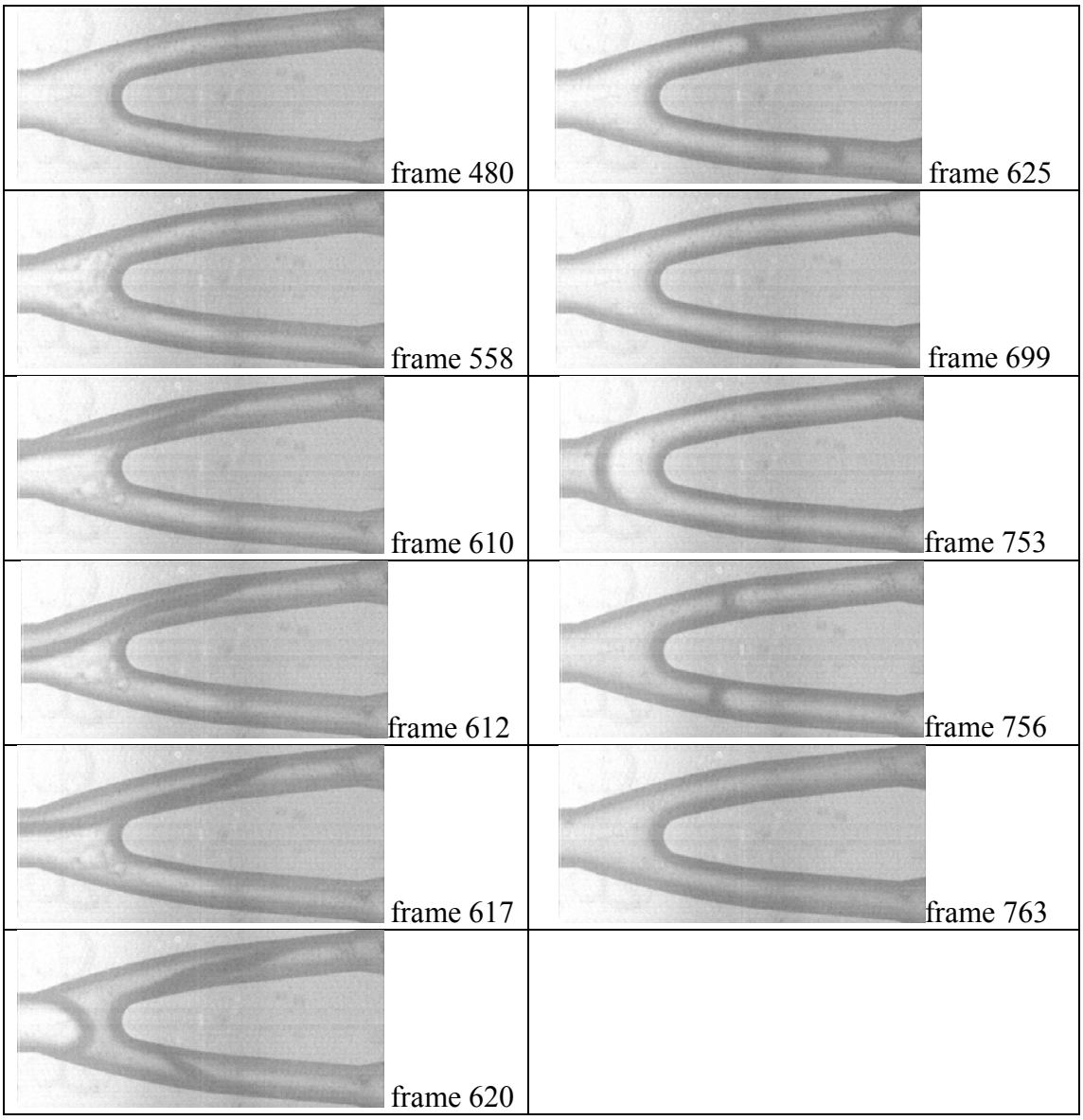

Figure 3.10: A sequence of images that demonstrate the typical wavy annular and slug flow phenomena at the K1 branching level. This is typical of both the case with throttling at the inlet and the case without throttling at the inlet. The flow conditions are 10g/min flow rate, 1.76 W/cm^2 input heat flux and 88°C inlet fluid temperature.

3.3.3 K2 Branching Level

3.3.3.1 K2 without Throttling

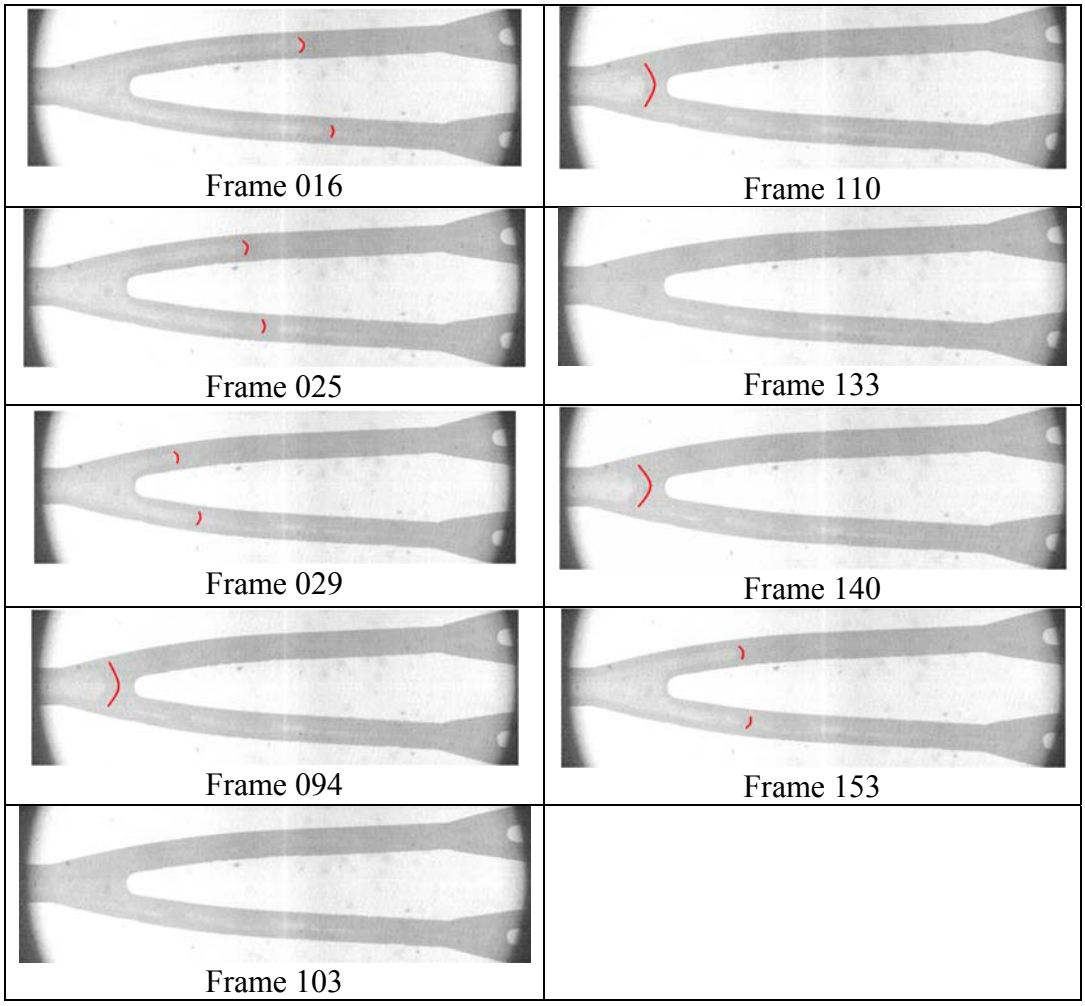

Figure 3.11: A sequence of images demonstrating the typical oscillation of the vapor-liquid interface at the bifurcation at the K2 branching level without throttling at the inlet*. The flow conditions are 10g/min flow rate, 1.76 W/cm^2 input heat flux and 88°C inlet fluid temperature. The frames presented here were acquired at 1000fps.

At the K2 branching level for the case without throttling at the inlet it was found the two most frequently occurring flow phenomena were oscillation of the vapor-liquid interface of a vapor slug at the bifurcation and what is here called intermittent annular flow with a progressive liquid film, which is discussed more in the K3 branching level

part of this section. Figure 3.11 depicts the typical appearance of the process of the oscillation of the vapor-liquid interface of a vapor slug at the bifurcation. In frames 016-103 the vapor-liquid interfaces are shown to recede upstream and eventually leave the field of view. Then the interface reappears in frame 110 only to recede back upstream again in frame 133 but it returns and moves further downstream in frames 140-153.

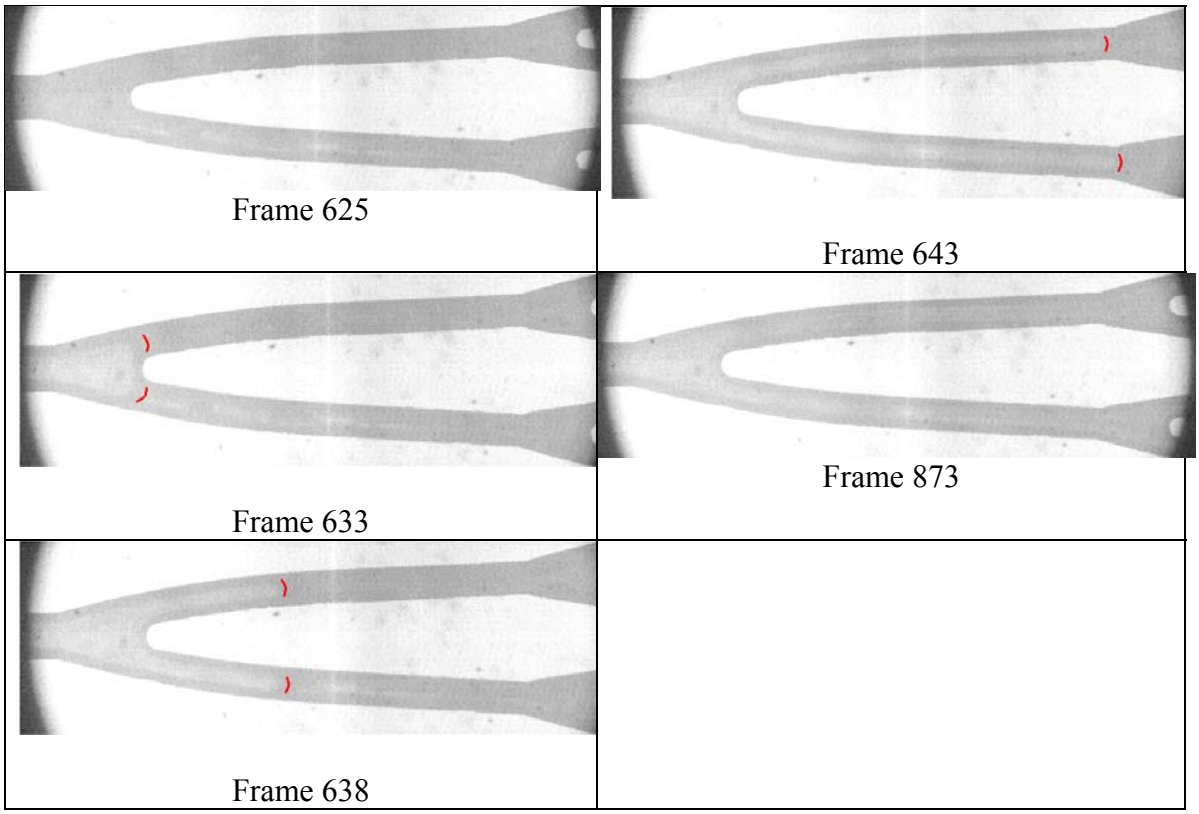

Figure 3.12: a sequence of images demonstrating the oscillation of the vapor-liquid interface transitioning to annular flow at the K2 branching level without throttling at the inlet*. The flow conditions are 10g/min flow rate, 1.76 W/cm^2 input heat flux and 88°C inlet fluid temperature. The frames shown here were acquired at a rate of 1000fps.

However, for most of the occurrences of the oscillation of the vapor-liquid interface at the bifurcation the movies either began with or ended with the flow transitioning to annular flow. Figure 3.12 presents an example of a movie in which the flow transitioned to the annular regime from the phenomenon of oscillation of the vapor-

liquid interface. In frame 625 the channels are filled with single phase liquid. It was found that in 36% of the movies used in the analysis for this case at this location showed initially the phenomenon of oscillation of the vapor-liquid interface which then transitioned to the annular flow, whereas 35% showed the reverse of this; that is annular flow transitioning to the phenomenon of oscillation of the vapor-liquid interface. These combine account for 71% of the movies used. The remaining movies fell in two categories: only oscillation of the vapor-liquid interface at the bifurcation and intermittent annular flow with a progressive liquid film. Also, 13% of the movies used were found to show the only oscillation of the vapor-liquid interface at the bifurcation and the remaining 16% were found to show intermittent annular flow with a progressive liquid film.

3.3.3.2 K2 with Throttling

Figure 3.13 shows the oscillation of a vapor front of a slug that is trying to flow upstream at the K2 branching level for the case with throttling at the inlet. The vapor-liquid interface makes its way upstream but seems to be met with resistance not seen in the non-throttled case at the same location. The oscillation of the vapor-liquid interface of a vapor slug at the bifurcation shown in fig.3.11 was not observed in any of the movies used for the analysis at this location for the case with throttling at the inlet. The oscillation of the interface appears to have no regular periodic behavior. The times between maximum upstream advances in each oscillation vary. For example, the time interval between frame 849 and 865 is 16 milliseconds which would yield an oscillation frequency of about 63Hz. The time interval between frames 865 and 873 is 8 milliseconds which correspond to an oscillation frequency of about 125Hz. However, the

frequencies of the oscillations appear to be no less than two but as high as three orders of magnitude greater than the oscillation of measured inlet pressure.

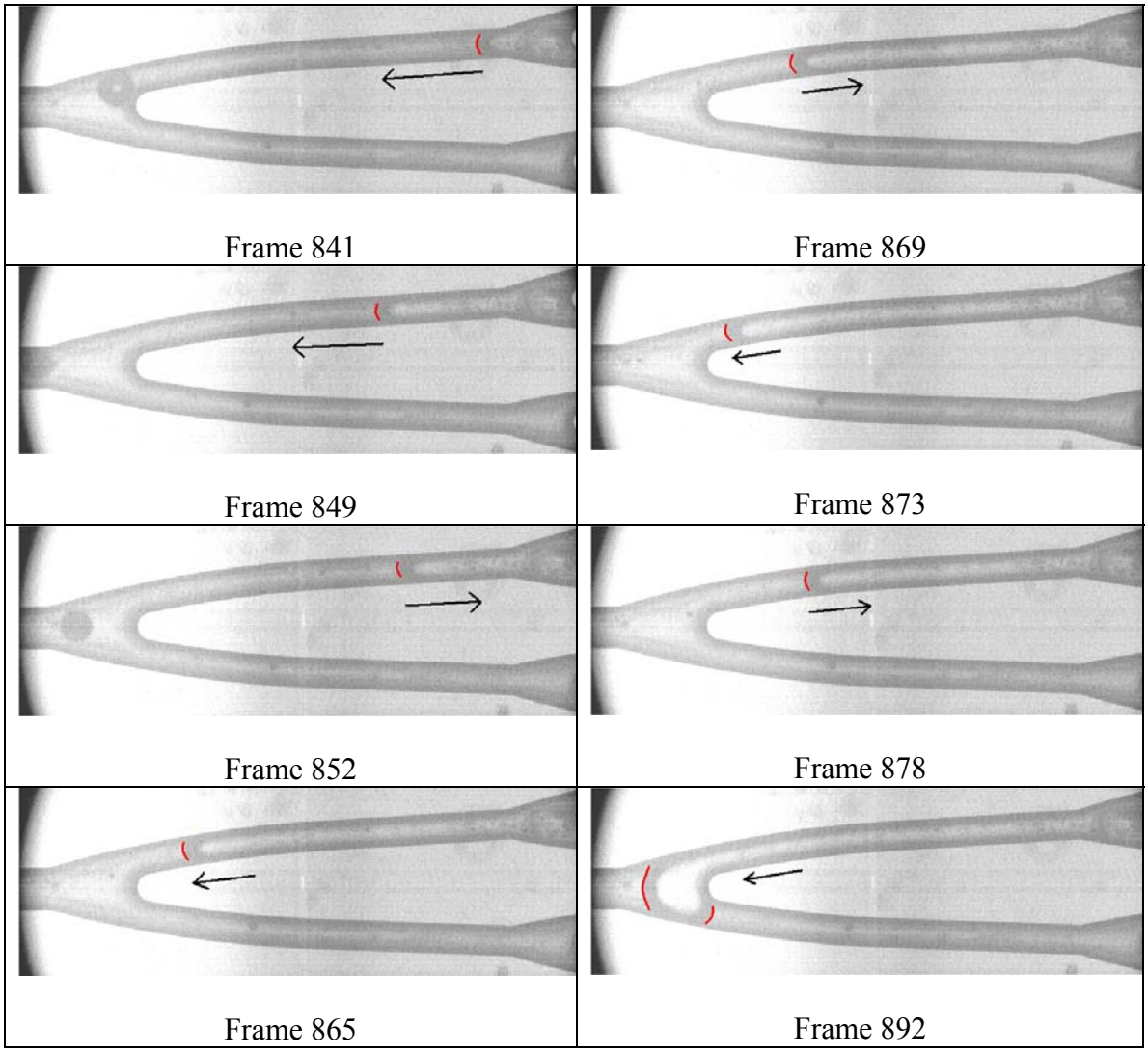

Figure 3.13: A sequence of images demonstrating the occurrence of the oscillation of the vapor-liquid interface of a vapor slug travelling upstream at the K2 branching level for the case with throttling at the inlet*. The flow conditions are 10g/min flow rate, 1.76 W/cm^2 input heat flux and 88°C inlet fluid temperature. The frames shown here were acquired at a rate of 1000fps.

The phenomena of oscillation of the vapor-liquid interface of upstream flowing vapor shown in fig.3.13 occurred in 44% of the movies used for analysis at this location for the case with throttling at the inlet. The rest of the movies used for analysis here were

comprised of intermittent annular flow with a progressive liquid film (42%), combination of intermittent annular flow with a progressive liquid film and oscillation of the vapor-liquid interface of upstream flowing vapor (5%), a constant layer of liquid film over an annular vapor core (4%) and single phase liquid only (5%).

3.3.4 K3 Branching Level

Figure 3.14 depicts a typical occurrence of intermittent annular flow with a progressive liquid film. The sequence begins with single phase liquid which fills the channels in frame 456. In frames 458 and 461, what appears to be a vapor stream enters and travels down the K3 branching level but in frame 464, 466 and 471 it appears a second vapor stream enters and travels down the K3 branching level immediately following the first vapor stream. However, the second vapor stream appears brighter than the first and this increase in image intensity is interpreted to mean there is a liquid film surrounding or at least covering the top of the vapor core which enters and travels down the K3 level in frames 458 and 461. Thus in the entry and flow of the vapor stream shown in frames 464, 466, and 471 it would seem no liquid film is present or at least a much thinner film is present and the entire or at least more of the channel cross-section is occupied by an annular region. Then in frames 471, 474, 478, 485 and 492 the gradual decrease in intensity of the image over the channels is apparent; especially at the bifurcation region. This gradual decrease in intensity is interpreted as the growth of a liquid film either around the annular core in the channel or at least as a growth of a liquid film on the top surface of the channel. In this case the transition from single phase vapor back to single phase liquid flow occurs gradually without a clearly defined vapor tail

exiting the channel. This phenomenon occurred in 66% of the movies used in the analysis for this location.

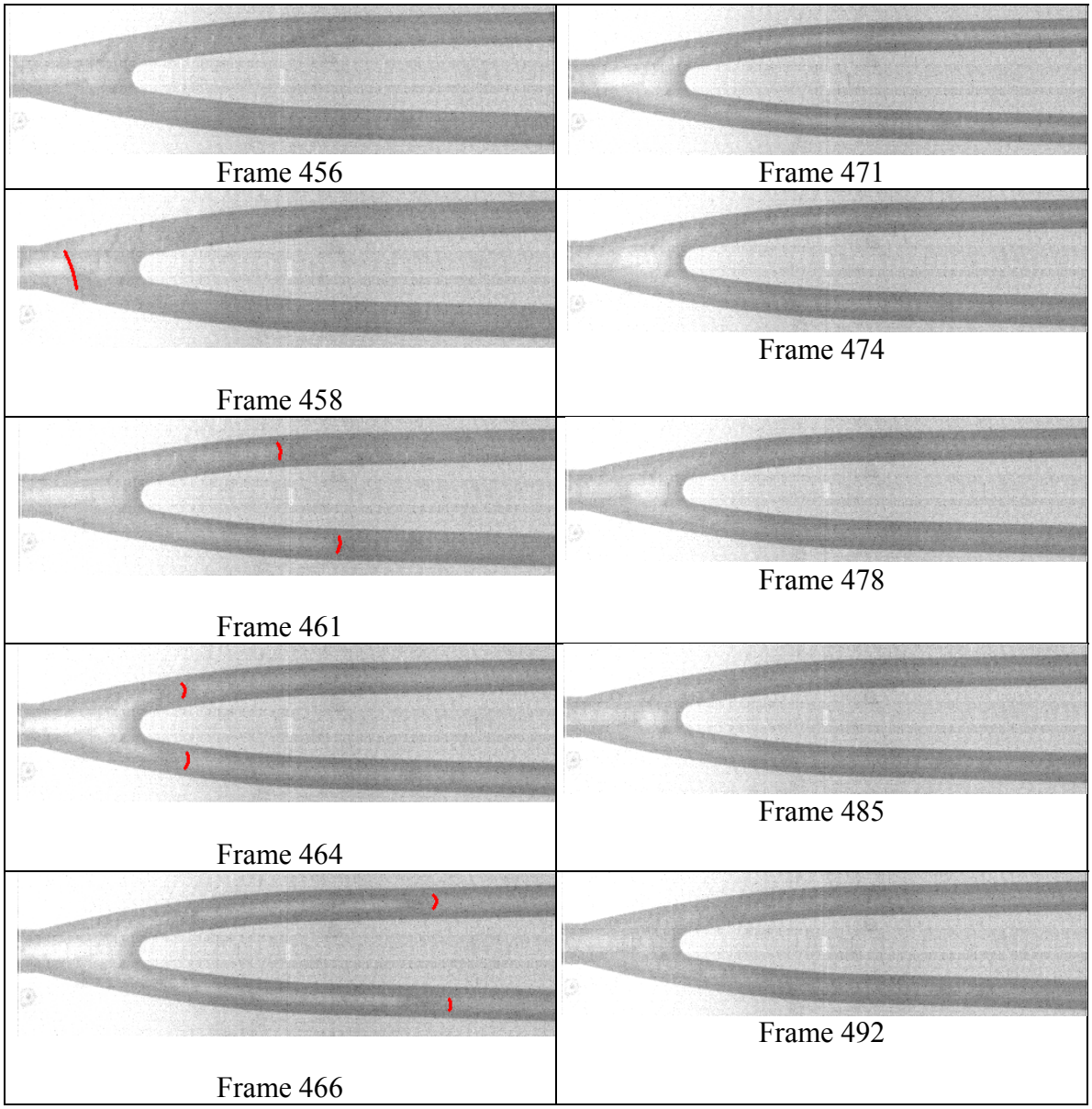

Figure 3.14: A sequence of images demonstrating the typical progression from liquid to annular flow to a liquid film forming over the annular region and gradually transitioning back to single phase liquid at the K3 branching level*. This phenomenon occurred in both the throttled and non-throttled test case. The flow conditions are 10g/min flow rate, 1.76 W/cm^2 input heat flux and 88°C inlet fluid temperature.

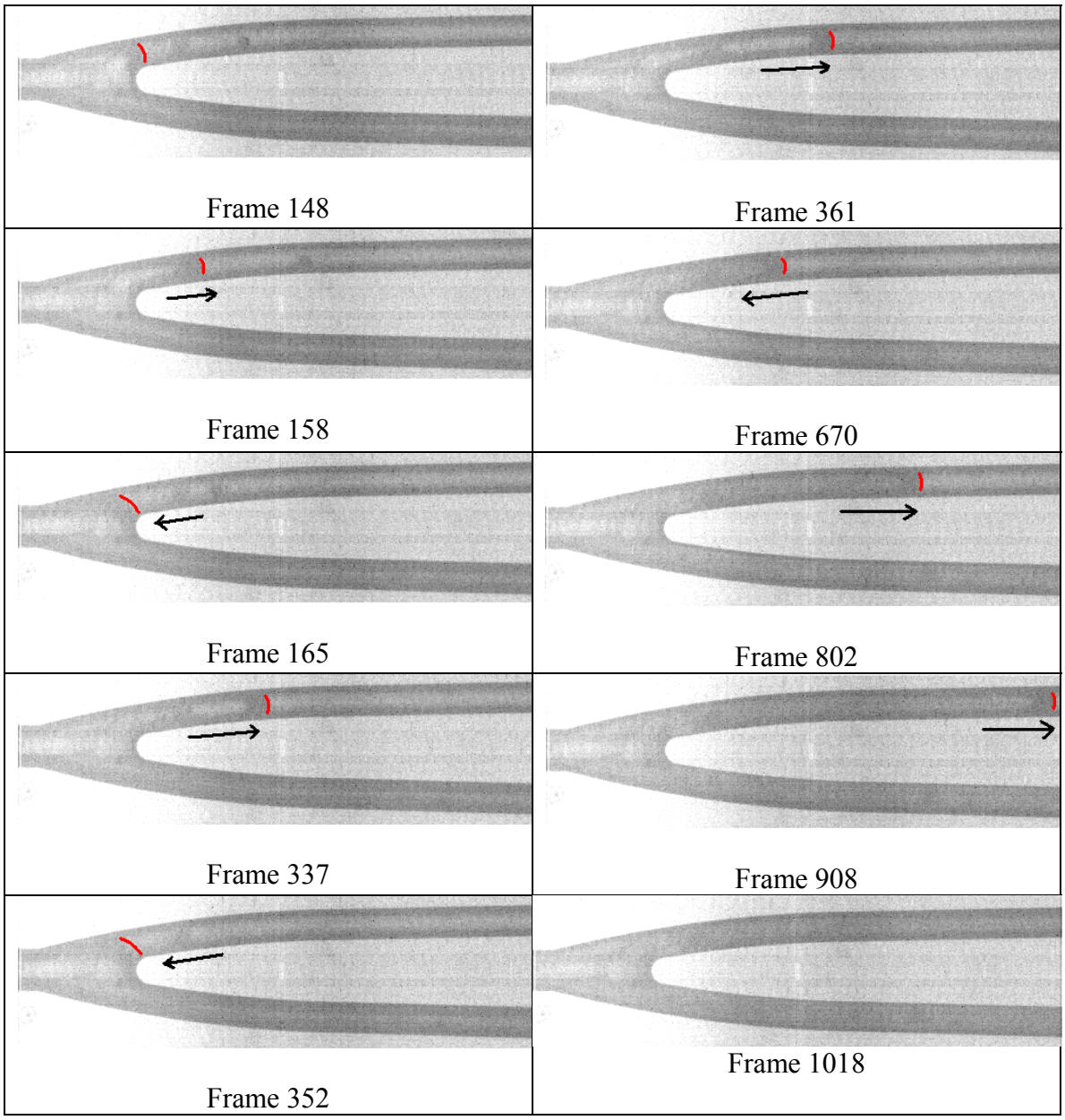

Figure 3.15: A sequence of images demonstrating the oscillation of a vapor-liquid interface into one of a pair of daughter channels at the K3 level for the case with throttling at the inlet*. The flow conditions are 10g/min flow rate, 1.76 W/cm^2 input heat flux and 88°C inlet fluid temperature. The images shown here were acquired at a rate of 1000fps.

The other frequently occurring phenomena came in two varieties. The first was an oscillation of the vapor-liquid interface at the bifurcation of a vapor slug attempting to flow downstream. This phenomenon was typified by one channel in a daughter channel

pair containing annular flow while the vapor-liquid interface oscillated in and out of the adjacent daughter channel as is shown in fig.3.15. In fig3.15 the right-most channel is filled with vapor. In each of these instances the layer of liquid film appears over the top of the vapor regions in the channels. Thus the intensity of the area where vapor is present appears almost as dark as the image where there is single phase liquid. It should be noted the selection of images shown in fig.3.15 were chosen to most clearly demonstrate the motion of the interface near the bifurcation. In actuality the interface experienced much smaller amplitude oscillations on the order of 100Hz. The oscillations shown in fig.3.15 occur from frame 148 to frame 670 and then the vapor interface slowly proceeds downstream and eventually both channels are filled with vapor as shown in frames 670 through 1018. This phenomenon occurred in 14% of the movies used for analysis at this location.

The next type of frequent occurrence was movies with single phase liquid only throughout the extent of the movie. This phenomenon occurred in 18% of the movies used in the analysis at this location. The remaining 2% was made up of combinations of the phenomena discussed above.

In the case without throttling it was found the occurrence of intermittent annular flow with a progressive liquid film accounted for 59% of all the movies used for the analysis of that case while 7% showed oscillation of the vapor interface down one of a pair of daughter channels from a bifurcation, 13 % showed a vapor core with a constant liquid film over the top of it, 1% showed single phase liquid only and 10% showed vapor expanding upstream in one channel only toward the bifurcation.

3.3.5 K4 Branching Level

3.3.5.1 K4 without Throttling

At the K4 branching level for the case without throttling at the inlet three main types of flow phenomena occurred. The first is called "stable entry/exit" of vapor. This is a relative term in the sense that it is stable compared to oscillation of vapor or rapid change in size of bubbles or slugs. Figure 3.16 shows the typical behavior of a stable entrance and propagation of vapor. The stable exit of vapor is similar in nature to what is shown in fig.3.16 but instead of vapor entering the channels it is shown to be exiting. This stable entry/exit of vapor phenomenon occurred in 16% of the movies used in the analysis at this location.

The second main type of flow phenomena is oscillation of a vapor liquid-interface at the bifurcation. This phenomenon is shown in fig.3.17. In frames 686-715 vapor enters the K4 channels and propagates downstream. However, it stops and in frames 720-744 it reverses direction and flows upstream to the bifurcation. Then in frames 780-822 a similar process is repeated. Again there seems to be no regular time interval over which the oscillation occurs. The period of oscillation is typically somewhere between 30 and 80 milliseconds corresponding to frequencies ranging from about 13 to 33Hz which is also two orders of magnitude greater than the oscillations of inlet pressure. The oscillation of a vapor interface at the bifurcation occurs in 34% of the movies used in the analysis here.

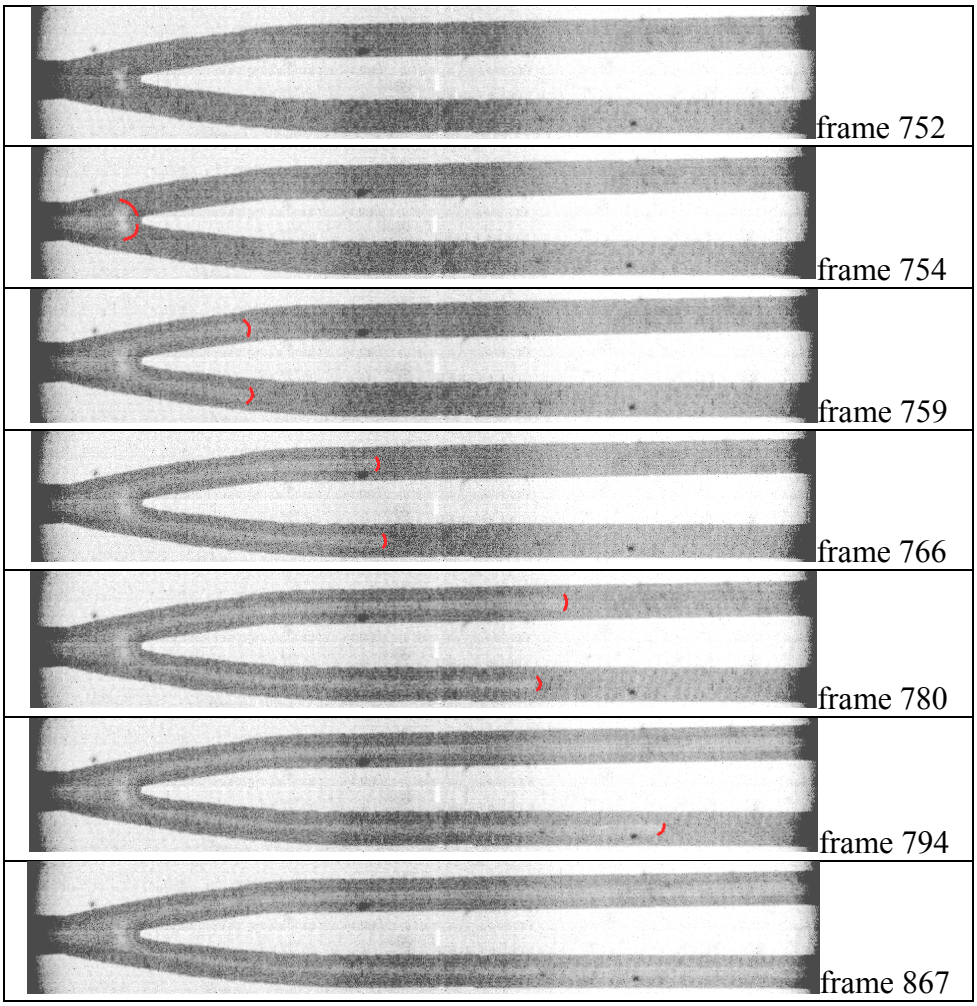

Figure 3.16: Sequence of images documenting the typical behavior of a stable expansion of vapor slugs down the upstream K4 location with no throttling at the inlet*. The flow conditions are 10g/min flow rate, 1.76 W/cm^2 input heat flux and 88°C inlet fluid temperature.

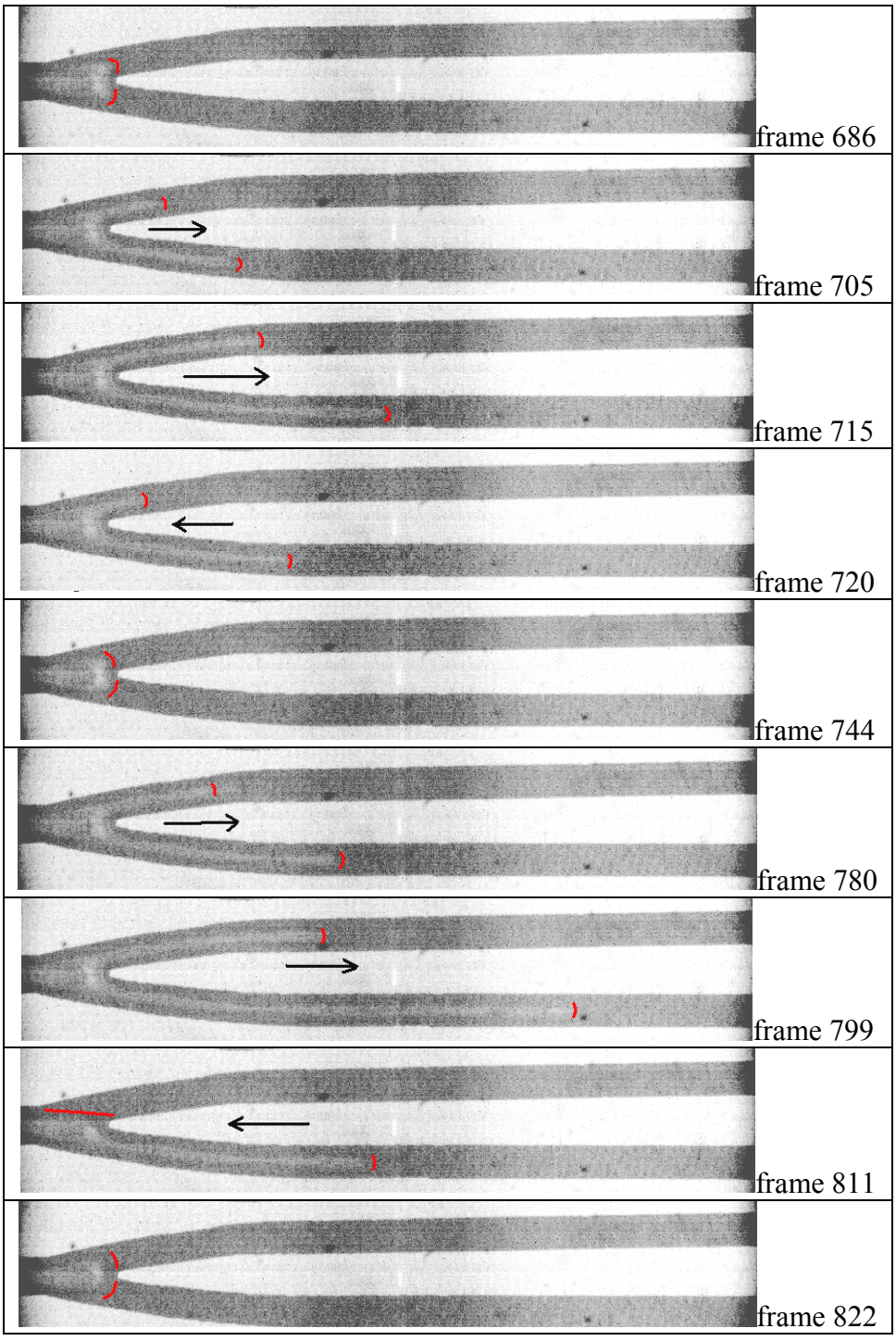

Figure 3.17: A sequence of images demonstrating the typical appearance of oscillations of the position of a vapor-liquid interface at the upstream K4 level for the case without throttling*. The flow conditions are 10g/min flow rate, 1.76 W/cm^2 input heat flux and 88°C inlet fluid temperature.

The third main type of flow phenomena is single phase liquid only. These single phase liquid flows occur in 41% of the movies at this location. The remaining 9% of the movies show phenomena only occurring once. Some examples are a group of small bubbles passing through the channel or a bubble trapped at the bifurcation. In these movies the presence of vapor is usually less than 50 out of 1000 frames.

If the correlation between oscillation of the measured inlet pressure signal and the periodic filling and clearing of the inlet plenum with vapor is extrapolated to these phenomena it would mean that the local pressure drop near the vapor slug could be oscillating at a rate two orders of magnitude greater than the measured global pressure drop.

3.3.5.2 K4 With Throttling: Oscillation of Vapor Slugs

Oscillation of the vapor-liquid interface occurred at the K4 level in the case with throttling at the inlet as it did without throttling at the inlet as shown in fig.3.18. The oscillation of the vapor-liquid interface occurred in 25% of the movies used for analysis at this location. The same lack of a regular time interval over which the oscillation occurs is present in the throttled case as in the non-throttled case. However, the range of time intervals over which the oscillation occurs is the same as the non-throttled case; somewhere between 30 and 80 milliseconds corresponding to frequencies of 13- 33Hz. The main difference between oscillations of the vapor interfaces in the throttled case versus the non-throttled case has to do with the position of the interfaces. In the non-throttled case it the vapor interface actually retreats back into the bifurcation completely exiting the channels, whereas in the throttled case the interface never appears to do this. In general the vapor phenomena at the K4 level for the case with throttling at the inlet

were more violent and varied than for the case without throttling at the inlet, involving more explosive behavior.

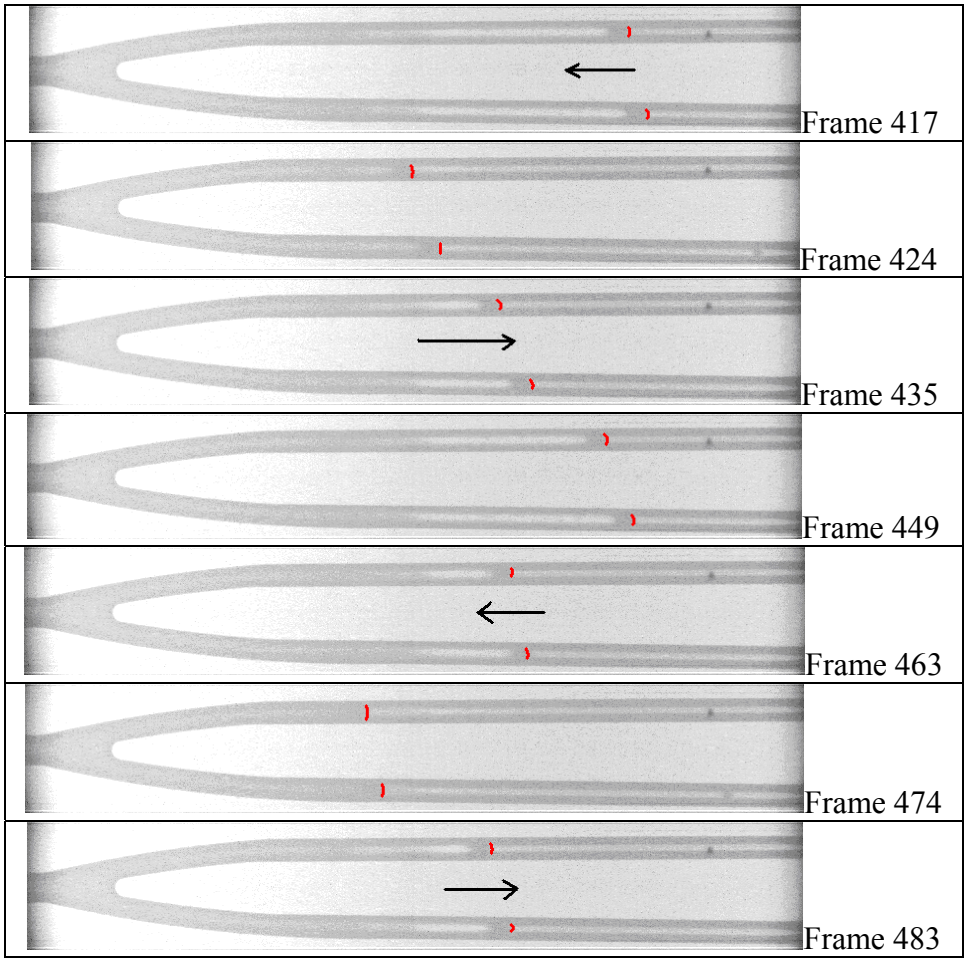

Figure 3.18: Typical oscillation of oscillation of the location of the downstream vapor slug in the K4 upstream location with throttling at the inlet*. The flow conditions are 10g/min flow rate, 1.76 W/cm^2 input heat flux and 88°C inlet fluid temperature. The frames shown here were acquired at a rate of 1000fps.

3.3.5.3 K4 with Throttling: Apparent Bubble Collapse

It seems the main difference in phenomena seen at the K4 level when the flow was throttled at the inlet was the occurrence of what is here called the cycle of apparent expansion and collapse as is shown in fig.3.19. In frame 676 of fig.3.19 vapor is shown to protrude into the K4 channels where it has remained since the beginning of the movie.

In frames 688-691 the apparent collapse process occurs. Then in frame 694 new vapor enters the k4 channels and appears to be following close after the other vapor, which was already in the process of collapsing, and eventually replaces it in frames 696-704. In this phenomenon typically it appears as if vapor slugs on the order of 1 millimeter in length are collapsed down to small spherical or close to spherical bubbles with a diameter close to the width of the channel. Immediately following and even during this apparent collapse another vapor slug appears to be expanding to take its place. In some movies this cycle would happen several times in some it would happen only once. In those movies in which several of these apparent collapses occurred the time between the collapse of one vapor slug and the expansion of another varied widely from on the order of 100 milliseconds down to a collapse of one slug and the expansion of another occurring at the same time, as is shown in fig.3.19. This phenomenon occurred in 52% of the movies used for analysis at this location.

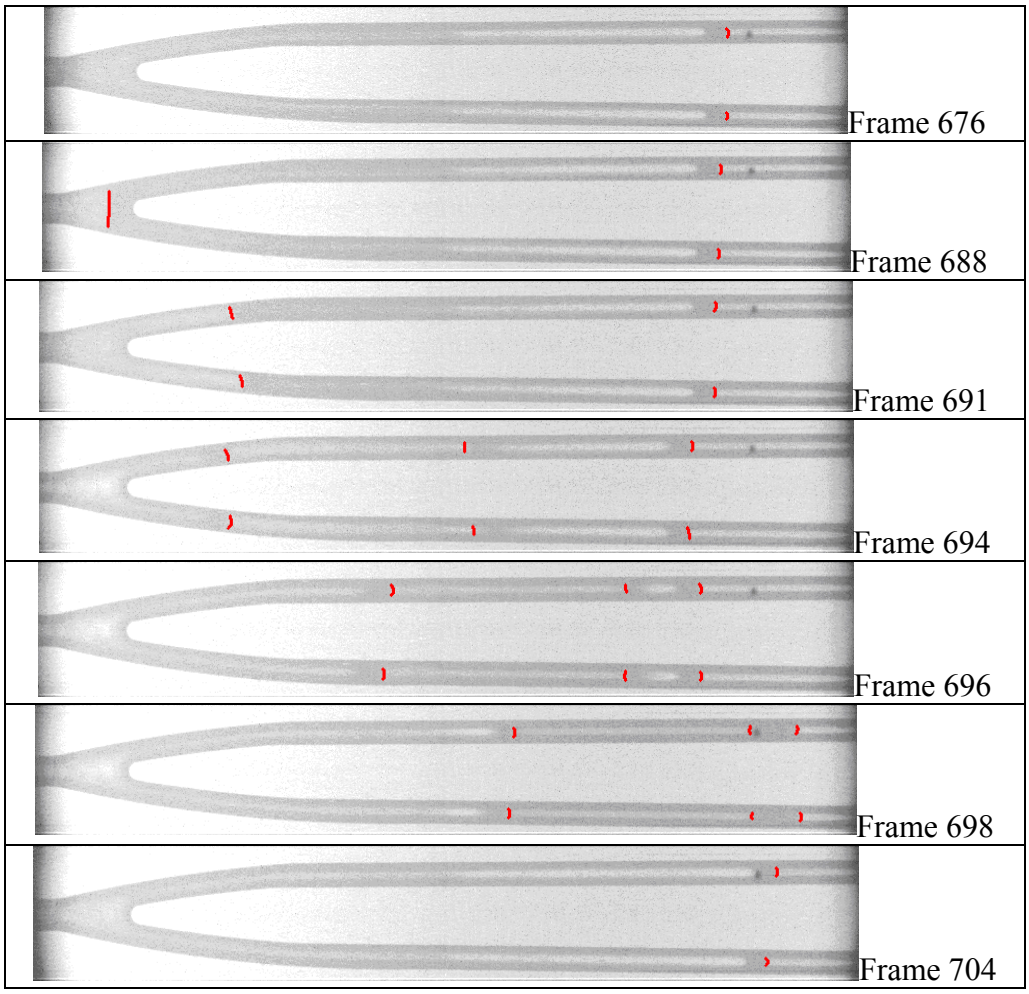

Figure 3.19: Typical cycle of apparent expansion and collapse at the upstream K4 location with throttling at the inlet*. The flow conditions are 10g/min flow rate, 1.76 W/cm^2 input heat flux and 88°C inlet fluid temperature. The frames shown here were acquired at a rate of 1000fps.

Figure 3.20 is an example of an apparent collapse in which only one vapor slug collapse occurs. It appears that when a collapse occurs if another vapor slug is entering the channel while the collapsing bubble is still present, as is the case in fig.3.19, the time over which the slug collapses decreases. For example the slug collapse in fig.3.19 occurs over roughly 0.01 seconds whereas the collapse in fig.3.20 occurs over roughly 0.18 seconds. The movie from which the frames in fig.3.19 are taken featured two other vapor slug collapses. In the latter cases the collapsing slugs were not immediately followed by

new vapor slugs expanding to take their place and as a result the time intervals over which the collapses occurred were 0.028 and 0.026 seconds.

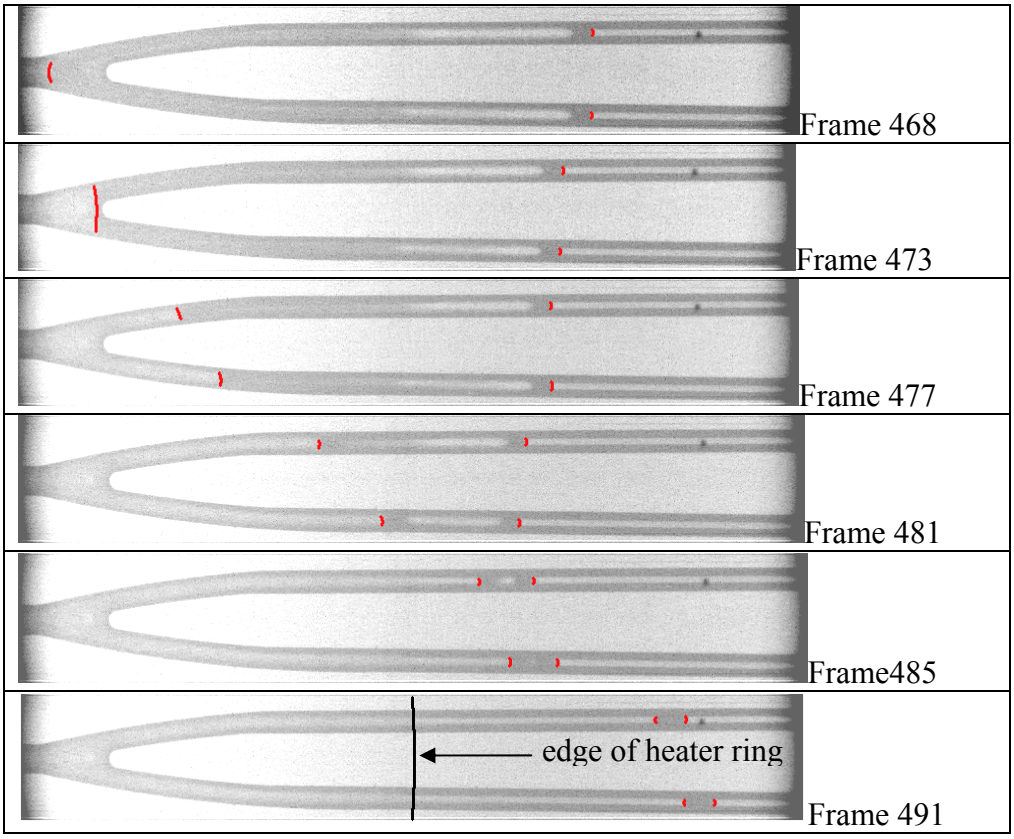

Figure 3.20: A sequence of images taken at the upstream K4 documenting an apparent bubble collapse*. This movie had only a single collapse which was then followed by single phase liquid flow for the rest of the movie. The flow conditions are 10g/min flow rate, 1.76 W/cm^2 input heat flux and 88°C inlet fluid temperature. The frames shown here were acquired at a rate of 1000fps.

Also, of interest is the fact that the collapse of a bubble at the K4 branching level always seems to happen in the same place and in the same manner. During the apparent collapse the downstream interfaces of the vapor slug extending into the K4 branching level will move upstream a little as if a high pressure region on both sides of the slug were compressing it together. This appears to happen until the slug reaches a length of about three times the channel width at which point the downstream interface of the slug will

begin to move downstream. The upstream interface will move downstream toward the downstream interface of the slug and when it reaches the bifurcation the interface will divide in two equal parts. The collapse process follows the same symmetric distribution around the bifurcation as do vapor slugs expanding around the bifurcation; meaning the vapor slugs typically divide into two mostly equal portions as they pass through the bifurcation. Thus the initial slug is divided into two slugs which continue to shrink down eventually reaching the nearly spherical bubble stage with a diameter close to or at the width of the channel.

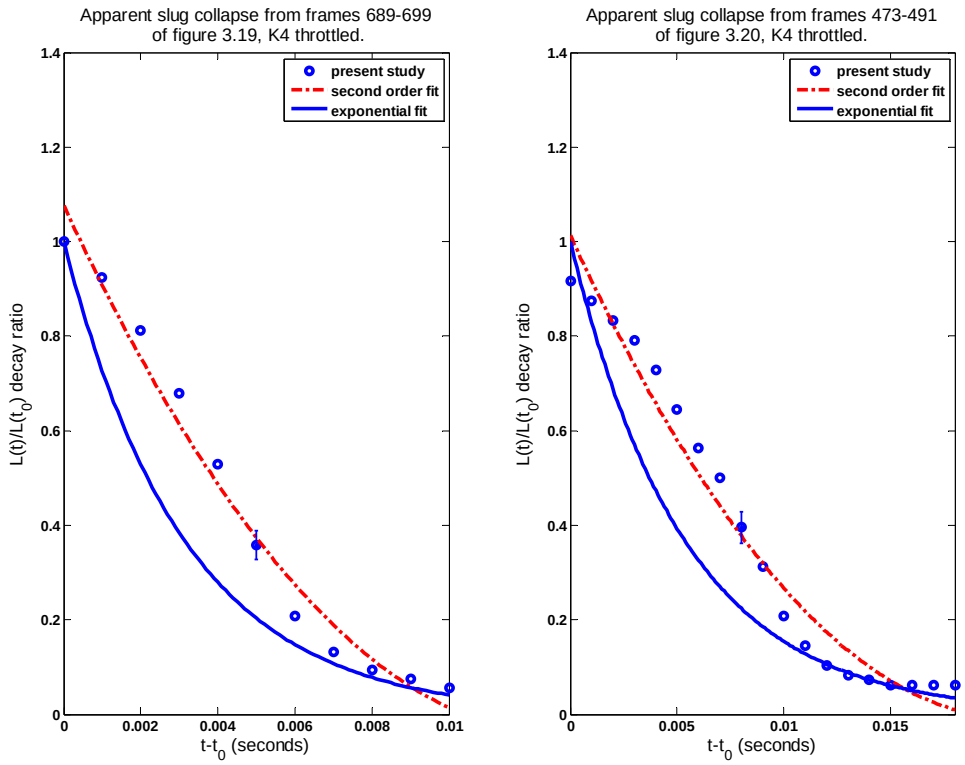

Figure 3.21: Curve fits to the measured decrease in length of the slugs in figures 3.19 and 3.20 through the apparent collapse process. The flow conditions are 10g/min flow rate, 1.76 W/cm^2 input heat flux and 88°C inlet fluid temperature.

The length of the slugs in the left-most channel of the K4 level in both figure 3.19 & 3.20 were measured as they underwent the apparent collapse process. The method of measurement as well as the listing of the variation in slug length over time and the uncertainty can be found in appendix D. From fig.3.21 it appears the second order curve fits give the best approximations of the trend in measured length of the slug over time. Higher order fits only appeared superimposed over the second order fit so the latter is thought to be sufficient.

Table 3.3: The second order approximations of the data shown in fig.3.20.

Figure 3.19	Figure 3.20
$\frac{L(t)}{L(t_o)} = 6839 \cdot \Delta t^2 - 175 \cdot \Delta t + 1$	$\frac{L(t)}{L(t_o)} = 2363 \cdot \Delta t^2 - 98 \cdot \Delta t + 1$

It's interesting to note that the upstream vapor-liquid interfaces shown in the bifurcation in frames 688 and 691 of fig.3.19 as well as frames 473 and 477 of fig.3.20 appear flat. In order for the interface to be curved the pressure in the vapor region must be higher than the pressure in the fluid surrounding liquid. The pressure drop across the interface is related to the surface tension of the fluid and the radius of curvature of the interface. If the interface is flat meaning the angle of contact of the interface with the wall is 90°, as it seems to be in frame 688, then the pressure drop across the interface is zero. Because of this the pressure in the surrounding fluid must increase to the value of the pressure inside the vapor region. A range of pressure drop across the vapor-liquid interface was calculated for varying radii of curvature of the interface and is shown in appendix F. It was found that the range of pressure drop across the interface was in the

same range as the magnitude of the oscillations of inlet pressure. So it seems that when the pressure at the inlet reaches one of its peak values it may cause the vapor slug at the bifurcation to collapse and flatten the upstream vapor-liquid interface in the process.

Li et al. [14] documented that the pressure of the fluid surrounding a vapor-liquid interface affects the shape of the interface. A high pressure region in the liquid surrounding an interface produces a flat vapor-liquid interface whereas a low pressure region allows the interface to be curved. Typically in the flows they observed it was found the upstream interface of the vapor slug was flat and the downstream interface was curved. The slug was shaped somewhat like a bullet traveling in the direction of the flow. This made it easy to determine the direction the bubble or slug was travelling; being that the high pressure region propelling the slug forward caused a noticeable deflection of the upstream interface.

However, the expansion and collapse of vapor slugs at the K4 location in this case has been shown to occur rapidly at frequencies that range much greater than the frequency of oscillation of inlet pressure. Also, as is shown in fig.3.20, other vapor phenomena happen at this location at frequencies of two or more orders of magnitude greater than the frequencies of the oscillations of inlet pressure. So it seems there is more affecting the local activity of the vapor than the global fluctuations of pressure.

It is found that oscillations of the vapor-liquid interface of a slug at the bifurcation comprise a substantial amount of the observed phenomena at this location. As was described in the introduction, both Li et al. [14] and Chang & Pan [19] observed similar vapor phenomena for unstable flows regarding bubble growth rate and oscillation of slug

length. However, their observations do not account for the drastic reduction in slug length in one of the cases of apparent collapse.

It is possible in the case of the apparent bubble collapse presented in figures 3.19 & 3.20 the bubble may not be losing as much volume as it appears to. In the K4 branching level the channel is 100μm wide but 250μm deep. The channel is 2.5 times as deep as it is wide.

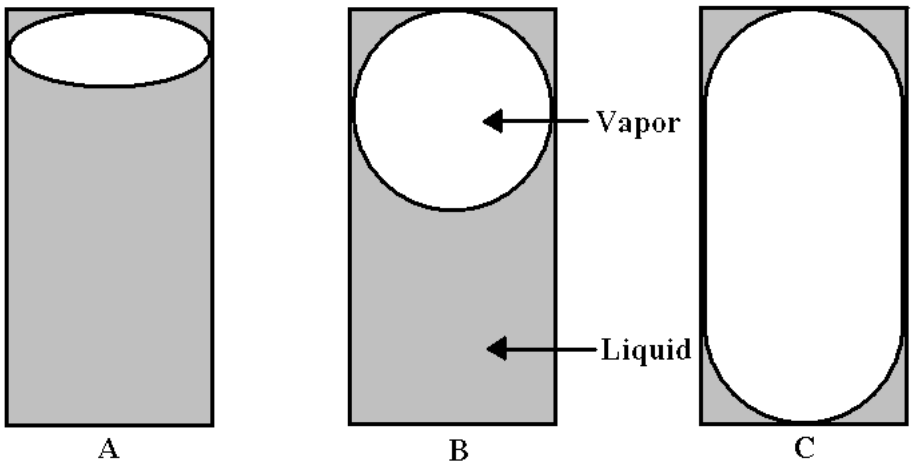

Figure 3.22: Cross-sectional view of three possible bubbles occupying the K4 channel. (A) represents a vapor "film" pushed up against the bottom of the Pyrex layer (possible if the buoyancy forces are high), (B) represents a bubble of circular cross-section which fills the width of the channel and (C) represents a possible configuration where the bubble fills the entire channel cross-section.

It could be the vapor slug in either the channel of figure 3.19 or figure 3.20 has a circular cross-section of diameter 100μm or is only a film of vapor pressed against the bottom of the Pyrex layer, either of which would make it appear to fill the entire channel as shown in fig.3.22. However, the latter option seems unlikely. It could be that in the process of the apparent collapse the aspect ratio of the bubble cross-section is changing; progressing from B to C as shown in fig.3.22. So while the bubble is apparently

shrinking horizontally it is expanding vertically until it fills the entire cross-section of the channel.

It seems possible this change in the aspect ratio of the bubble cross-section could be the result of the large pressure surge which sweeps through the fractal moving the vapor out and replacing it with fresh liquid. Also, such a pressure surge would help account for the extensive apparent volume loss of the bubble in fig.3.22 (B). The mere change in aspect ratio alone seems insufficient to explain the apparent volume loss but if the effects of the pressure increase on the local saturation enthalpy, as explained in the previous section, is taken into account it may be possible to explain why the bubble appears to be collapsing from an elongated slug to a small bubble before exiting the fractal. However, the results of the calculation performed in Appendix G shows the effect of compression alone due to the pressure increase would only decrease the void fraction by about 0.4% and the effect of the potential increase in saturation temperature due to the pressure increase would only reduce the void fraction by about 5%. In the current experiment it is seen vapor slugs initially on the order of 1mm in length appear to be collapsing down to spherical bubbles with a diameter on the order of 0.1mm. Assuming the initial cross-section of the bubble is shown in fig.3.22 (B) then the initial volume of the vapor slug would be around 7.9E-12m^2 whereas the ending volume of the bubble after collapse would be around 5.2E-13m^2. This is a reduction in volume of about 93%. So it would seem the above three possible explanations together (change of the aspect ratio of the bubble cross-section, increase in local saturation temperature and compression effects of pressure increase) are not sufficient to account for the large apparent decrease in length of the vapor slug.

Also, condensation of the vapor slugs at the K4 branching level was considered and could possibly be explained by thermal maldistribution of the input energy supplied by the heater rings on the bottom of the fractal. Since such a large length of the K4 branching level has no heater directly beneath it relies on conduction to supply heat to it from the heater rings further upstream. It could be that because of this the downstream section of the K4 branching level does not receive as much input energy as the upstream section. However, this seems unlikely due to the high thermal conductivity of Si. Nevertheless, a potential energy loss of a collapsing vapor slug at the K4 level was done and can be found in appendix H. The findings showed that even for an assumed channel wall temperature as high as 99°C it may be possible for a vapor slug at 100°C and 1 mm in length to condense down to half its initial size in 1 millisecond. The calculation is simple and meant only to investigate and compare the orders of magnitudes of the rate of energy removed from a vapor slug undergoing collapse and the rate of energy transferred between an annular region within a channel and the wall of the channel.

The downstream section of the K4 level in both the case with throttling at the inlet and the case without throttling showed very little presence of vapor. As has been shown the majority of the vapor activity occurs in the upstream section of the K4 level. The only occurrences of vapor activity in the downstream section of this level are the steady expansion of vapor through the channel or the small bubbles passing through that are the result of an apparent bubble collapse. However, most of the time the downstream section is occupied by single phase liquid. The exit of the test device was exposed to atmosphere and due to the construction of the vacuum chuck a small pool of the test fluid surrounded the periphery of the test device as is shown below in fig.3.23.

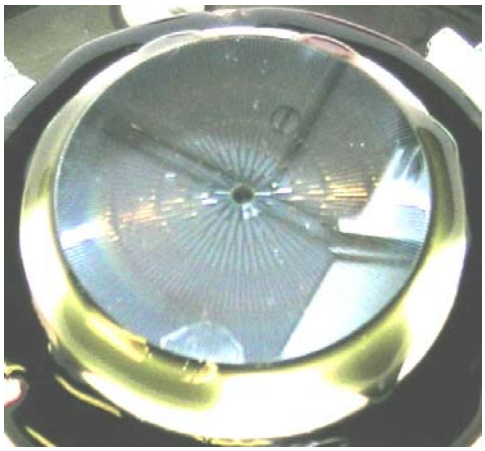

Figure 3.23: A picture of the test device during operation. Note the pool of test fluid surrounding the test device at the periphery.

It is possible that during the oscillation of the position of a vapor-liquid interface in the upstream section of the K4 level cool fluid was being sucked back into the test device from the periphery and then flushed out again. This could have cooled the device around the periphery and been at least a partial reason for the low amounts of vapor observed in the downstream section of the K4 level. It is possible this cool fluid sucked into the test device from the periphery was aiding in the apparent collapse of slugs at the K4 level.

3.3.5.4 Apparent Bubble Collapse in the K0 & K1 Branching Levels

The phenomena of apparent bubble collapses were also observed to happen in the K0 and K1 branching levels for the case with throttling at the inlet as well as the K1 branching level for the case without throttling at the inlet. This isn't to say that collapse happened nowhere else but only to say the apparent collapses were only observed at these locations in the movies which were collected. However, the process of apparent bubble collapse only happens at the K4 level for the case with throttling at the inlet in the regular and repeated fashion as is stated above.

In frames 838 and 840 of fig.3.24 vapor enters the K0 level channel from the inlet plenum and is then pinched off at the inlet of the K0 channel in frame 841. Following this the vapor is seen to break into two bubbles; a large one the right of about 0.5 millimeters in length and a small one on the left about 0.3 millimeters in diameter in frame 842. Then in frames 843-845 the large bubble to the left in frame 842 settles against the wall of the channel as it continues to shrink and eventually exits the channel in frame 846. Immediately following this occurrence another bubble collapse is observed and follows the same pattern as the one shown here. Other than these two collapses no others were observed at this location for the case with throttling.

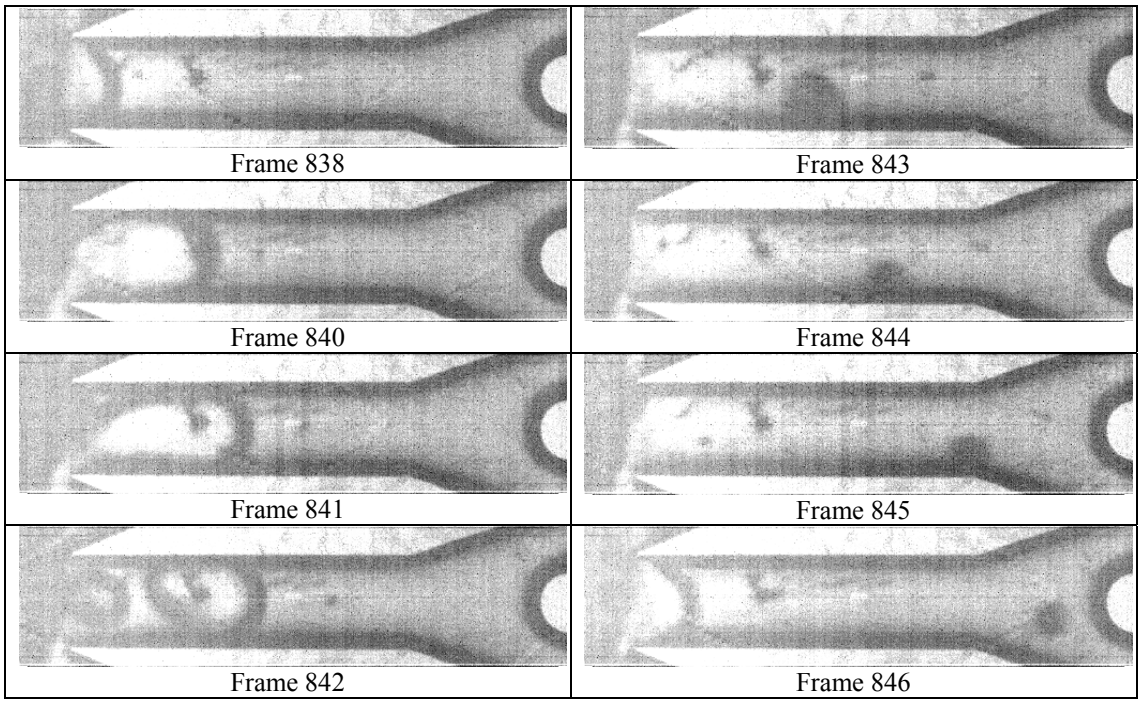

Figure 3.24: A series of images documenting an apparent bubble collapse at the K0 branching level with throttling at the inlet. The flow conditions are 10g/min flow rate, 1.76 W/cm^2 input heat flux and 88°C inlet fluid temperature. The images shown here were acquired at a rate of 1000fps. This was the only example found of this occurrence at the K0 level for both the throttled and non-throttled cases.

The apparent slug collapses in the K1 level are interesting because in both the case with throttling at the inlet and the case without throttling at the inlet the slug collapses as it's flowing upstream. In frame 197 of fig.3.25 a vapor slug in the right-most channel is pinched off and then is collapsed down in frames 198-200 before it is eventually pushed into the K0 level by another vapor slug in frame 201. The vapor slug that enters the right-most channel in frame 201 then proceeds to undergo a very similar process of collapse as previously described. Again this was the only example of an apparent bubble collapse at this location for the case with throttling at the inlet.

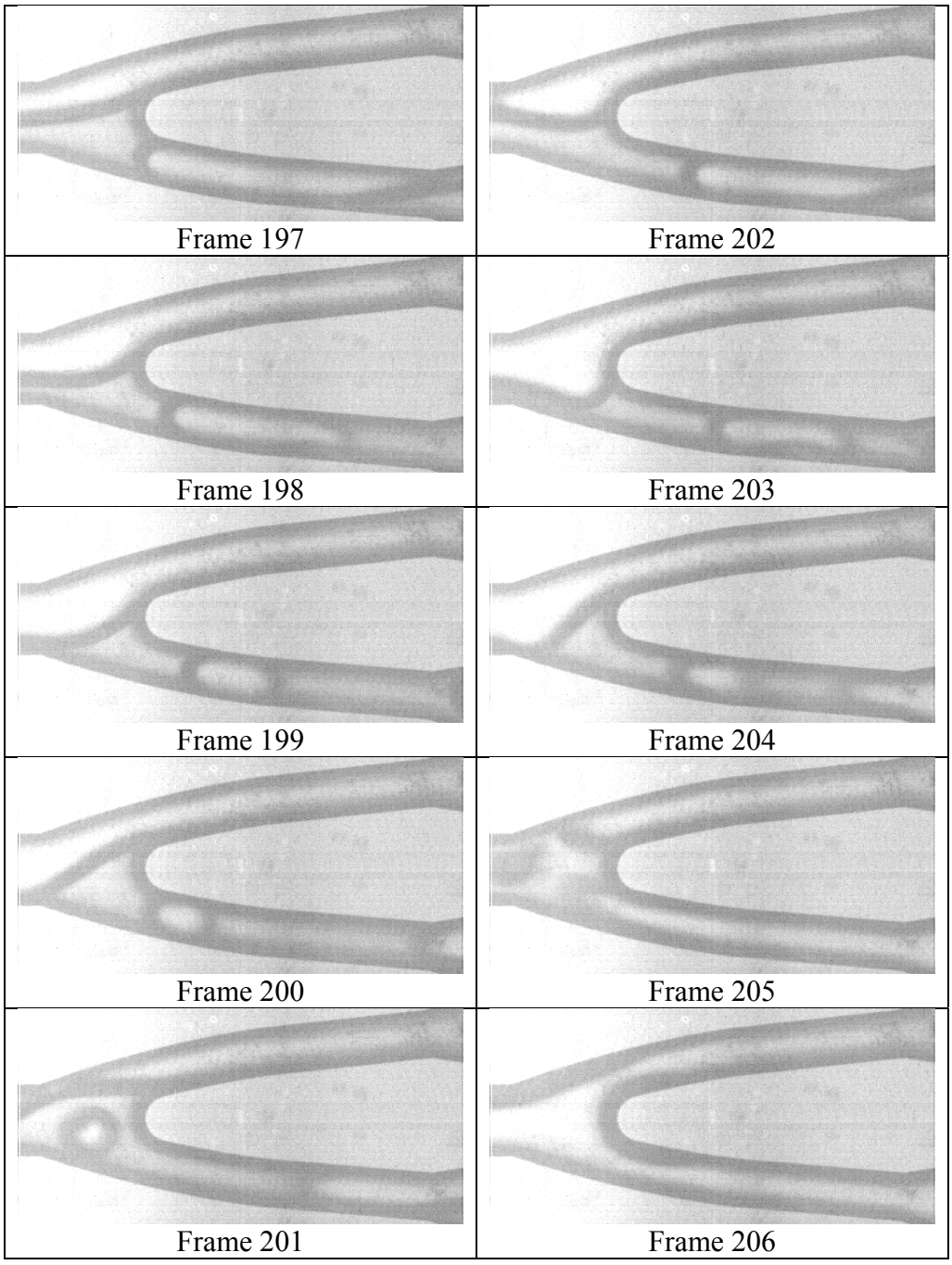

Figure 3.25: A sequence of images demonstrating two apparent successive bubble collapses at the K1 branching level with throttling at the inlet. The flow conditions are 10g/min flow rate, 1.76 W/cm^2 input heat flux and 88°C inlet fluid temperature. The images were recorded at 1000fps. This was found to be the only occurrence of apparent bubble collapses at this location for the throttled test case.

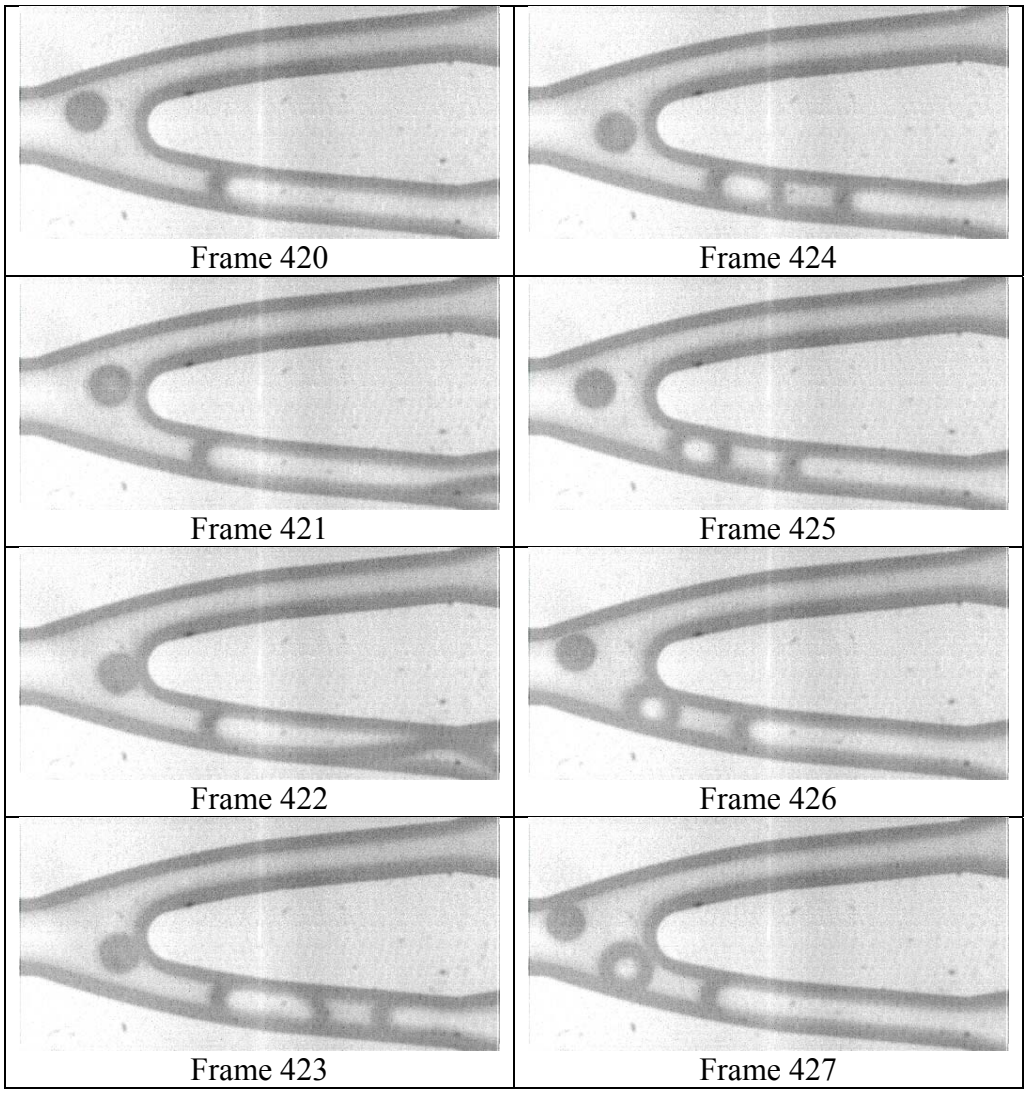

Figure 3.26: A sequence of images demonstrating an apparent bubble collapse at the K1 branching level without throttling at the inlet. The flow conditions are 10g/min flow rate, 1.76 W/cm^2 input heat flux and 88°C inlet fluid temperature. The frames were acquired at a rate of 1000fps. This was the only observed case of an apparent bubble collapse at the K1 branching level for the non-throttled case.

The process of apparent collapse in fig.3.26 is very similar to that shown in fig.3.25 with the exception only one collapse is seen to occur and the collapse bubble doesn't appear to be forced upstream due to the entry of new vapor flowing upstream. In frames 421 and 422 of fig.3.26 the vapor which enter the K1 channel in frame 420 it pinched of near the channel exit. Then in frames 423-427 the bubble appears to shrink

down as it flows upstream. As with the previous two cases this is the only observed incidence of an apparent bubble collapse at this location for the case without throttling.

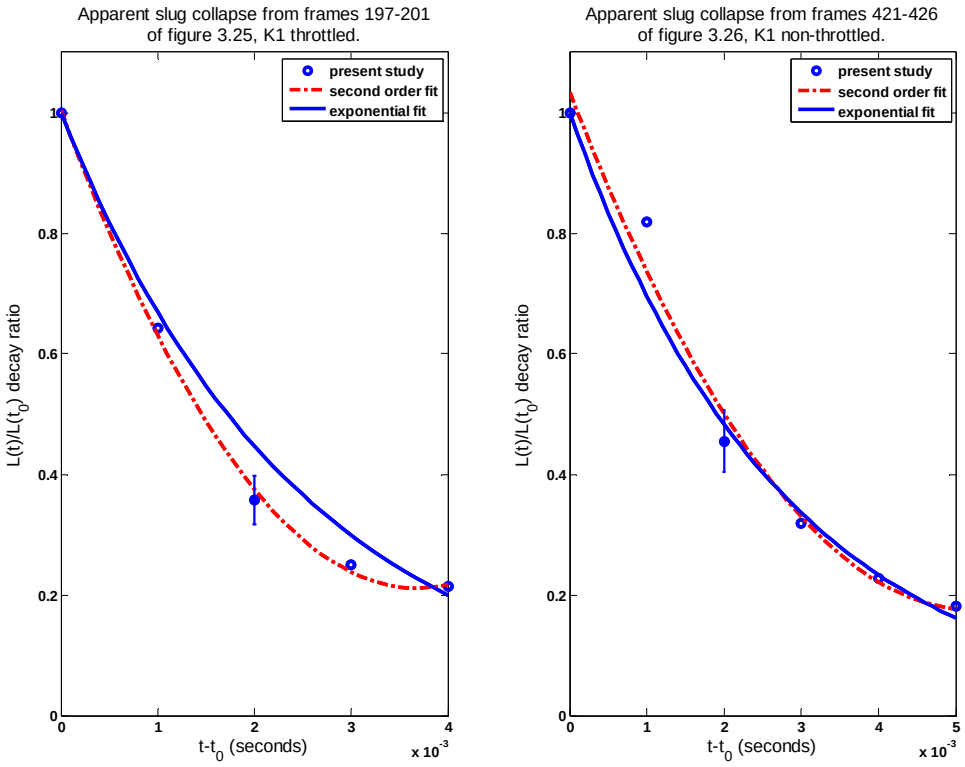

Figure 3.27: Approximations of the rate of apparent bubble collapse shown in figures 3.25 and 3.26. The flow conditions are 10g/min flow rate, 1.76 W/cm^2 input heat flux and 88°C inlet fluid temperature.

From fig.3.27 it looks as though the second order approximations again most closely fit the data measured in the present study. However, from the data from fig.3.23 it is hard to tell whether the exponential fit or the second order curve fit is best.

Table 3.4: The second order approximations of the data shown in fig.3.27.

Figure 3.25	Figure 3.26
$\frac{L(t)}{L(t_o)} = 58664 \cdot \Delta t^2 - 431 \cdot \Delta t + 1$	$\frac{L(t)}{L(t_o)} = 31654 \cdot \Delta t^2 - 330 \cdot \Delta t + 1$

3.3.5.5 Possible Nucleation & Rapid Expansion/Apparent Collapse

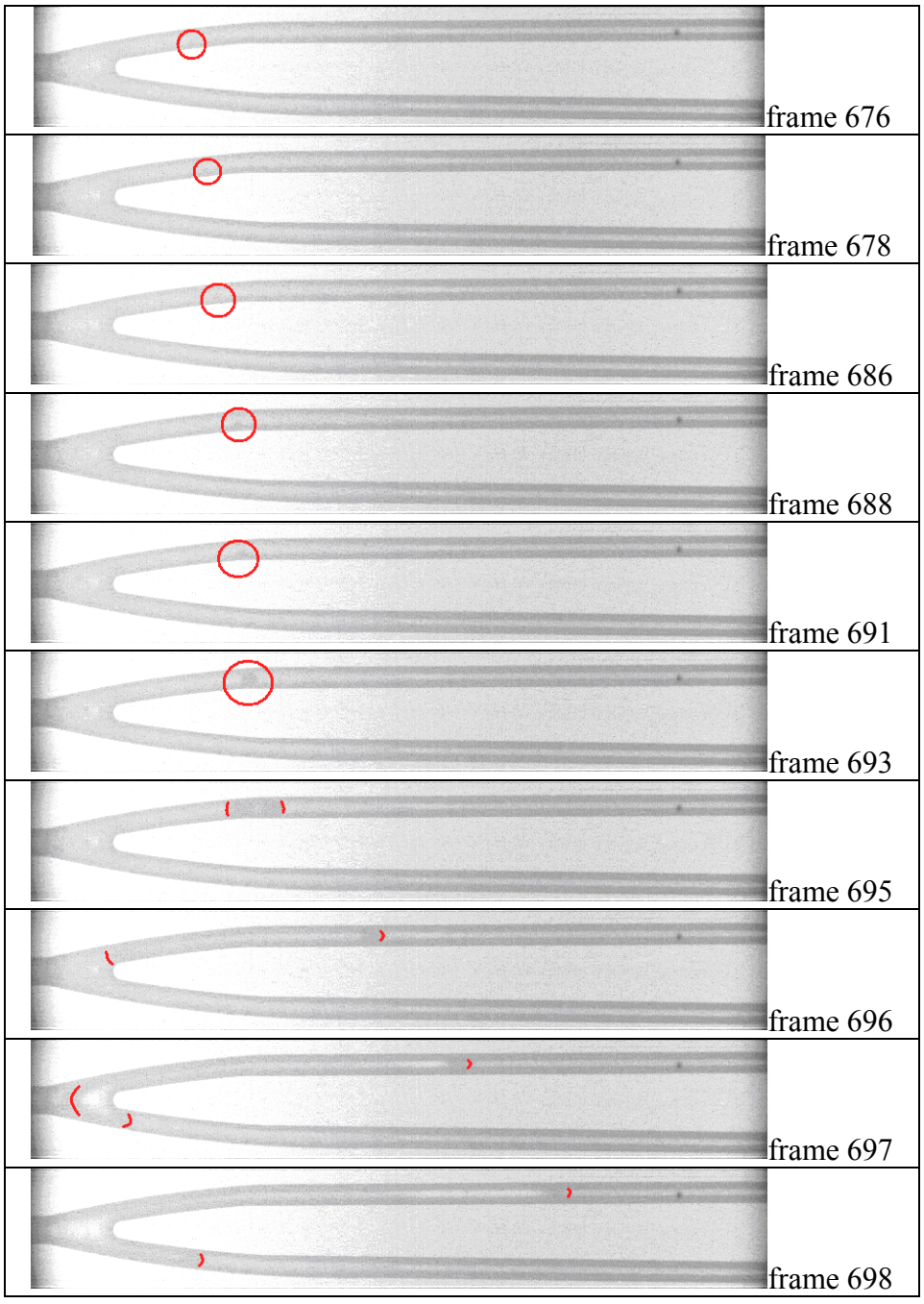

Figure 3.28: A sequence of images demonstrating what appears to be a nucleation and subsequent expansion of vapor at the K4 level with throttling at the inlet*. The flow conditions are 10g/min flow rate, 1.76 W/cm^2 input heat flux and 88°C inlet fluid temp. The frames shown were acquired at 1000fps.

Figure 3.28 documents the only apparent nucleation to occur at this location in either the throttled or non-throttled test case. It is unclear as to whether or not this is an instance of an actual nucleation due to the resolution of the images. It is possible the bubble nucleated somewhere upstream and broke off at an extremely small size below the ability of the camera to resolve with the magnification used and then grew substantially when it reached the K4 level. However, the bubble does appear to have nucleated just downstream of the bifurcation as shown in frame 674. Frames 674-691 show the growing bubble being dragged downstream along the channel wall until the bubble diameter reaches the width of the channel in frame 693. At this point it appears the liquid flow may have been diverted to the adjacent daughter channel because in frames 695-698 the bubble expands rapidly up and downstream fills the bifurcation and then expands down the adjacent daughter channel as well as into the downstream section of the K3 level. It should be noted the computational model[6] compared with the findings in this study predicts nucleation at close to this point as is shown in fig.3.36.

Figure 3.29 is difficult to understand; in it is displayed a bubble that expands and then immediately contracts nearly as fast as the initial expansion. In frame 400 of fig.3.29 a bubble enters the bifurcation region from upstream and then proceeds down the left-most channel shown until in frame 402 the bubble apparently gets trapped in the channel and then begins to expand up and downstream. From frame 402-412 the bubble expands and then from 412-418 the bubble apparently collapses down to nearly the original size before exiting the field of view and flowing into the downstream section of the K4 level.

[6] Model created by Brian Daniels [4]

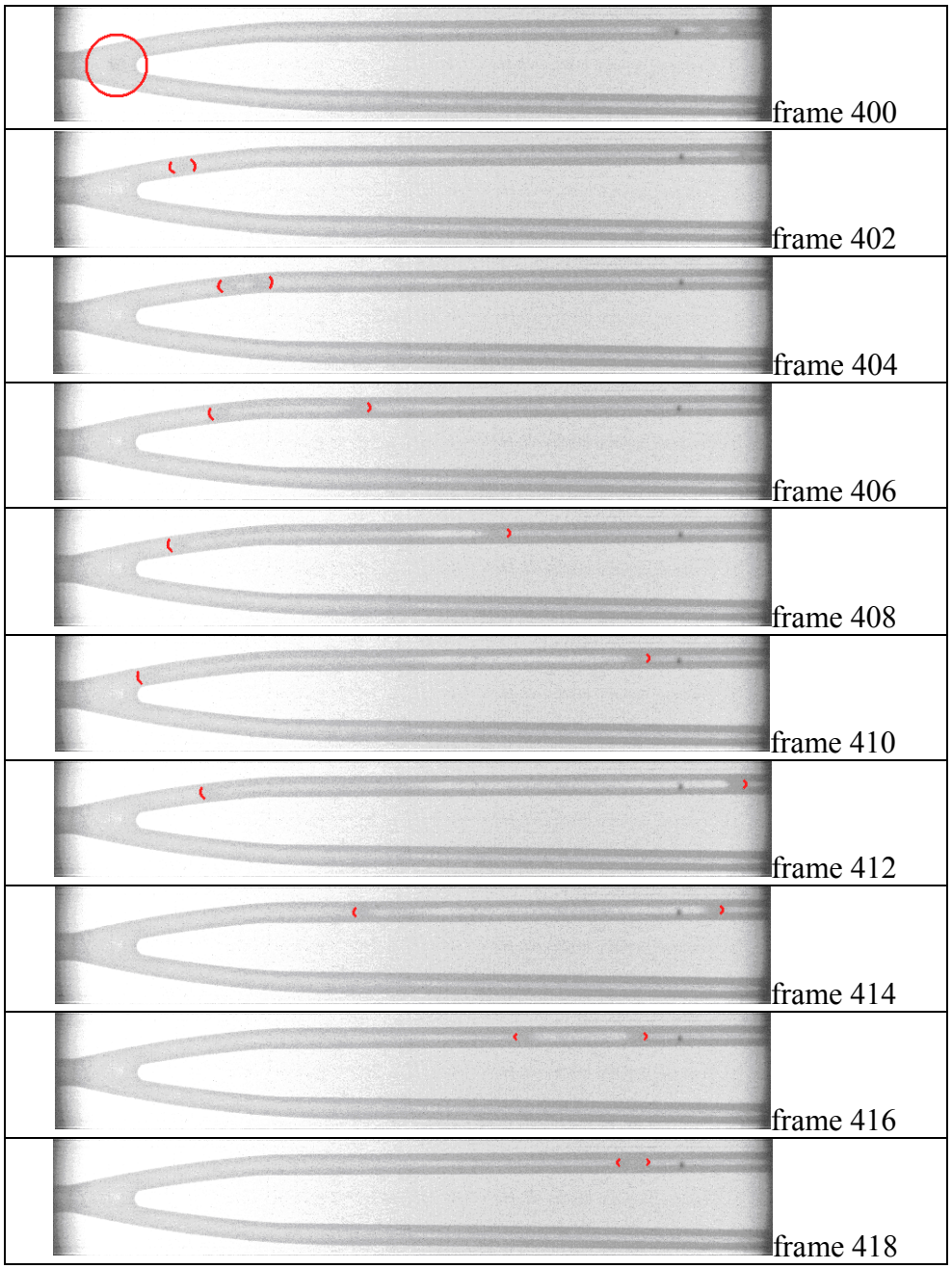

Figure 3.29: A Sequence of images documenting a rapid expansion and apparent collapse of a vapor bubble at the K4aaa1 location with throttling at the inlet*. The flow conditions are 10g/min flow rate, 1.76 W/cm^2 input heat flux and 88°C inlet fluid temperature. The frames shown here were acquired at a rate of 1000fps.

Both Chang & Pan [19] and Li et al. [14] reported exponential bubble growth rates for slugs observed in their respective experiments. For stable flow conditions, Chang & Pan [19] found the relation between time and growth rate of slug length using an exponential curve fit to be

$$\frac{L(t)}{L(t_o)} = e^{5.87\cdot(t-t_o)} \tag{3.3}$$

where t has units of seconds. Li et al. [14] found a similar expression for their data using an exponential curve fit for unstable flow conditions to be

$$\frac{L(t)}{L(t_o)} = e^{285\cdot(t-t_o)} \tag{3.4}$$

where t has units of seconds. These equations are used to generated predicted growth rate profiles and compared to what is found in the current experiment below in fig.3.30.

From fig.3.30 it appears a second order curve fit produces the best results. The predicted values shown using the relations found by Chang & Pan [19] and Li et al. [14] appear to under predict the growth rate of slugs in the K4 level. The exponential curves fit to the data gathered from figures 3.28 & 3.29 found the coefficients in the exponent to be roughly 805 and 367 respectively. These values are two orders of magnitude greater than what was found in Chang & Pan [19] but the same order of magnitude as what was found in Li et al. [14]. Chang & Pan [19] found the time constant to be 5.87 1/s whereas Li et al. [14] found their time constant to be 285 1/s.

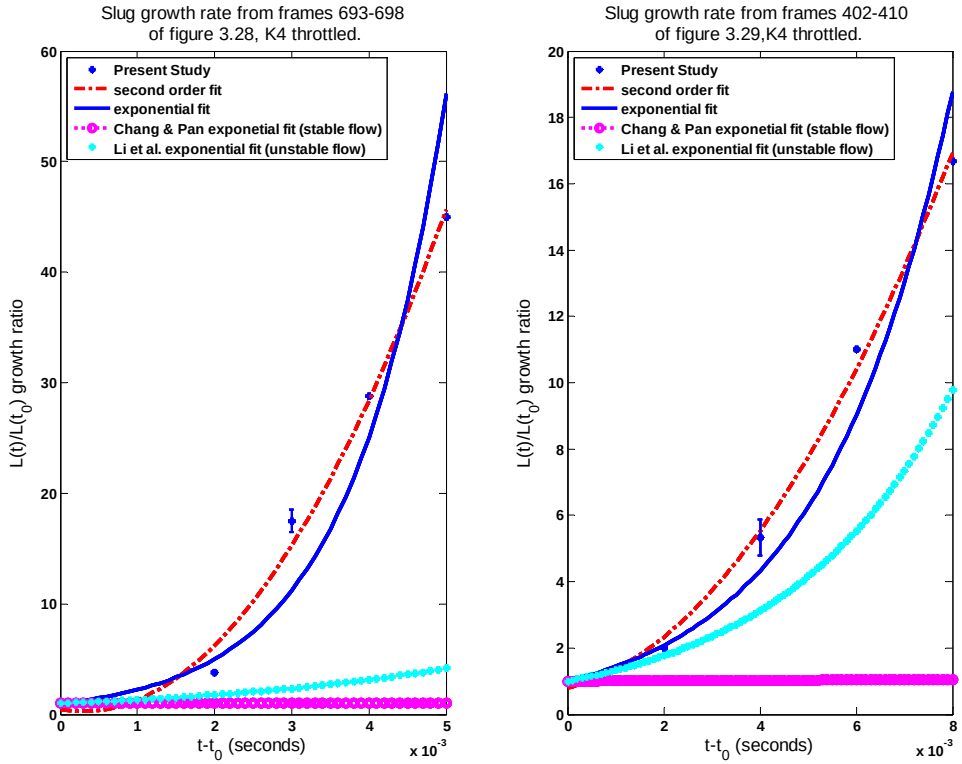

Figure 3.30: Approximations of the growth rate of slugs shown in figures 3.28 and 3.29. The curve fits found are compared with the findings of Chang & Pan [19] and Li et al. [14]. The flow conditions are 10g/min flow rate, 1.76 W/cm^2 input heat flux and 88°C inlet fluid temperature.

Table 3.5: Second order approximations of data shown in fig.3.30.

Approximate growth rate of frames 693-698 of fig.3.19	Approximate growth rate of frames 402-410 of fig.3.29
$\frac{L(t)}{L(t_o)} = 2052650 \cdot \Delta t^2 - 1232 \cdot \Delta t$	$\frac{L(t)}{L(t_o)} = 208333 \cdot \Delta t^2 + 350 \cdot \Delta t + 1$

Finally the apparent collapse which occurs during the latter frames of fig.3.29 is investigated along with an investigation of the entire group of frames accounting for both expansion and apparent collapse in fig.3.31 below.

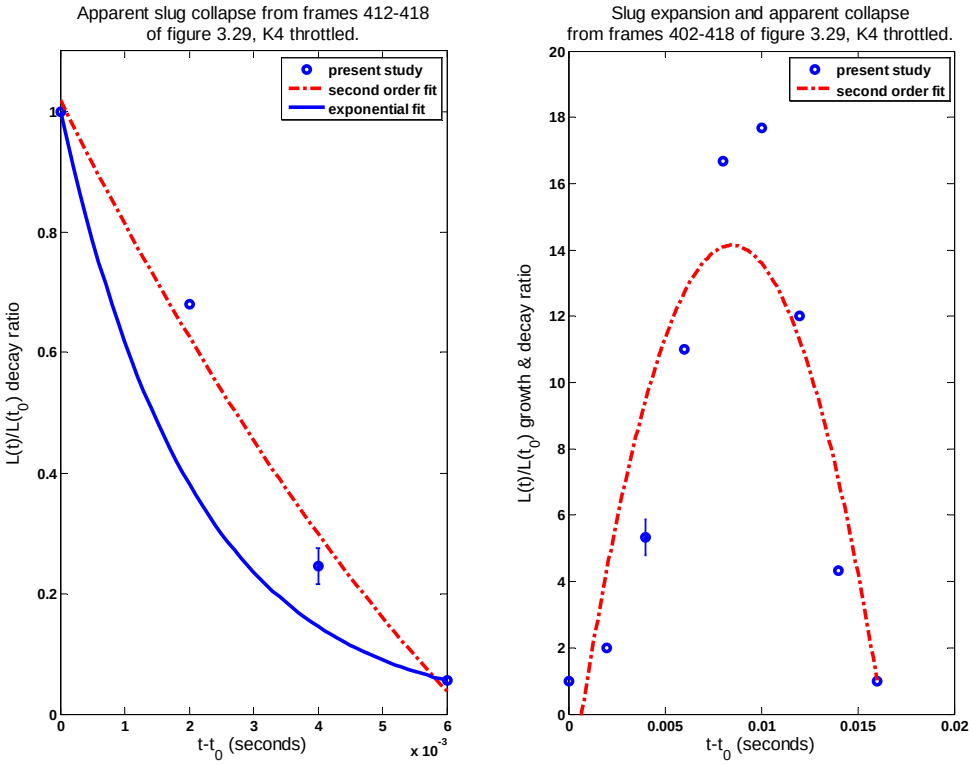

Figure 3.31: An approximation of the apparent collapse and the total growth and collapse rate of fig.3.29. The flow conditions are 10g/min flow rate, 1.76 W/cm^2 input heat flux and 88°C inlet fluid temperature.

Table 3.6: Second order approximations shown in fig.3.31.

Approximate rate of collapse of slug over frames 412-418 of fig.3.29	Approximate rate of expansion and collapse of slug over frames 402-418 in fig.3.29
$\frac{L(t)}{L(t_o)} = 8255 \cdot \Delta t^2 - 213 \cdot \Delta t + 1$	$\frac{L(t)}{L(t_o)} = -232413 \cdot \Delta t^2 + 3944 \cdot \Delta t - 3$

3.3.6 Observations at Bifurcations

The bifurcations in the test device play an important role in rerouting the flow of upstream vapor in the downstream direction. Once upstream flowing vapor reaches the bifurcation it appears favorable for the vapor to turn around and flow downstream in the adjacent channel if it is not itself blocked with vapor. If indeed it is blocked with vapor then the upstream flowing vapor in the first channel will continue on into the next upstream branching level. A presentation of this phenomenon is given below.

It was observed in all branching levels for both the test case with throttling at the inlet and the case without that reversed flow would not reach into the inlet plenum unless no downstream path in the tree was available to it. In other words it was evidenced from the phenomena observed that if vapor was flowing upstream once it reached a bifurcation it favored to flow down the adjacent channel rather than continuing upstream to the next branching level.

Figure 3.32 provides an example of vapor flowing upstream that continues on to the upstream branching level due to the adjacent daughter channel having a blockage of vapor. From frames 729-833 it is apparent that a small bubble is for the most part stagnant in the bottom-most channel. This seems to be an indication of a vapor blockage in the pair of its downstream daughter channels. In frames 729-803 a vapor slug propagates upstream in the left-most channel until it fills the bifurcation in frame 814. Then it continues upstream in frame 833 having no other path to expand down.

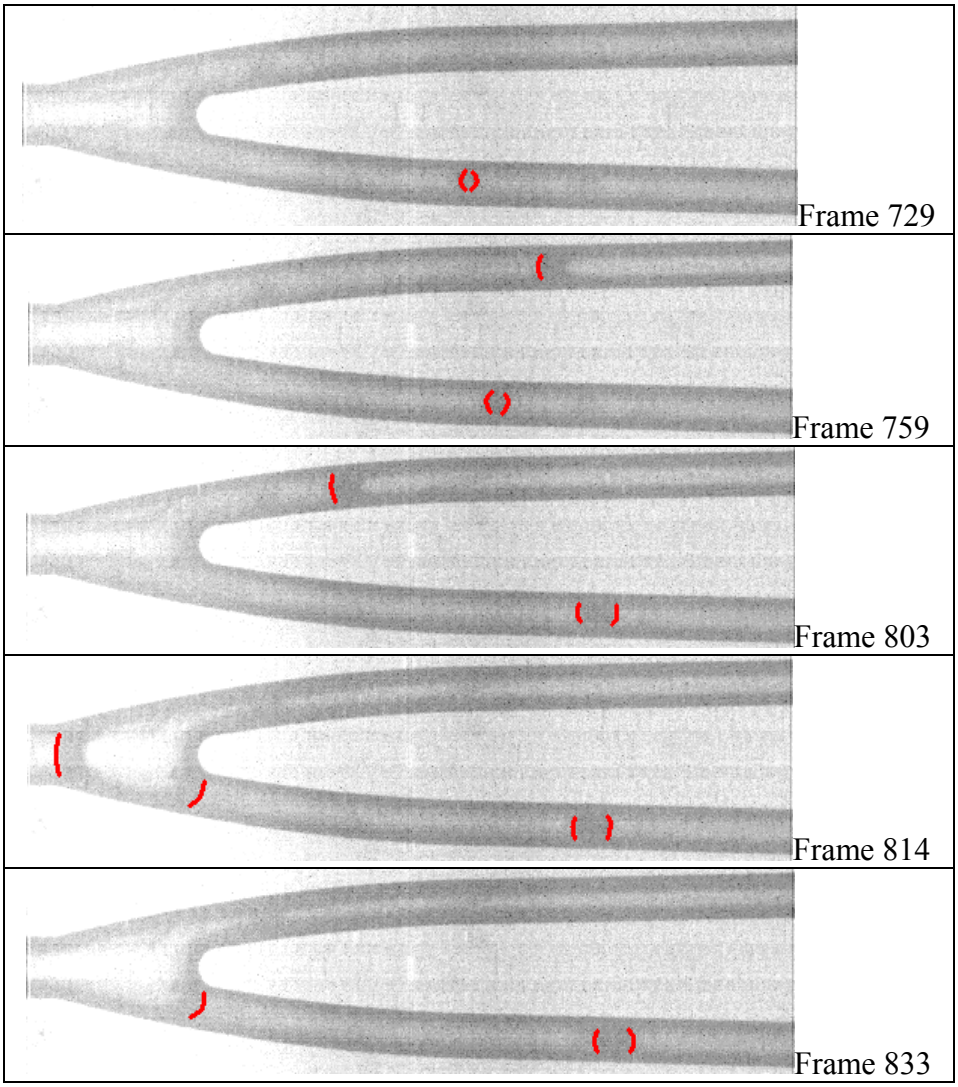

Figure 3.32: A sequence of images demonstrating vapor flowing upstream when the adjacent daughter channel is blocked*. Images were taken at the K3 branching level in the test case with throttling at the inlet. The flow conditions are 10g/min flow rate, 1.76 W/cm^2 input heat flux and 88°C inlet fluid temperature. Images were acquired at 1000fps.

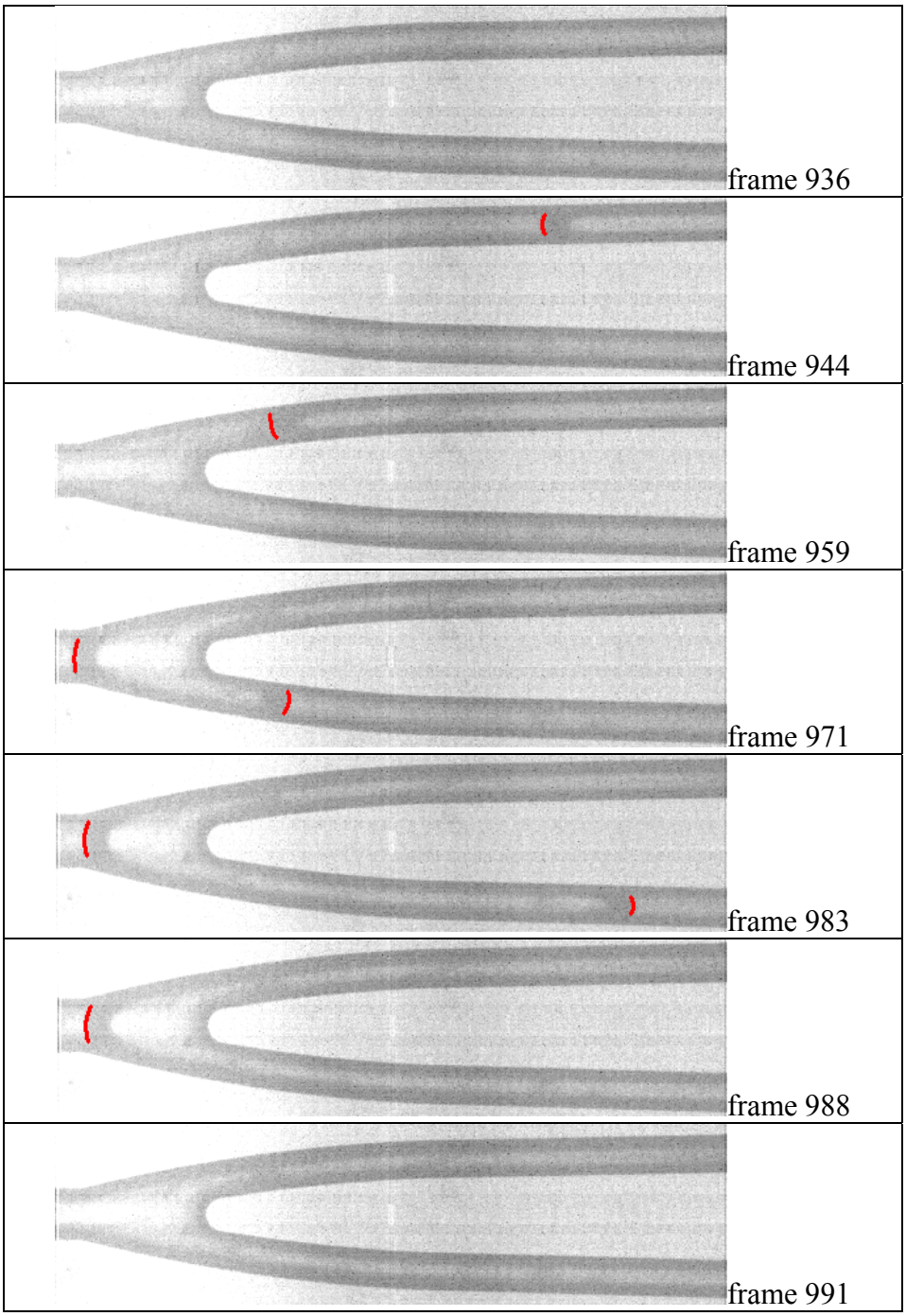

Figure 3.33: A sequence of images demonstrating a vapor slug traveling upstream favors curving around a bifurcation over continuing upstream*. Images were taken at the K3 branching level in the test case with throttling at the inlet. The flow conditions are 10g/min flow rate, 1.76 W/cm^2 input heat flux and 88°C inlet fluid temperature. Images were acquired at 1000fps.

Again, if the adjacent daughter channel is free of vapor then upstream bound vapor will turn and flow down it once it has reached the bifurcation. Figure 3.33 begins with the channels filled with single phase liquid in frame 936. In frames 944 and 959 a vapor slug enters and flows upstream in the left-most daughter channel. In frame 971 it has completely filled the bifurcation and proceeded to flow down the adjacent daughter channel as it continues to do in frame 983. Thus it is seen that in the absence of a vapor blockage in the adjacent daughter channel the vapor flowing upstream reverses direction after it reaches the bifurcation. Having filled the adjacent daughter channel with vapor in frame 988, and assuming it has filled downstream beyond the filled of view with vapor also, the vapor region then propagates upstream to the upstream branching level in frame 991.

Another common occurrence at the bifurcation regions is a bubble becoming trapped and then expanding up and downstream from the bifurcation. Typically this happens when a small slug enters the bifurcation region with a volume that is less than the volume of the bifurcation and, if allowed to form into a spherical shape, has diameter greater than the width of the channel downstream of the bifurcation. Figure 3.34 shows this phenomenon occurring at the bifurcation upstream of the K3 branching level for the case with throttling at the inlet. In frame 558 a bubble enters the bifurcation region from upstream in the K2 level and is trapped at the bifurcation in frame 559. Beginning in frame 593 the bubble expands; first down the left-most channel in frame 596 then once this channel is filled with vapor in frame 599 the bubble expands upstream from the

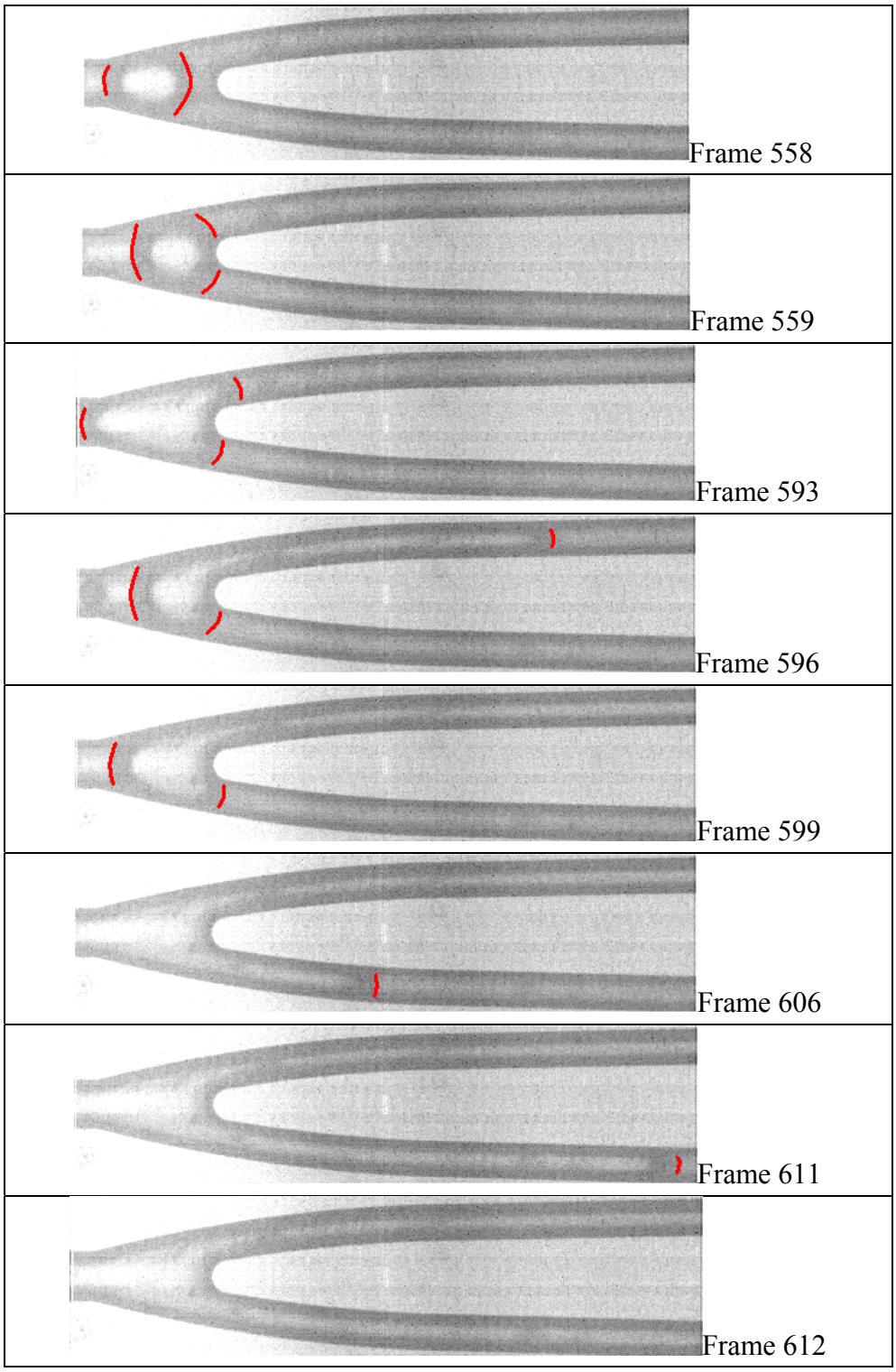

Figure 3.34: A bubble expands from the bifurcation at the upstream section of the K3 branching level in the case with throttling at the inlet*. The flow conditions are 10g/min flow rate, 1.76 W/cm^2 input heat flux and 88°C inlet fluid temperature. The frames presented here were captured at a rate of 1000fps.

bifurcation into the K2 level and down the right-most channel in frames 606 and 611 eventually filling the entire channel area in the field of view in frame 612.

3.4 Void Fraction

3.4.1 Results for Throttled and Non-Throttled Test Cases

As can be seen from figure 3.35 the profiles of time averaged void have a similar profile versus branching level. However, there are large differences between the reported void fraction values at the K0 level and the upstream section of the K4 level.

Notice the downstream section of the K4 level in both cases report exceptionally low void fraction values. This is due to the findings of the K4 level section documented earlier; very little observable vapor reached this section of the test device. There were the occurrences of oscillations of the vapor at the bifurcation, vapor slugs collapsing in the upstream section of K4 and the instances where no vapor would be observed in entire movies. Whenever vapor did appear in the downstream section it was usually in the form of a bubble making its way out rather than the long sustained annular regions of vapor expected at this location.

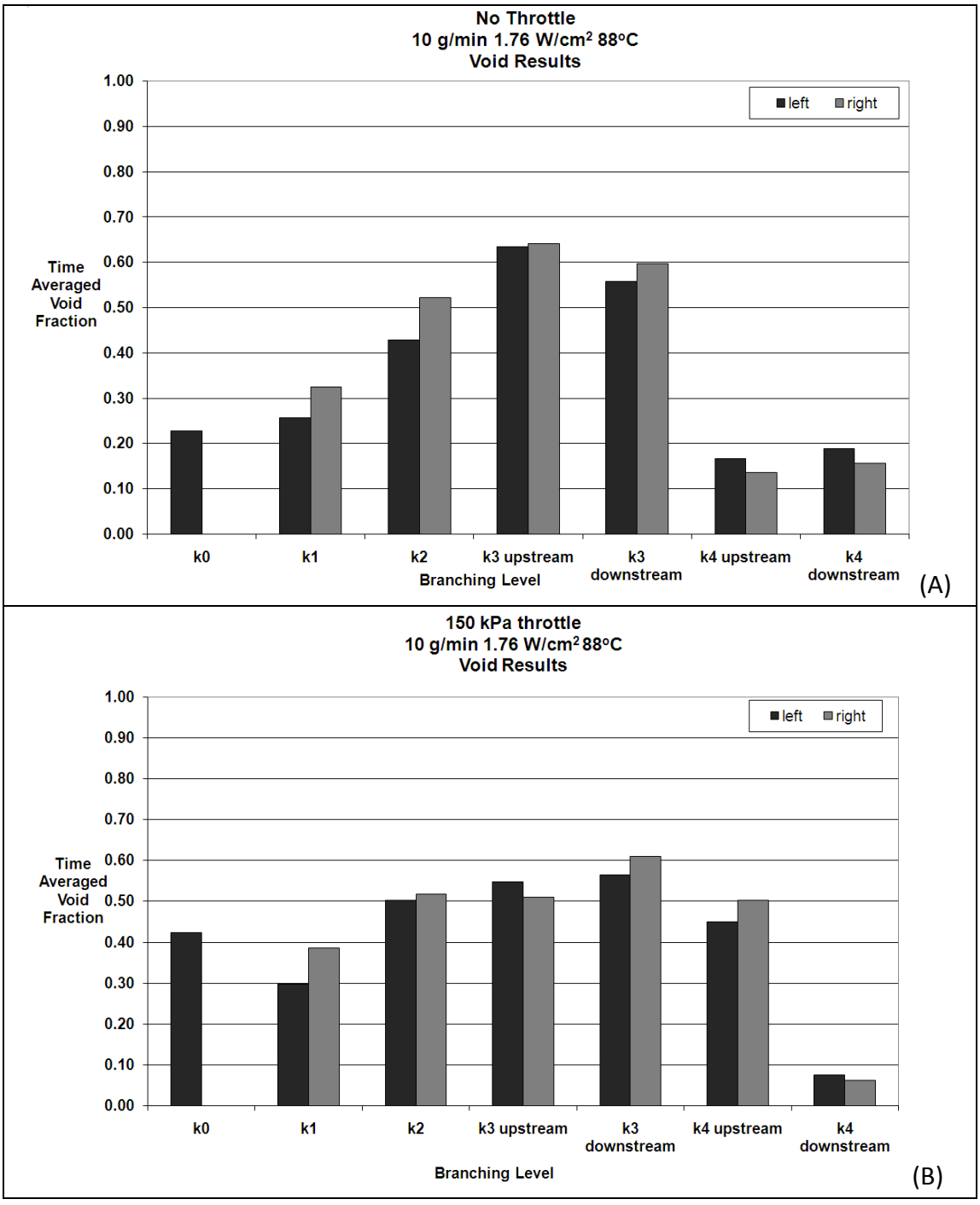

Figure 3.35: Time-averaged void fraction results[7] for the throttled and non-throttled test case 10g/min flow rate, 1.76W/cm^2 input heat flux and 88°C inlet fluid temperature. The estimated total uncertainty in measured void fraction was found to be +/-0.035; the calculations can be found in appendix D.

[7] Results computed using the image processing algorithm created by Douglas Heymann, Graduate Student, Oregon State University

It could be that the addition of the throttle valve at the inlet causes the vapor to, on average, move downstream in the flow network. Comparing fig.3.35 (A) with fig.3.35 (B) it seems the peak of the distribution may have been moved from the upstream section of the K3 level to the downstream section of the of the K3 level. This could then also shift the void fraction trend at the downstream section of the K3 level from fig.3.35 (A) to the upstream section of the K4 level in fig.3.35 (B). This could be a partial explanation as to why the void fraction is so much larger at the upstream section of the K4 level with the throttle valve engaged at the inlet. Comparing fig.3.17 with fig.3.25 it is shown that the position from which the downstream vapor-liquid interfaces oscillate moves downstream with the addition of the throttle valve at the inlet. In fig.3.17 the vapor expands from and contracts to the bifurcation whereas with throttling at the inlet the vapor never reaches back into the bifurcation as shown in fig.3.25.

3.4.2 Variations at K4 for Throttle vs. Non-throttle

The main difference in measured void fraction at the K4 branching level between the flow throttled at the inlet and the non-throttled flow was the drastic reduction of the presence and activity of vapor in the upstream section of the K4 branching level in the non-throttled case. Roughly 38% of the movies taken at the upstream K4 location in the case without throttling were found to have either no vapor at all or vapor present for less than 10 frames of the movie. This is compared with all of the movies showing vapor taken at the upstream K4 location for the throttled case. Further, the oscillation of the position of the vapor-liquid interface of a slug produced very low reported void fractions in the K4 level channels for the case without throttling. Even though it was found that a significant portion of the movies of the upstream K4 section for the throttled test case

exhibited oscillation of the position of the vapor-liquid interface the vapor region protruded much farther down the channel on average than did in the case of the oscillations for the case without throttling. Even considering the occurrences in the K4 level for the case with throttling where a slug collapsed down there was on average much greater amounts of vapor observe in the upstream section of the K4 level.

3.4.3 Variations at K0 for Throttle vs. Non-throttle

The increase in void fraction at the K0 level for the case with throttling at the inlet over the case without throttling at the inlet is surprising. This is due to the fact the long time scale movies taken at the inlet documented in the inlet pressure section showed increased amounts of single phase liquid residence time at the inlet while not changing substantially the vapor residence time at the inlet when the throttle valve was engaged upstream of the test device; see fig.A4 of the global inlet pressure characteristics of test device. Understanding this it would seem that liquid only phases were present at the inlet over longer durations of time with the throttle at the inlet than without. With the K0 level immediately downstream of the inlet one would expect this trend to carry over to the K0 level. However, as is apparent from fig.3.35 it did not.

It could be that the throttle indeed made it more difficult for vapor to reach the inlet plenum and as a result the vapor was held up in the K0 level for a longer period of time in the case with throttling at the inlet before it was able to proceed all the way into the inlet. However, in the K0 level movies viewed of the case with throttling at the inlet it appear in the majority vapor was already in the inlet and vapor flowing upstream entered the K0 channel and then merged with the vapor already in the inlet plenum. This happened in the majority of the movies. So it seems this would not support the idea of

the vapor being held in the K0 branch for a longer period of time with throttling at the inlet.

The cause for the discrepancy may have to do with the rate at which video data of the flow was acquired. The time required to record a movie was about 1 second and the time required to upload one movie was about 2.5 minutes bringing the total recording and uploading time to around 2.5 minutes. This is compared to the typical vapor-liquid cycle time at the inlet of about 4 seconds. It could be the times at which data was acquired at K0 for the case with throttling at the inlet occurred on average more during the time in which vapor filled the inlet plenum then when data was acquired at the K0 level for the case without throttling at the inlet. However, if this was true it would seem as though there would be greater differences in the trend of time averaged void for the rest of the branching levels. Further, these are time averaged void values and should account for any differences in instantaneous void caused by the documented vapor-liquid cycle at the inlet. So at this point it is difficult to understand this trend in observed phenomena and measured void fraction at the K0 level for the case with throttling at the inlet with the observed phenomena in long time scale movies taken at the inlet.

3.4.4 Model Predictions of Void Fraction

Figure 3.36 shows the model[8] predictions for the flow conditions of the present experiment (B) along with the extremes of the results of a perturbation analysis[9]. In this perturbation analysis the flow rate was varied from 9-11 g/min and the heat input was varied from 18-22 watts (1.58 – 1.94 W/cm^2), which generated a matrix of 15 different

[8] Used numerical model created by Daniels et al. [4]

[9] Perturbation analysis performed by Douglas Heymann, Graduate Student, Oregon State University

cases. The purpose was to understand the magnitude of the effect of slight changes in flow conditions on the reported values of void fraction in the model. The two extremes of the perturbation are shown, which are the case in which the lowest vapor should be generated (A) and the highest amount of vapor should be generated (C).

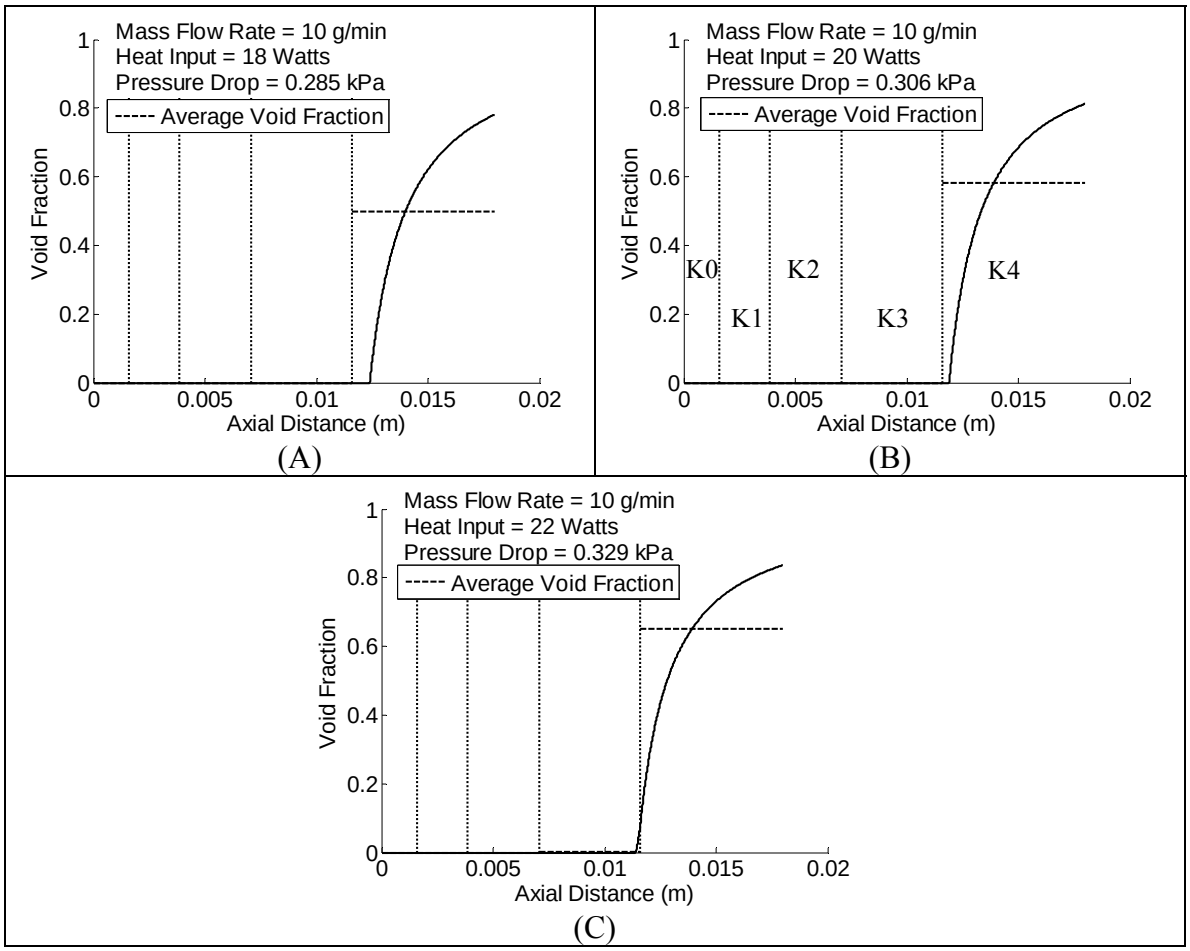

Figure 3.36: Predicted void fraction distribution from model with an inlet fluid temperature of 88°C. The vertical dashed lines represent the streamwise location of the different branching levels and the horizontal dashed lines represent the void fraction values averaged over each branching level.

To compare the total amount of void fraction measured in the flow network to the total amount predicted by the model an area weighted average is performed below. It is

assumed the values of measured void fraction are uniform and therefore present in all channels of a given branching level.

The area weighted average is calculated below according to equation 3.5

$$\alpha_{avg,tot} = \sum_{i=0}^{4} \frac{A_{ki}}{A_{tot}} \cdot \alpha_{ki} \qquad 3.5$$

where A_{ki} is the planform area of the channels in the entire branching level of one tree not including the bifurcation region, A_{tot} is the total planform area of one tree, and α_{ki} is the time averaged void fraction at a branching level. To compute the averaged measured void fraction in one channel of a given branching level the measured void fraction in the right and left channels (excluding K0) at a given branching level were averaged first and that average value was used for α_{ki} and assumed uniform throughout the branching level. In the event that two separate camera field of views were used to capture the entire length of a given branching level (as in the case of K3 and K4) then the up and downstream sections of measured void fraction for each channel were averaged and following this the measured void fraction of both the right and left channel were averaged and that value was used for α_{ki} and assumed uniform throughout the branching level. The results of the calculation for the predicted values from the model and the measured values of void are listed in table 3.7 & table 3.8, respectively, the calculations can be found in appendix I.

Table 3.7: Area weighted average void fraction values from model results shown in Fig.3.36.

10 g/min 1.58 W/cm^2 heat input (A)	10 g/min 1.76 W/cm^2 heat input (B)	10 g/min 1.94 W/cm^2 heat input (C)
$\alpha_{avg,tot}$=0.28	$\alpha_{avg,tot}$=0.32	$\alpha_{avg,tot}$=0.36

Table 3.8: Area weighted average void fraction values from experimental results shown in fig.3.35.

10g/min 1.76 W/cm^2 without throttling at inlet (A)	10g/min 1.76 W/cm^2 with throttling at inlet (B)
$\alpha_{avg,tot}$=0.31	$\alpha_{avg,tot}$=0.37

So comparing the experimental average void values from table 11 to the average with the average void value for 10g/min 20 watts from table 10 the values appear similar. In fact, the averaged value for the case without throttling matches the value predicted by the model for 10 g/min 1.76 W/cm^2 within the uncertainty limits. The difference in average void between the model and the experimental case with throttling at the inlet could be due to the measured flow conditions of the experiment deviating from the specified conditions of 10 g/min 1.76 W/cm^2 used for analysis in the model.

4 Conclusions

It appears from the above analysis that the results for the predicted amount of vapor by the model compared to the measured amount of vapor in the present experiment may well be in agreement for the target test case of 10 g/min, 1.76 W/cm^2, 88°C. However, the distribution of the vapor throughout the flow network predicted by the model is substantially different. This disagreement is most likely due to limitations of the model itself.

The main limitations of the model are the fact it does not include the physical bifurcation region in the flow network used for the analysis, it does not include flow reversal and the flow network used for analysis in the model consists of a single tree as compared with the 16 trees of the flow network used in the present experiment. Rather

than having a physical bifurcation incorporated in the model when a channel bifurcates into a new branching level there is an immediate division from one channel into two channels along the streamwise direction. Also, the model assumes when a bubble is nucleated it will continue to grow as it moves down stream and eventually exits the flow network.

Clearly the bifurcations are necessary to be taken into account regarding flow phenomena. As has been shown above they are the areas of bubble expansion as shown in fig.3.34 as well as a sort of holding chamber for some bubbles as in fig.3.17 and fig.3.11. Also they are the regions in which upstream bound vapor can turn around and flow downstream as shown in figure 3.33.

Flow reversal appears to be very important as well. Nucleation is not seen to occur anywhere upstream of the K4 branching level and even there only one potential occurrence is documented as shown in fig.3.28. Actually it is more realistic to say the effects or results of nucleation are not seen in the branching levels upstream of the K4 level. That is to say at those upstream branching levels no occurrence of small bubbles growing along the channel wall and then departing once a certain diameter is reached is observed in the present experiment. Yet the measured void fraction in these branching levels is non-zero and actually quite substantial. Based on flow observations the presence of vapor in these branching levels is the result of flow reversal happening in the tree being investigated and thus flowing upstream into the field of view or flow reversal happening at another location in the flow network reaching the inlet plenum and then entering the tree under investigation and flowing downstream into the field of view.

Because of the vapor interplay between trees as a result of flow reversal it becomes necessary to include multiple trees in the model to make an accurate comparison between measured and predicted values of void fraction. As is shown in fig.3.1 once vapor enters the inlet it can travel down any available tree since all are fed by the inlet plenum. Thus it is not surprising that the model predictions of the distribution of void vary so drastically from the measured distributions for the case in which flow reversal is present. Had no flow reversal occurred then it is possible the model predictions would have more closely matched what was measured.

It should be noted that the measured values of void fraction are reported for single channels in the tree moving along the streamwise direction of the flow network. However, it was determined that the vapor phenomena was not localized to any specific tree or path in a tree based on global movies taken of the test device operating under the test conditions. In the model all of the channels of a given branching level in the tree are taken into account. The values of void fraction predicted by the model are only given for a single channel but it assumes the value given is true for every channel in that branching level.

The addition of the throttle valve directly upstream of the inlet did not stop flow reversal from happening but merely decreased the characteristic frequency of the inlet pressure oscillations as well as the characteristic frequency of the period when single phase liquid was present at the inlet plenum. The pressure drop applied across the throttle valve was around 100 times larger than the pressure drop across the test device yet the magnitude of the oscillations of inlet pressure did not change much only the frequency of the oscillations. Seemingly the throttle valve made it more difficult for the

vapor to flow upstream reflected by the increase in time require to reach the inlet plenum as shown in fig.3.4.

The magnitude of the oscillations of inlet pressure for the case without throttling in the present study is an order of magnitude less than those found by Qu & Mudawar [15] for their device when it was unthrottled. However, when they employed the throttle valve in their experiment they found that even with increasing the heat flux by a factor of roughly three a significant decrease in the magnitude of the oscillations of pressure drop across their test device was observed.

It is thought the reason the magnitude of the oscillations of inlet pressure in the present study don't decrease is due to the fact upstream flowing vapor has several points in the flow network to turn around and flow downstream rather than being forced to continue expanding upstream. At the beginning of each branching level upstream flowing vapor can turn around and flow downstream which has been observed to happen as long as no blockage is present in the adjacent channel as shown in figure 3.33. The fact that the test device in the present study provides alternate paths for vapor to flow down rather than continue upstream is thought to be the reason for the relatively low magnitude of oscillations.

Muwanga et al. [21] observed oscillation magnitudes of inlet pressure an order of magnitude lower than Qu & Mudawar [15] as well. Recall their test device had a series of cross-link channels horizontally etched across the test device to provide upstream flow of vapor an alternate path to continuing upstream into the inlet plenum.

5 Recommendations for Future Work

The main limitation of this study was the range of possible test cases set by the limitations of the physical test pieces. The test cases for the present study occupy a very small region of the test cases documented in the literature which not many other investigators have studied. This condition made direct comparisons between the behavior and characteristics of the test device in the present study and devices in other studies very difficult or impossible. Testing at higher heat fluxes and flow rates is necessary to make such comparisons. Also, the results found in the present study may not be representative for the characterization of the test device due to the very low flow rate used in the test cases. The phenomena could change substantially if the flow rate and heat flux were increased large amounts.

To determine how evenly Nichrome heaters on the bottom of the test device distribute heat a series of tests in which the test device is operated with only two of the heater rings energized should be performed. Three test cases should be run; 1) no power supplied to the inner heater ring, 2) no power supplied to the middle heater ring and 3) no power supplied to the outer heater ring. In these tests the total power level supplied to the test device should remain constant but the distribution of that power to each ring will change. In the first test case the middle heater will receive the normal power sent to it with the addition of the power sent to the inner heater ring. In the second test case the power normally sent to the middle heater ring will be divided unequally between the outer and inner heater rings due to the difference in area they cover. Finally, in the third test case the power normally sent to the outer heater ring would be sent to the middle heater ring.

Then, operating the test device according to each of the test cases listed above, HSHR movies should be recorded of vapor phenomena in the test device and flow observations should be made and compared between the different test cases to see what the sensitivity of the device is to any thermal energy maldistribution. Phenomena of special interest to check for are apparent collapses of long vapor slugs at the upstream section of the K4 branching level as well as any apparent bubble collapses anywhere else in the flow network as well as flow reversal. Differences observed in flow phenomena could indicate non-uniform heating.

Also, regarding the apparent bubble collapses in the upstream section of the K4 branching level, it might be useful to send a larger energy to the outer heater ring perhaps in increments of 5% until the apparent bubble collapse phenomena is no longer observed and then make a note of that value of heat input compared to the value calculated from the uniform heat flux condition.

Finally, it would be useful to test the device in a closed flow loop. Currently the exit of the device is open to atmosphere during operation. Because the manifold acts as a sort of reservoir for fluid exiting the test device it is very difficult or nearly impossible to maintain a constant level of fluid. This means that the reported outlet flow rate does not record the actual outlet flow rate of the test fluid exiting the test device but the recorded values fluctuate up and down depending on whether the level of fluid in the manifold is either increasing or decreasing. Thus true outlet flow rate measurements cannot be made with the current experimental setup.

References

[1] Mudawar, Issam, "Assessment of High-Heat Flux Thermal Management Schemes", IEEE Transactions on Components and Packaging Technologies, VOL. 24, NO. 2, June 2001

[2] Kandlikar, Satish, G., "Fundamental Issues Related to Flow Boiling in Minichannels and Microchannels", Experimental Thermal and Fluid Science VOL. 26, December 2001, pp.389-407

[3] Tuckerman, D.B., Pease, R.F.W., "High-Performance Heat Sinking for VSLI", IEEE Electron Device Letters, VOL. EDL-2, No.5, May 1981, pp.126-129

[4] Daniels, Brian J., Pence, Deborah V., Liburdy, James A., . "Predictions of Flow Boiling in Fractal-Like Branching Microchannels", Proceedings of IMECE2005: 2005 ASME International Mechanical Engineering Congress and Exposition, November 5-11, 2005, Orlando, Florida USA

[5] Wu, H.Y., Cheng, P., 2004, "Boiling Instability in Parallel Silicon Microchannels at Different Heat Flux", Elsevier International Journal of Heat and Mass Transfer, April 2004, pp. 3631-3641.

[6] Kennedy, J.E., Roach Jr., G.M., Dowling, M.F., Abdel-Khalik, S.I., Ghiaasiaan, S.M., Jeter, S.M., Quershi, Z.H., 2000, " The Onset of Flow Instability in Uniformly Heated Horizontal Microchannels", Journal of Heat Transfer, Vol. 122 February 2000, pp.118-125.

[7] Xu, Jinliang, Zhou, Jijun, Gan, Yunhua, 2004, "Static and Dynamic Flow Instability of a Parallel Microchannel Heat Sink at High Heat Fluxes", Elsevier Energy Conversion and Management, March 2004, pp. 313-334.

[8] Qu, W., Mudawar, I., "Prediction and Measurements of Incipient Boiling Heat Flux in Microchannel Heat Sinks", Int. J. of Heat and Mass Transfer, VOL. 45, 2002, pp. 3933-3945

[9] Kawaji, M., Chung, P. M.-Y., "Adiabatic Gas-Liquid Flow in Microchannels", Microscale Thermophysical Engineering, VOL. 8, 2004, pp.239-257

[10] Serizawa, Akimi, Feng Ziping, Kawara, Zensaku, "Two-Phase Flow in Microchannels", Experimental Thermal and Fluid Science, VOL.26, 2002, pp.703-714

[11] Saisorn, Sira, Wongwises, Somchai, "Flow Pattern, Void Fraction and Pressure Drop of Two-Phase Air-Water Flow in a Horizontal Circular Micro-Channel", Experimental Thermal and Fluid Science, VOL.32, 2008 pp.748-760

[12] Kasza, K. E., Didascalou, T., Wambsgnass, M.W., "Microscale Flow Visualization of Nucleate Boiling in Small Channels: Mechanisms Influencing Heat Transfer", Proceedings of International Conference on Compact Heat Exchangers for the Process Industries, New York, Begell House Inc., 1997 pp.343-352

[13] Chen, Tailian, Garimella, Suresh V., "Measurements and High-Speed Visualizations of Flow Boiling of a Dielectric Fluid in a Silicon Microchannel Heat Sink", Int. J. of Multiphase Flow, VOL.32, 2006, pp.957-971

[14] Li, H.Y., Tseng, F.G., Pan, Chin, "Bubble Dynamics in Microchannels. Part II: Two Parallel Microchannels", Int. J. of Heat and Mass Transfer, VOL 47, 2004, pp.5591-5601

[15] Qu, Weilin, Mudawar, Issam, 2004, "Transport Phenomena in Two-Phase Micro-Channel Heat Sinks", Journal of Electronic Packaging, vol. 126 June 2004, pp. 213-224.

[16] Hetsroni, G., Mosyak, A., Pogrebnyak, E., Segal, Z., "Periodic Boiling in Parallel Microchannels at Low Vapor Quality", Int. J. of Multiphase Flow, VOL. 32, 2006, pp.1141-1159

[17] Jiang, Linan, Wong, Man, Zohar, Yitshak, "Phase Change in Microchannel Heat Sink Under Forced Convection Boiling", Proceedings of IEEE International Conference on MicroElectro Mechanical Systems, IEEE, 2000, pp.397-402

[18] Kosar, Ali, Kuo, Chih-Jung, Peles, Yoav, "Supression of Boiling Flow Oscillations in Parallel Microchannels by Inlet Restrictors", Journal of Heat Transfer, VOL. 128, March 2006, pp.251-260

[19] Chang, K.H., Pan, Chin, "Two-Phase Flow Instability for Boiling in a Microchannel Heat Sink", Int. J. of Heat and Mass Transfer, VOL. 50, 2007, pp. 2078-2088

[20] Lee, J.D., Pan, Chin, "Dynamics of Multiple Parallel Boiling Channel Systems with Forced Flows", Nuclear Engineering and Design, VOL. 192, 1999, pp.31-44

[21] Muwanga, R., Hassan, I., Macdonald, R., "Characteristics of Flow Boiling Oscillations in Microchannel Heat Sinks", Journal of Heat Transfer, VOL.129, October 2007, pp.1341-1351

[22] Kandlikar, Satish G., 2004, "Heat Transfer Mechanisms During Flow Boiling in Microchannels", Journal of Heat Transfer, Vol. 126 February 2004, pp. 8-16.

[26] Cullion, Rebecca.," Quantifying Void Fraction Variations in a Fractal-Like Branching Microchannel Network", Ph.D. Dissertation, Oregon State University, December 2005

[27] Ide, Hideo, Kimura, Ryuji, Kawaji, Masahiro, "Optical Measurement of Void Fraction and Bubble Size Distributions in a Microchannel", Heat Transfer Engineering VOL. 28, 2007, pp. 713-719

[28] Walchli, S., Stampanoni, M., Rudolf von Rohr, Ph., "Multiphase Flow Visualization in Microchannels Using X-ray Tomographic Microscopy (XTM)", pp. 52-53

[29] Revellin, R., Thome, J.R., "A New Type of Diabatic Flow Pattern Map for Boiling Heat Transfer in Microchannels", J. Micromech. Microeng. VOL.17, 2007 pp.788-796

[30] Alharbi, Ali Y., Pence, Deborah V., Cullion, Rebecca N., "Fluid Flow Through Microscale Fractal-Like Branching Channel Networks", Journal of Fluids Engineering, VOL. 125, No. 6, November 2003, pp.1051-1057

[31] Pence, D., Enfield, K., "Inherent Benefits in Microscale Fractal-Like Devices for enhanced Transport Phenomena", Design and Nature II, Collins & C.A. Brebbia, 2004 WIT Press, pp.317-327

[32] Pence, D.V., Improved Thermal Efficiency and Temperature Uniformity Using Fractal-Like Branching Channel Networks, Proc. Int. Conf. On Heat Transfer and Transport Phenomena in Microscale, ed. G.P. Celata, Begell House: New York, 2000 , pp.142-148

[33] Chen, Y., Cheng, P., " An Experimental Investigation on the Thermal Efficiency of Fractal Tree-Like Microchannel Nets", Int. J. of Heat and Mass Transfer, VOL.32, 2005, pp.931-938

[34] Pence, Deborah V., "Reduced Pumping Power and Wall Temperature in Microchannel Heat Sinks with Fractal-Like Branching Channel Networks", Microscale Thermophysical Engineering, VOL.6, 2002, pp.319-330

[35] Alharbi, Ali Y., Pence, Deborah V., Cullion, Rebecca N., "Thermal Characteristics of Microscale Fractal-Like Branching Channel", Journal of Heat Transfer, VOL. 126, No. 5, October 2004, pp.744-752

[36] Daniels, Brian, Liburdy, James A., Pence, Deborah V., "Adiabatic Flow Boiling in Fractal-Like Microchannels", Heat Transfer Engineering, VOL. 28, 2007, pp.1-9

[37] Hetsroni, Gad, Mosyak, Albert, Segal, Zelik, "Nonuniform Temperature Distribution in Electronic Devices Cooled by Flow in Parallel Microchannels", IEEE trans. on

Components and Packaging Technologies, VOL.24, No.1, March 2001, pp.1521-3331

[38] Qu, Weilin, Mudawar, Issam, "Flow Boiling Heat Transfer in Two-Phase Microchannel Heat Sinks-I. Experimental Investigation and Assessment of Correlation Methods", Int. J. of Heat and Mass Transfer, VOL. 46, 2003, pp.2755-2771

[A1] Lahey Jr., R.T., Moody, F.J., "The Thermal Hydraulics of a Boiling Water Nuclear Reactor", 1977, ANS.

[F1] White, Frank M., "Fluid Mechanics" 5th ed., New York, McGraw-Hill, 2003, pp.30-31

[H1] Incropera, Frank P., DeWitt, David P., "Fundamentals of Heat and Mass Transfer" 5th ed., New Jersey, John Wiley & Sons, 2002, pp.626-627

Appendices

Appendix A: Instability Criteria

One possible model, at least in part, could describe the unstable phenomena occurring within a microchannel undergoing flow reversal. This is the Ledinegg instability. In part was said because the Ledinegg model was derived for macro-level channels and may not consider important parameters governing the physics at the micro-level.

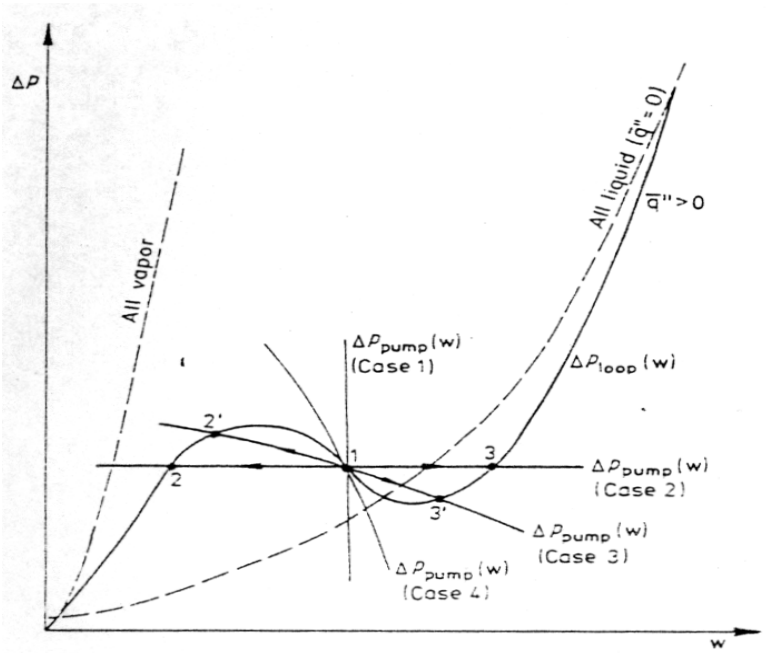

Figure A1: Example of pressure drop vs. flow wise velocity of a given channel with 4 different pump profiles superimposed. Cases 1 & 4 are stable configurations and cases 2&3 are unstable from Lahey & Moody [A1].

Figure A1 shows that stable configurations (1&4) are those with a pump demand curve that intersects the channel's demand curve at only one spot (point 1). Unstable configurations are those with a pump demand curve that intersects the channel's demand curve in more than one location. This is the case with cases 3&4 from fig.A1 for example in case 4, points 3 and 2 are one and the same as far as the system is concerned

since the operation point cannot deviate from the channel demand curve. So as the flow rate is decreased and eventually reaches point 3, at which the pump is no longer able to supply the required pressure head to overcome the evaporation forces acting on the vapor fronts, thereby allowing them to move upstream, the system will immediately jump to point 2 and operate at that flow rate which is drastically reduced from point 3, thereby greatly increasing the amount of boiling in the channel.

Kanlikar's Force Derivations from Kandlikar [22]:

Kandlikar [22] derived three expressions for forces which are thought to play an important role in flow reversal in microchannels.

The evaporation momentum of a vapor front, $F_M^{'}$, is defined as:

$$F_M^{'} = \frac{q^{"}D}{h_{fg}}\frac{q^{"}}{h_{fg}}\frac{1}{\rho_g} = \left(\frac{q^{"}}{h_{fg}}\right)^2\frac{D}{\rho_g} \qquad \text{eq.A1}$$

The inertia force of the liquid, $F_I^{'}$, is defined as:

$$F_I^{'} = \rho_l V^2 D = \frac{G^2 D}{\rho_l} \qquad \text{eq.A2}$$

The surface tension force at the vapor-liquid interface, $F_S^{'}$, is defined as:

$$F_S^{'} = \gamma\cos(\theta) \qquad \text{eq.A3}$$

where θ is the contact angle of the vapor front and the wall. Figure A2 illustrates how the forces act on the vapor front.

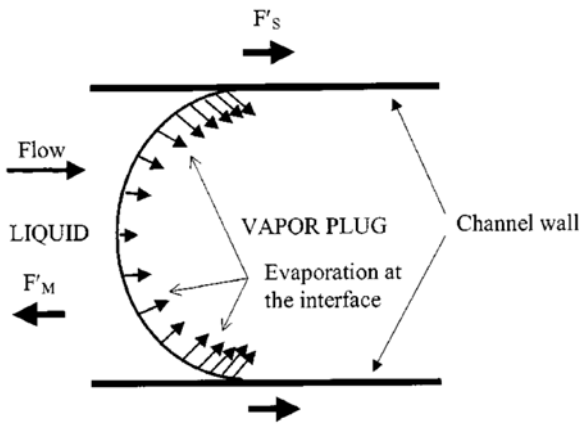

Figure A2: Kandlikar's diagram of the forces acting upon a vapor front from Kandlikar [22].

Kandlikar [22] then used the above expressions to create two new non-dimensional terms K1,

which is the ratio of $F_M^{'}$ to $F_I^{'}$, and K2, which is the ratio of $F_M^{'}$ to $F_S^{'}$.

$$\mathbf{K_1} = \frac{\left(\frac{q}{h_{fg}}\right)^2 \frac{D}{\rho_G}}{\frac{G^2 D}{\rho_L}} = \left(\frac{q}{G h_{fg}}\right)^2 \frac{\rho_L}{\rho_G} \qquad \text{eq.A4}$$

$$\mathbf{K_2} = \frac{\left(\frac{q}{h_{fg}}\right)^2 \frac{D}{\rho_G}}{\sigma} = \left(\frac{q}{h_{fg}}\right)^2 \frac{D}{\rho_G \sigma} \qquad \text{eq.A5}$$

Appendix B: Matlab Algorithms

Sample algorithm used to analyze movies for void fraction:

```
clear
clc

for i=1:10;
    a{i}=['00' num2str(i-1)];
end

for i=11:100;
    a{i}=['0' num2str(i-1)];
end

for i=101:214;
    a{i}=[ num2str(i-1)];
end

base=imread('HS_10_20_88_F16_H5_6_k0_013008_base_010.tif');
bwbase=imread('Current_BW_Base_HS_10_20_88_F16_H5_6_k0_013008.TIF');
for j=1:107
    for i=1:1019
        disp(['Processing image ' num2str(i) ' of file ' num2str(j-1)]);
        filename=['HS_10_20_88_F16_H5_6_k0_150_013008_' a{j} '.tif'];
        image=imread(filename,i);
        image=imabsdiff(image,base);
        image=medfilt2(image,[5 5]);
        image=im2uint8(50.*image);
        image=imsubtract(image,imcomplement(bwbase));
        image=medfilt2(image,[2 2]);
        image=imdilate(image,strel('disk',3));
        image=imfill(image,'holes');
        image=imerode(image,strel('disk',1));
        image=imadd(image,im2uint8(edge(bwbase,'zerocross')));
        image=imclose(image,strel('disk',9));
        image=imerode(image,strel('square',5));
        image=im2bw(image,.58);
        image=medfilt2(image,[5 5]);
        image=imopen(image,strel('disk',6));
        image=imadd(image,edge(bwbase,'zerocross'));
        image=imclose(image,strel('disk',3));
        image=imerode(image,strel('square',3));
        void(i,1)=sum(sum(im2bw(image)))/sum(sum(im2bw(bwbase)));
        filename_out=['HS_10_20_88_F16_H5_6_k0_013008_150_' a{j}
'b_set_2.tif'];
        imwrite(image,filename_out,'tif','writemode','append');
    end
    xlswrite(['HS_10_20_88_F16_H5_6_k0_013008_150_'  a{j}  'set_2'],void);
end
```

Once void fraction was calculated each movie was averaged and written to an Excel file using the following algorithm:

```
clear
clc

%ending movie number
k=107
%creates index string for files 0-9
for i=1:10;
    a{i}=['00' num2str(i-1)];
end
%creates index string for files 10-99
for i=11:100;
    a{i}=['0' num2str(i-1)];
end
%creates index string for files 100 and up
for i=101:(k+1);
    a{i}=[ num2str(i-1)];
end

% this loop reads the time series void fraction results for each movie
% then averages all 1018 values and stores the average in the matrix M

for j=1:(k+1);
    filename=['HS_10_20_88_F16_H5_6_k0_013008_150_' a{j} 'set_2.xls'];
    data=xlsread(filename,'A1:A1019');
    M(j)=mean(data);
end
% transpose row vector M to column vector N
N=M';
% write excel file
xlswrite('HS_10_20_F16_H5_6_k0_013008_150_average_void_set_2_1_105',N)
```

APPENDIX C: Instrument Calibration

C.1 Calibration of the Inlet and Differential Pressure Transducers and the RTD at the Inlet.

To calibrate the inlet pressure transducer, the differential pressure transducer for the throttle valve and the RTD at the inlet an Omega calibration unit was used, model number PCL-1B, serial number 9955. also, an Omega pressure module was used in conjunction with the Omega calibration unit , model number PCL-MB, serial number GQS-26484. The pressure module had a range of 0-100 psia and an accuracy of .05% of full scale. The equation associated with the calibration curve for the inlet and differential pressure transducers are shown in eq.C.1. and eq.C.2, respectively.

$$y = 340.230x - 0.437 \quad \text{C.1}$$

$$y = 25.653x - 38.243 \quad \text{C.2}$$

Also, an Omega temperature module was used with the calibration, model number PCL-MR-1, serial number GRT-3605. The temperature module range is 400Ω. The equation associated with the calibration curve is shown in eq.C.3.

$$y = 2.6225x - 262.58 \quad \text{C.3}$$

No calibration of the mass flow meter was calibration. The output of this device was a 0 to 10 V square wave, a frequency of 1000 Hz was associated with a flow rate of 4 g/min.

$$y = \frac{4}{1000}x \quad \text{C.4}$$

C.2 Measurement of Power Sent to Heater Rings

To find the power supplied to the heater rings deposited on the bottom of the fractal a voltage divider was constructed[10] to reduce the amount of voltage being sent to the DAQ board installed in the computer being used for measurements. This was required because more power was being supplied to the heaters than could be directly measured by the daq board. It had a range of -10 to 10 volts and voltage in excess of 50 V were being supplied to the outer ring of the test piece. Figure C.1 and Table C.1 show the construction of the voltage divider

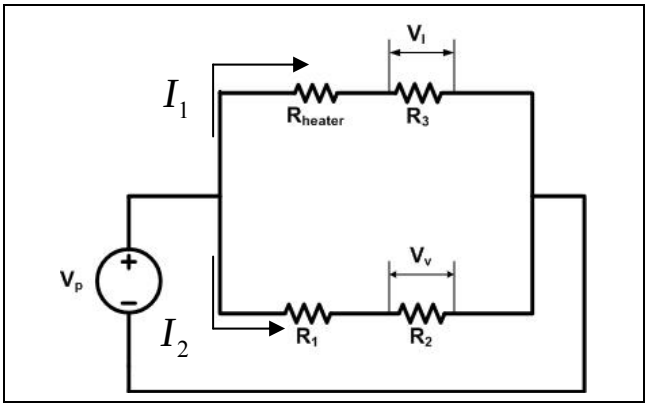

Figure C.1: Schematic of voltage divider used for measurement of voltage and current supplied to fractal.

Table C.4: Definitions of values in fig.C.1

V_H : Voltage sent to heater ring
I_H : Current sent to heater ring
V_p : Voltage for power supply
V_V : Voltage for voltage measurement (DAQ board)
V_I : Voltage for current measurement (DAQ board)
R_1 : Resistance 1 (45.3 kohm)
R_2 : Resistance 2 (47.1 kohm) for voltage measurement
R_3 : Resistance 3 (0.60 ohm) for current measurement
I_1 : Current 1
I_2 : Current 2

[10] Voltage divider constructed by Younghoon Kwak, Dan Krebs and Lee Edward, Graduate Students, Oregon State University

In order to calculate V_H and I_H equations C.5, C.6 and C.7 were used

$$V_H = V_p - V_I \tag{C.5}$$

where

$$V_p = V_v\left(\frac{R_1 + R_2}{R_2}\right) \tag{C.6}$$

$$I_H = I_1 = \frac{V_I}{R_3} \tag{C.7}$$

$$P_H = V_H I_H \tag{C.8}$$

After V_H and I_H were know they were multiplied to find the power supplied to the heater ring, P_H,shown in eq.C.8. the relative power sent to each ring was determined according to the relative area each ring was designed to supply energy to as defined in the paradigm in section 2.5.

Appendix D: Uncertainty

D.1 Uncertainty of Differential Pressure Measurements across Throttle Valve

Differential pressure gage: Omega PX142-030D5V

To quantify total uncertainty in averaged measured values the following five uncertainties were computed or found and then the root-sum-square (RSS) was used to find the total uncertainty.

- Total manufacturer specified uncertainty
- Calibration uncertainty including error of the standard, regression error of curve fit at 95% confidence, error due to standard deviation of measured calibration points at 95% confidence
- Resolution uncertainty of DAQ board: range (-10) – (10) V, 16 bits
- Uncertainty due to repeatability. This is the standard deviation of the average pressure measurements of the different experimental runs
- Pooled standard deviation of the standard deviations of the average pressure values over all experimental runs as defined in eq.D.1

$$\bar{\sigma} = \sqrt{\frac{1}{N}\sum_{j=1}^{N}\sigma_j^2} \qquad \text{D.1}$$

where N is the number of samples, σ_j is the standard deviation of the jth average measure pressure and $\bar{\sigma}$ is the average standard deviation of the set of values.

Table D.1: Standard deviation and average values of the differential pressure across the throttle valve over the seven experimental runs. Used to calculate the uncertainty due to repeatability and standard deviation of average pressure in table D.2.

Experimental run	Average pressure (kPa)	Standard deviation of average pressure (kPa)
k0	149.95	0.72
k1	151.41	0.51
k2	151.48	0.94
k3_upstream	150.56	0.62
k3_downstream	150.00	0.36
k4_upstream	149.18	0.67
k4_downstream	147.35	0.45

Table D.2: Uncertainty sources and total uncertainty for average differential pressure measurements across the throttle valve.

Error source	Manufacturer (kPa)	Total calibration uncertainty (kPa)	Resolution uncertainty of DAQ board (kPa)	uncertainty due to repeatability (kPa)	Standard deviation of average pressure (kPa)
Value (+/-)	2.04	0.80	7.65E-6	1.43	0.64

The total error for the average differential pressure measurements across the throttle valve using the root-sum-squared method is found to be +/-2.69 kPa, Using the values shown in table D.2.

D.2 Uncertainty of Inlet Pressure Measurements:

Inlet pressure transducer: Kulite Semiconductor .XTL-190-5PSID

The same process as is described in section D.1 is used here to calculate the total uncertainty of the average inlet pressure measurements. It should be noted that a different pressure transducer was initially used but was found to be damaged and giving

suspicious output during experimental runs. The pressure transducer was replaced but only after the data for the non-throttled case had been acquired. For that reason the inlet pressure data from the non-throttled test case is omitted from the repeatability analysis.

Table D.3: Standard deviation and average values of the inlet pressure for the non-throttled test case over the seven experimental runs. Used to calculate the uncertainty due to repeatability and standard deviation of average pressure in table D.4.

experimental run	Average inlet pressure (kPa)	Standard deviation (kPa)
K0	1.56	0.05
K1	1.63	0.05
K2	1.61	0.05
K3_upstream	1.58	0.03
K3_downstream	1.56	0.03
K4_upstream	1.61	0.04
K4_downstream	1.62	0.05

Table D.4: Uncertainty sources and total uncertainty for average inlet pressure measurements.

Uncertainty source	Manufacturer specified uncertainty (kPa)	Total calibration uncertainty (kPa)	Resolution Uncertainty of DAQ board (kPa)	Uncertainty due to repeatability (kPa)	Standard deviation of average pressure (kPa)
Value (+/-)	0.03	0.35	1.00e-4	0.03	0.05

The total uncertainty of the average inlet pressure measurement using the root-sum-squared method is found to be +/-0.36 kPa, using the values shown in table D.4. This value is assumed to be the same for both the throttled and non-throttled case.

D.3 Uncertainty of Inlet Temperature Measurements

Table D.5: Standard deviation and average values of inlet temperature for the throttled and non-throttled test case. Used to calculate the uncertainty due to repeatability and standard deviation of average pressure in tables D.6 and D.7.

experimental run	average temperature measurement (deg C)	standard deviation (deg C)
throttled		
K0	88.05	0.30
K1	88.13	0.14
K2	88.09	0.15
K3_1	88.04	0.12
K3_2	88.14	0.11
K4_1	87.94	0.11
K4_2	87.88	0.21
non-throttled		
K0	88.77	0.23
K1	88.52	0.23
K2	87.88	0.23
K3_1	88.61	0.17
K3_2	88.30	0.16
K4_1	88.43	0.20
K4_2	88.24	0.24

Table D.6: Uncertainty sources and total uncertainty for average inlet temperature measurements for the throttled test case.

Uncertainty source	Manufacturer specified uncertainty (°C)	Total calibration uncertainty (°C)	Resolution Uncertainty of DAQ board (°C)	Uncertainty due to repeatability (°C)	Standard deviation of average pressure (°C)
Value (+/-)	0.14	0.14	7.82e-7	0.10	0.17

The total uncertainty of the average inlet temperature measurement for the case with throttling using the root-sum-squared method is found to be +/-0.28°C, using the values shown in table D.6.

Table D.7: Uncertainty sources and total uncertainty for average inlet temperature measurements for the non-throttled test case.

Uncertainty source	Manufacturer specified uncertainty (°C)	Total calibration uncertainty (°C)	Resolution Uncertainty of DAQ board (°C)	Uncertainty due to repeatability (°C)	Standard deviation of average pressure (°C)
Value (+/-)	0.14	0.14	7.82e-7	0.29	0.21

The total uncertainty of the average inlet temperature measurement for the case without throttling using the root-sum-squared method is found to be +/-0.41°C, using the values shown in table D.7.

D.4 Uncertainty in Inlet Mass Flow Measurements

The uncertainty for the inlet mass flow meter was quantified using the same method listed in section C.1 with the exception of the calibration step since the mass flow meter did not require calibration as mentioned in section C.3.

Table D.8: Standard deviation and average values of inlet mass flow rate temperature for the throttled and non-throttled test case, Used to calculate the uncertainty due to repeatability and standard deviation of average pressure in table D.9 and D.10.

experimental run	average inlet mass flow rate (g/min)	standard deviation (g/min)
throttled		
K0	9.931154	0.429373
K1	10.12179	0.036656
K2	10.03402	0.064222
K3_1	10.09016	0.053147
K3_2	10.08829	0.40854
K4_1	10.1116	0.042086
K4_2	10.01143	0.034602
non-throttled		
experimental run	average inlet mass flow rate (g/min)	standard deviation (g/min)
K0	9.731286	0.500569
K1	10.48869	0.966721
K2	10.35054	0.736175
K3_1	10.18721	0.658868
K3_2	10.37083	0.446787
K4_1	10.64622	0.557879
K4_2	10.36318	0.657656

Table D.9: Uncertainty sources and total uncertainty for average inlet mass flow rate measurements for the throttled test case.

Uncertainty source	Manufacturer specified uncertainty (g/min)	Resolution Uncertainty of DAQ board (g/min)	Uncertainty due to repeatability (g/min)	Standard deviation of average pressure measurements (g/min)
Value (+/-)	0.045	1.19e-9	0.07	0.23

The total uncertainty of the average inlet mass flow rate measurement for the case with throttling using the root-sum-squared method is found to be +/-0.24 g/min, using the values shown in table D.9.

Table D.10: Uncertainty sources and total uncertainty for average inlet mass flow rate measurements for the non-throttled test case.

Uncertainty source	Manufacturer specified uncertainty (g/min)	Resolution Uncertainty of DAQ board (g/min)	Uncertainty due to repeatability (g/min)	Standard deviation of average pressure measurements (g/min)
Value (+/-)	0.045	1.19e-9	0.29	0.67

The total uncertainty of the average inlet mass flow rate measurement for the case without throttling using the root-sum-squared method is found to be +/-0.73 g/min, using the values shown in table D.10.

D.5 Uncertainty in Heat Flux

The manufacturer specified uncertainty for the unit is +/- 0.15 V for the constant current setting.

The Kline and McClintock method was used to quantify the error associated with the measurement of the power supplied to each heater ring based on the measured values of the voltage supplied to each heater ring, V_H, and the current supplied to each heater ring, V_I. The Kline and McClintock method is shown below in eq.D.5[11].

$$u_R = \sqrt{\sum_{i=1}^{n}\left(\frac{\partial R}{\partial x_i}u_{x_i}\right)^2} \qquad \text{D.5}$$

[11] Equation taken from class handout of ME 451 winter term 2007, Dr. Vinod Nrayanan, Instructor

where u_R is the uncertainty in the measured value R and u_{xi} is the ith value of uncertainty in the ith variable x. Average measured values were calculated for V_H and I_H as well as V_V and V_I and were used in the calculations of the uncertainty in the power supplied to each ring, P_H.

Table D.11: Average measured values and uncertainty for V_H, I_H and P_H.

Average values	Inner ring	Middle ring	Outer ring
V_H (V)	15.37	23.79	53.37
u_{VH} (V)	0.89	1.37	3.06
I_H (A)	0.21	0.22	0.24
u_{IH} (A)	0.04	0.04	0.04
P_H (W)	3.23	5.23	12.81
U_{PH} (W)	0.61	0.95	2.15

Next an area average uncertainty for the power sent to the fractal was calculated using the root-sum-square method on the values for the uncertainty in power calculated for the inner, middle and outer heater rings listed in table D.11. The result was a total uncertainty of 2.43 Watts over the entire test device area.

Table D.12: Uncertainty sources and total uncertainty for average input power measurements for the throttled test case.

Source of uncertainty	Voltage divider, manufacturer specified, Resolution of DAQ board (V)	Uncertainty due to repeatability (V)	Standard deviation of average pressure measurements (V)
Value +/-	2.43	0.06	0.09

Using the root-sum-squared method the total uncertainty in the input power for the throttled case is +/-2.43 W, which translates to an uncertainty of heat flux of 0.21 W/cm^2 for the throttled case, as shown in table D.12.

Table D.13: Uncertainty sources and total uncertainty for average input power measurements for the non-throttled test case.

Source of uncertainty	Voltage divider, manufacturer specified, Resolution uncertainty of DAQ board (V)	Uncertainty due to repeatability (V)	Standard deviation of average pressure measurements (V)
Value +/-	2.43	0.10	0.04

Using the root-sum-squared method the total uncertainty in the input power for the non-throttled case is also about +/-2.43 W, which translates to an uncertainty of heat flux of 0.21 W/cm^2 for the non-throttled case, as shown in table D.13.

D.6 Uncertainty in Void Fraction Calculation

A user sensitivity analysis was completed on this algorithm by selecting four different sets of 7 movies each from the 107 movies collected at the K0 location for the case with throttling at the inlet and using each of these different sets to perform the optimization process on the algorithm. This resulted in four different image processing algorithms, 1 for each set of movies. These four image processing algorithms were then used to analyze the complete set of 107 movies they were selected from for void fraction. The result was four different void fraction values; one for each image processing

algorithm. The range of these average void values was used to determine the user sensitivity of the program.

Each of the movies in the 250 movie sets were analyzed one-by-one, frame-by-frame and then the average value of void fraction was calculated for each movie of 1019 frames. Then the averages of each movie were imported into an Excel file and a running average was performed on the averages of each movie. Once the running average of the averages reached a steady value, defined as the point where the fluctuations of the average value were within the boundaries of the uncertainty, the process was stopped and that stable average void fraction value was recorded. The results of the four different image processing algorithms are shown in table D.14.

Table D.14: Average values of void fraction computed using the four different image processing algorithms.

	Case 1	Case 2	Case 3	Case 4
Time averaged α	0.42	0.48	0.45	0.49

The other factor contributing to uncertainty here is the resolution error on the interfaces of the bubbles of the raw images themselves. However, the contribution of the resolution uncertainty to the total uncertainty will ultimately be negligible due to its small magnitude relative to the range of values found in the sensitivity analysis above in table D.14.

Because of the resolution of the image the smooth curvature of the actual vapor-liquid interface will be jagged when displayed in the image. To determine the uncertainty due to the resolution of an image, an image which displayed the typical

phenomena at the K0 level was chosen to analyze. The K0 region was chosen because it is believed that due to the relatively large width of the channel compared to other branching levels the uncertainty due to resolution will be greatest at this location. An image at this location which displayed a clearly defined vapor-liquid interface was chosen. A two pixel wide strip than spanned the interface from channel wall to channel wall was compared to the total defined area of the channel where the image was taken. Due to the large radius of curvature of the interface the length of the interface was approximated as merely the channel width. Thus the uncertainty due to resolution was gauged by the ratio of a two pixel wide strip across the width of the channel to the total defined area of the channel. Using this definition the uncertainty of void fraction due to uncertainty of resolution is estimated to be +/-0.006.

Thus, using the root-sum-squared method the total estimated uncertainty in measured void fraction is +/- 3.5.

Appendix E: Data and Uncertainty Used for Bubble Growth and Decay

E.1 Bubble Length Data

Table E.1: Apparent bubble collapse data in K4 upstream with throttling shown in fig.3.19. Data is taken from movie: HS_10_20_88_F16_H5_6_k4aaa1_150_093.

Frame #	Apparent length (μm)
689	2650
690	2450
691	2150
692	1800
693	1400
694	950
695	550
696	350
697	250
698	200
699	150

Table E.2: Apparent bubble collapse data in K4 upstream with throttling shown in fig.3.20. Data is taken from movie: HS_10_20_88_F16_H5_6_k4aaa1_150_002.

Frame #	Apparent length (μm)
473	2200
474	2100
475	2000
476	1900
477	1750
478	1550
479	1350
480	1200
481	950
482	750
483	500
484	350
485	250
486	200
487	175
488	150
489	150
490	150
491	150

Table E.3: Apparent bubble collapse data in K1 with throttling shown in fig.3.25. Data is taken from movie: HS_10_20_88_F16_H5_6_k1_150_000.

Frame #	Apparent length (μm)
197	1981
198	1274
199	708
200	495
201	425

Table E.4: Apparent bubble collapse data in K1 without throttling shown in fig.3.26. Data is taken from movie: HS_10_20_88_F16_H5_6_k1_005.

Frame #	Apparent length (μm)
421	1557
422	1274
423	708
424	495
425	354
426	283

Table E.5: Bubble growth data in K4 upstream with throttling shown in fig.3.28. Data is taken from movie: HS_10_20_88_F16_H5_6_k4aaa1_150_070.

Frame #	Apparent length (μm)
693	80
695	300
696	1400
697	2300
698	3600

Table E.6: Bubble growth data in K4 upstream with throttling shown in figures 3.29 and 3.31. Data is taken from movie: HS_10_20_88_F16_H5_6_k4aaa1_150_067.

Frame #	Apparent length (μm)
402	150
404	300
406	800
408	1650
410	2500
412	2650
414	1800
416	650
418	150

E.2 Method of Measurement of Interfaces and Uncertainty

The locations of the interfaces were measured from the apparent outermost points of the up and downstream interfaces, which resided on the outside of the fuzzy region between the vapor and liquid in the channel, as shown in fig.E.1.

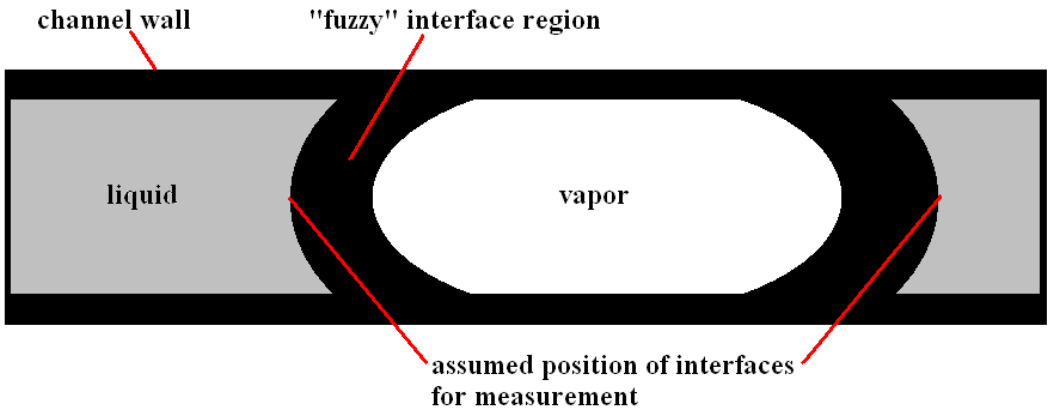

Figure E.1: Measurement locations of vapor-liquid interfaces.

The distance between locations of the apparent outermost points of the interfaces were measured by manually counting the pixels spanning between the interfaces and then dividing that value by the measured resolution[12] of the 5x objective, thus yielding a length in microns.

To gauge the uncertainty of this measurement a range of possible pixels which could possibly represent the location of the outermost points of the interfaces values on either side of the apparent location of the outermost points of the interfaces. After examining multiple frames this value was found to be roughly +/- 8 pixels which translates to +/- 40 microns.

Appendix F: Pressure Drop across Interface at K4 Branching Level

From White [F1] eq. 1.32 describes the pressure difference across an interface of a given curvature due to surface tension shown below in eq.F.1.

$$\Delta P = \frac{2\gamma}{R} \qquad \text{F.1}$$

where γ is the surface tension of water and R is the radius of curvature of the interface. The above expression assumes the first principal radius of curvature is taken to be R and the second radius of curvature is taken to be infinite. R could also be written as shown in eq.F.2

$$R = \frac{a}{\cos\theta} \qquad \text{F.2}$$

where a is the half width of the channel and θ is the angle made between the interface and the channel wall at the point of contact. Substituting eq.F.2 into eq.F.1 yields eq.F.3

$$\Delta P = \frac{2\gamma}{a}\cos\theta \qquad \text{F.3}$$

In the case of the k4 branching level a=0.00005m. Assuming saturation conditions at atmosphere at the k4 level the surface tension is reported in White [F1] as 0.0589N/m. Below a range of pressure drops across an interface of varying degrees of curvature is shown in table F.1.

Table F.1: Pressure drop induce by curvature of vapor-liquid interface due to surface tension.

Θ (degrees)	ΔP (Pa)	Θ (degrees)	ΔP (Pa)
0	2356	60	1178
15	2276	75	610
30	2040	90	0
45	1666		

[12] Measurement made by Douglas Heymann, Graduate Student, Oregon State University

Appendix G: Effect of Pressure Fluctuations on Bubble Size

G.1 Possible Void Loss Due to Increase in Local Pressure Field

Homogenous void fraction correlation, shown in eq.G1, is used to determine quality.

$$\alpha = x\left[x + (1-x)\frac{\rho_g}{\rho_l} \right]^{-1} \qquad \text{G.1}$$

Solving eq.G1 for the quality x, yields eq.G2

$$x = \frac{\alpha\rho_g}{\alpha(\rho_g - \rho_l) + \rho_l} \qquad \text{G.2}$$

Density of saturated liquid and vapor at atmospheric pressure

$$\rho_l = 958.3\frac{kg}{m^3}, \rho_g = 0.5977\frac{kg}{m^3}$$

At approximately halfway down the k4 branching level (z=14.8mm) the model predictions for 10 g/min, 1.76W/cm^2 are

$$\alpha=0.67, P=101{,}410 \text{ Pa}$$

Using this value of alpha and densities of the saturated fluid and vapor the quality is found using eq.G2 to be

$$x_1=0.0013$$

In the process of the pressure fluctuation it is assumed the temperature of the vapor liquid mixture remains constant but the local saturation pressure will of course vary with the pressure change. Thus the assumption will be made that the enthalpy of the vapor liquid mixture remains the same between pressure fluctuations.

Using the relation between quality and enthalpy and the above assumptions it will be possible to calculate the change in void fraction which could be induced by the pressure fluctuations.

The relation between quality and enthalpy is stated as eq.G3

$$x = \frac{h - h_f}{h_g - h_f} \qquad \text{G.3}$$

Where f and g denote saturated fluid and vapor, respectively. To find the saturated fluid and vapor enthalpies first the saturation temperature at each pressure is needed. To find the saturation temperature at each state a pressure fluctuation of 1500 Pa is assumed, which is characteristic of the typical fluctuations measured, with an initial pressure value found from the model results for 10g/min, 20 watts at z=14.8mm of 101,410Pa. Below in table G1 the fluid properties before and after the pressure oscillation are tabulated.

Table G.1: Fluid/vapor mixture properties before at max and min values of pressure fluctuation.

State 1: conditions before pressure increase	State 2: conditions after pressure increase
p_1=101,410Pa	P_2=102,910Pa
$T_{1,sat}$=107.56 °C	$T_{2,sat}$=107.68 °C
h_{1f}=450.92 kJ/kg	h_{1f}=451.42 kJ/kg
h_{1g}=2,687.7 kJ/kg	h_{1g}=2,687.9 kJ/kg

Using the definition found in eq.G3 and the assumption of a constant enthalpy process the quality at state two is found to be as shown in eq.G4.

$$x_2 = \frac{h_{1f} - h_{2f} + x_1\left(h_{1g} - h_{1f}\right)}{\left(h_{2g} - h_{2f}\right)} \qquad \text{G.4}$$

Then employing the values found in table G1 x_2 becomes

$$x_2 = 0.0011$$

Using eq.G1 to calculate a void fraction from this it is found

$$\alpha_2=0.6384$$

So it is found that the increase of pressure by 1,500Pa could produce a roughly 5% decrease in void fraction due solely to increase in the saturation temperature if indeed the temperature of the two-phase mixture remains unchanged.

G.2 Effect of Pressure Fluctuations on Compression of a Vapor Slug

Using the saturation temperatures found above for the assumed pressure fluctuations values from the specific volume at each state can be interpolated. Below in table G2 the fluid properties before and after the pressure oscillation are tabulated.

Table G.2: Conditions at max and min values of pressure fluctuations

State 1: conditions before pressure increase	State 2: conditions after pressure increase
p_1=101,410Pa	P_2=102,910Pa
$T_{1,sat}$=107.56 °C	$T_{2,sat}$=107.68 °C
υ_{1g}=1330.2 cm^3/g	υ_{1g}=1324.8 cm^3/g

In this case it is found for a given mass of vapor the 1,500Pa increase in pressure can be expected to compress the vapor slug by 0.41% of its initial volume. If the vapor slug is assumed to fill the entire cross-section of the channel and its length is the only variable dimension then a slug of initial length of 1mm with compress down to a slug of length 0.9986 mm.

With both of these considerations together they are not sufficient to account for the tremendous decrease in apparent volume of vapor as is observed in the apparent bubble collapses in the k4 level.

Appendix H: Vapor Condensation Calculations

H.1 Energy Lost From a Condensing Bubble

- Estimate how much energy would need to be removed from a bubble collapsing.
- Assume a vapor slug in K4 branching level channel which is initially 1 mm in length and fills the entire cross-section of the channel.
- Assume vapor slug loses half its volume in 1 ms (this is actually a bit of an over estimate as most of the apparent bubble collapses did not happen this fast).

The energy lost in the collapse process, Q_1, is equal to the mass flow rate of the vapor multiplied by the change in enthalpy of the vapor which condenses to water and is shown below in eq.H.1.

$$Q_1 = \dot{m}_v (\Delta h) \tag{H.1}$$

the mass flow rate is defined as the density of the vapor multiplied by the change in volume of the vapor over the specified time period as shown below in eq.H.2.

$$\dot{m}_v = \rho_v \frac{\Delta V_v}{\Delta t} \tag{H.2}$$

the change in enthalpy is the case of a bubble condensing is the heat of fusion, h_{fg}. Using this definition for the enthalpy and substituting eq.H2. into eq.H.1, eq.H.3 is obtained.

$$Q_1 = \rho_v \frac{\Delta V_v}{\Delta t} h_{fg} \tag{H.3}$$

the four parameters in eq.H.3 are defined as follows

$$\rho_v(saturated\_H_20\_vapor@100^\circ C) = 0.6\frac{kg}{m^3}$$
$$\Delta V_v = 0.0005m \cdot (0.00025m \cdot 0.0001m) = 1.25E-11m^3$$

$$h_{fg}(saturated\_H_20\_vapor@100^{\circ}C) = 2257E3\frac{J}{kg}$$

$$\Delta t = 0.001s$$

$$Q_1 = 0.6\frac{kg}{m^3}\cdot\frac{1.25E-11m^3}{0.001s}\cdot 2257E3\frac{J}{kg} \approx 0.02W$$

H.2 Possible Energy Transfer Rate from a Vapor Slug at the K4 Branching Level to the Channel Wall

- Assume the same initial size of vapor slug as in part 1: 1mm long vapor slug which fills the entire cross-section of the channel.
- Total heat transfer area includes two side walls, top wall and bottom wall of channel.
- Assume wall temperature of 95°C.

Heat transfer area, A_{Q2}, is found to be

$$A_{Q_2} = 2\cdot(0.00025\cdot 0.001)m^2 + 2\cdot(0.0001\cdot 0.001)m^2 = 7E-7m^2$$

the coefficient of heat transfer is found using eq.10.42 from Incorpera & Dewitt [H1] for condensing flow in a tube and is shown below in eq.H.4

$$h = 0.555\left[\frac{g\rho_l(\rho_l-\rho_v)k_l^3 h_{fg}^{'}}{\mu_l(T_{sat}-T_s)D}\right]^{1/4} \qquad \text{H.4}$$

where

$$h_{fg}^{'} = h_{fg} + \frac{3}{8}\cdot(c_{p,l})\cdot(T_{sat}-T_s) \qquad \text{H.5}$$

where g is the acceleration due to gravity, ρ_l & ρ_v are the respective densities of the liquid and vapor phases, k_l is the thermal conductivity of the liquid phase, h_{fg} is the heat of fusion, μ_l is the viscosity of the liquid phase, T_{sat} & T_s are the saturation temperature and the surface (wall) temperature of the channel, respectively, and D is the hydraulic diameter of the channel. All of the parameters found in eq.H.4 & eq.H.5 were evaluated for water at 100°C. Thus, with a wall temp of 95°C, h is found to be

$$h_{fg,95}^{'} = 2257\frac{kJ}{kg} + \frac{3}{8}\cdot\left(4.217\frac{kJ}{kg\cdot K}\right)\cdot(313-308)K = 2265\frac{kJ}{kg}$$

$$h_{95} = 0.555\left[\frac{9.81\frac{m}{s^2}\cdot 1000\frac{kg}{m^3}\cdot\left(1000\frac{kg}{m^3}-0.6\frac{kg}{m^3}\right)\cdot\left(0.68\frac{W}{mK}\right)^3\cdot 2265E3\frac{J}{kg}}{0.279E-3\frac{N\cdot s}{m^2}\cdot\left(313K-308K\right)\cdot 1.43E-4m}\right]^{1/4} \approx 43{,}000\frac{W}{m^2\cdot K}$$

Thus the heat transfer rate, Q_2, from the vapor core to the channel wall during condensation is estimated to be

$$Q_{2,95} = h\cdot A_{Q_2}\cdot\Delta T = 43{,}000\frac{W}{m^2\cdot K}\cdot 7E-7m^2\cdot 5K \approx 0.15W$$

if the wall temperature is increased to 97°C, 99°C and 99.9°C the heat transfer rates are found to be

$$Q_{2,97} \approx 0.10W$$

$$Q_{2,99} \approx 0.04W$$

$$Q_{2,99.9} \approx 0.008W$$

So it seems that if the channel wall temperature is somewhere around 99°C and the two-phase mixture of the channel is at 100°C the vapor may actually condense. This is based on the values of Q_1 & Q_2 being the same order of magnitude.

Appendix I: Area Averaged Void Fraction Calculations

I.1 Measured Values

Table I.1: Area weighted average void calculation of measured void values.

length of channel area (pixels)	width of channel area (pixels)	length of channel (m)	width of channels (m)	planform area of individual channel (m^2)	# of channels per branching level	total planform area of channels of branching level (m^2)	average void *average area/total area
320	85	1.62E-03	4.29E-04	6.94E-07	1	6.94E-07	7.52E-03
318	62	1.61E-03	3.13E-04	5.03E-07	2	1.01E-06	1.39E-02
509	41	2.57E-03	2.07E-04	5.32E-07	4	2.13E-06	4.82E-02
378	30	1.91E-03	1.52E-04	2.89E-07	8	2.31E-06	7.02E-02
425	30	2.15E-03	1.52E-04	3.25E-07	8	2.60E-06	7.14E-02
663	22	3.35E-03	1.11E-04	3.72E-07	16	5.95E-06	4.29E-02
704	22	3.56E-03	1.11E-04	3.95E-07	16	6.32E-06	5.19E-02
						Sum of channel areas= 2.10E-05	Average void= 0.31
length of channel area (pixels)	width of channel area (pixels)	length of channel (m)	width of channels (m)	planform area of individual channel (m^2)	# of channels per branching level	total planform area of channels of branching level (m^2)	average void *average area/total area
320	85	1.62E-03	4.29E-04	6.94E-07	1	6.94E-07	1.40E-02
318	62	1.61E-03	3.13E-04	5.03E-07	2	1.01E-06	1.64E-02
509	41	2.57E-03	2.07E-04	5.32E-07	4	2.13E-06	5.17E-02
378	30	1.91E-03	1.52E-04	2.89E-07	8	2.31E-06	5.83E-02
425	30	2.15E-03	1.52E-04	3.25E-07	8	2.60E-06	7.28E-02
663	22	3.35E-03	1.11E-04	3.72E-07	16	5.95E-06	1.35E-01
704	22	3.56E-03	1.11E-04	3.95E-07	16	6.32E-06	2.06E-02
						Sum of channel area= 2.10E-05	Average void= 0.37

I.2 Values Predicted by Model

Table I.2: Area weighted average void calculation of predicted void values from model[13].

	channel length (m)	channel width (m)	planform area of channel (m^2)	# of channels	total planform area of branching level (m^2)
k0	1.58E-03	4.00E-04	6.32E-07	1	6.32E-07
k1	1.73E-03	2.83E-04	4.90E-07	2	9.79E-07
k2	2.62E-03	2.00E-04	5.24E-07	4	2.10E-06
k3	4.03E-03	1.41E-04	5.68E-07	8	4.55E-06
k4	5.96E-03	1.00E-04	5.96E-07	16	9.54E-06
	average void for 10 g/min 1.58 W/cm^2	average void for 10g/min 1.76 W/cm^2	average void for 10 g/min 1.94 W/cm^2		
k0	0.00	0.00	0.00		
k1	0.00	0.00	0.00		
k2	0.00	0.00	0.00		
k3	0.00	0.00	0.01		
k4	0.53	0.60	0.67		
average void *average area/total area					
k0	0.00	0.00	0.00		
k1	0.00	0.00	0.00		
k2	0.00	0.00	0.00		
k3	0.00	0.00	0.00		
k4	0.28	0.32	0.36		
area weighted average void fraction values	0.28	0.32	0.36		

[13] Daniels et al. [4]